3-11-2011

Characterization of a Boron Carbide Heterojunction Neutron Detector

James E. Bevins

CHARACTERIZATION OF A BORON CARBIDE HETEROJUNCTION NEUTRON DETECTOR

THESIS

James E. Bevins, Second Lieutenant

AFIT/GNE/ENP/11-M02

DEPARTMENT OF THE AIR FORCE
AIR UNIVERSITY

AIR FORCE INSTITUTE OF TECHNOLOGY

Wright-Patterson Air Force Base, Ohio

AFIT/GNE/ENP/11-M02

The views expressed in this thesis are those of the author and do not reflect the official policy or position of the United States Air Force, the Department of Defense, or the United States Government. This material is declared a work of the U.S. Government and is not subject to copyright protection in the United States.

AFIT/GNE/ENP/11-M02

CHARACTERIZATION OF A BORON CARBIDE HETEROJUNCTION NEUTRON DETECTOR

THESIS

Presented to the Faculty

Department of Engineering Physics

Graduate School of Engineering and Management

Air Force Institute of Technology

Air University

Air Education and Training Command

In Partial Fulfillment of the Requirements for the

Degree of Master of Science in Nuclear Engineering

James E. Bevins, BS

Second Lieutenant, USAF

March 2011

APPROVED FOR PUBLIC RELEASE; DISTRIBUTION UNLIMITED

AFIT/GNE/ENP/11-M02

CHARACTERIZATION OF A BORON CARBIDE HETEROJUNCTION NEUTRON DETECTOR

James E. Bevins, BS

Second Lieutenant, USAF

Approved:

LTC John W. McClory (Chairman)	Date
James C. Petrosky, PhD (Member)	Date
Maj Benjamin R. Kowash (Member)	Date

Abstract

New methods for neutron detection have become an important area of intense research in support of national security objectives. In support of this effort p-type B_5C on n-type Si heterojunction diodes have been built and tested. These diodes have demonstrated potential for high efficiency neutron detection and possible integration into a first-of-its-kind real-time solid-state neutron spectrometer. To realize these goals, the diodes must be optimized to increase neutron detection efficiency.

This research sought to optimize the boron carbide (BC) diode by coupling the nuclear physics modeling capability of GEANT4 and TRIM with the semiconductor device simulation tools from Synopsis' TCAD semiconductor modeling software. GEANT4 and TRIM were used to model the physics of the neutron capture event on boron and subsequent transport of the secondary ^{4}He and ^{7}Li particles throughout the device. This information was used to construct heavy ion models in TCAD where the transient electrical response in the BC on Si diode was modeled. Through an iterative modeling process of controllable parameters, optimal device construction was determined such that intrinsic detection efficiency and total charge collection were optimized. Due to a lack of benchmark data regarding charge collection, normalized functional forms governing the efficiency and charge collection at each contact for each parameter

were developed. This method will allow for an estimation of expected charge collection and efficiency given a set of operating parameters that include: silicon resistivity, BC resistivity, BC thickness, silicon thickness, applied bias, and collection contact. In general, charge collection was maximized with high bias operation of thin BC layers on thin silicon substrates (the thinner the better for both BC and Si) of low resistivity ($\leq$ 10 Ω-cm), while the capture efficiency was maximized for thicker BC layers.

Additionally, the effects of neutron damage on BC diodes were studied to determine damage thresholds and resulting device performance and lifetime. Sample irregularities limited the irradiation results to two BC diodes with silicon substrate resistivities of 8k and 20k Ω-cm. The major limitation found for device performance was the increase in the leakage current (~340% at a thermal fluence of 9.7×10^{13} n cm^{-2}) in the 8k Ω-cm diode. However, the 20k Ω-cm diode exhibited no statistically significant change in leakage current indicating that the BC and interface defect density can be used to engineer a more radiation-hardened device. Type inversion was not measured at the total fluence levels achieved, but the 8k Ω-cm diode effective carrier concentrations (N_{eff}) decreased by 30% at a total thermal fluence of 7.5×10^{13} n cm^{-2} (1×10^{13} 1 MeV neutron equivalent). For the same irradiation conditions, the 20k Ω-cm diode N_{eff} decreased by 57%. These results indicate that the hardness of the diodes can also be improved with low resistivity silicon substrates.

To My Wife and the Three Hellions

Acknowledgements

Many people and organizations made this work possible. First and foremost, this research was funded in part through the Defense Threat Reduction Agency, the Department of Homeland Security, and the Office of Naval research. Without their material support, none of this would have been possible.

The support and guidance provided by my advisor, LTC John McClory, and committee members, Dr. Petrosky and Maj Kowash, was invaluable throughout the process. Without their support in their respective areas of expertise, I would still be mired in this research effort. In particular, LTC McClory was always available to provide assistance in every phase of this research effort, Dr. Petrosky was most helpful with the TCAD software package and radiation effects, and Maj Kowash's expertise in signal processing helped enable the development of useful quantifications of the optimization results. Their support and encouragement has also given me the opportunity to present this research through conferences and journals.

The support staff at the various facilities utilized was outstanding. Dr. Abigail Bickley's expertise in GEANT was the only reason I was able to obtain any useful results from GEANT. Mr. Eric Taylor, NENG's laboratory technician, was instrumental in accumulating and developing the equipment

needed for the irradiation studies. The OSURR support staff was extremely helpful. They bent over backwards to help me get reactor time and flux measurements on a very short notice. Mr. Dave Doak, the high power computing administrator, was instrumental in overcoming issues with the cluster, LINUX lab, and TCAD licensing.

Numerous AFIT students provided help, advice, and served as sounding boards during this research. At the risk of missing someone, I would like to thank (in no particular order) 2Lt Chris Dahl, Capt Jesse Foster, MAJ Ben Thomas, Mr. Matt Halstead, Tony Kelly, and 1Lt Brad Jones.

Last, but not certainly not least, I would like to thank my loving wife and three beautiful daughters. Their support and encouragement has been truly amazing. Despite going to school herself, I do not think there has been a single paper or presentation on which my wife has not taken the time to provide her advice and English assistance on. Somewhat more begrudgingly, I would also like to thank my parents for their advice and words of encouragement throughout this process. In fact, they also attempted to help overcome my English deficiency in writing this document despite not understanding a word I wrote.

James E. Bevins

Table of Contents

Page

Page

List of Figures

Figure **Page**

Figure **Page**

Figure **Page**

Figure **Page**

Figure **Page**

Figure **Page**

List of Tables

List of Acronyms

AFIT	Air Force Institute of Technology
AMN	AFIT, UMKC, and UNL
BC	Boron Carbide
B_5C	Shorthand for the $C_2B_{10}H_{12}$ carboranes
C-V	Capacitance vs. voltage
DHS	Department of Homeland Security
DTRA	Defense Threat Reduction Agency
e-h	Electron-Hole pairs
eV	Electron-volt
GEANT	Geometry and Tracking: nuclear physics modeling software
HEU	Highly enriched uranium: uranium containing $>$ 20% ^{235}U
I-V	Current vs. voltage
LET	Linear energy transfer [energy distance^{-1}]
MDL	Minimum detectable level
MeV	Mega electron-volt (10^6 eV)
NIEL	Non-ionizing energy loss
NDSU	North Dakota State University
PECVD	Plasma enhanced chemical vapor deposition
SEM	Scanning Electron Microscope

SEU	**Single event upset**
S/N	**Signal-to-noise**
SNM	**Special Nuclear Material: Defined by the Atomic Energy Act of 1954 as ^{233}U, ^{235}U, and ^{239}Pu [1].**
TCAD	**Technology Computer-Aided Design: semiconductor modeling software**
TRIM	**Transport of Ions in Matter: heavy ion transport model**
UMKC	**University of Missouri – Kansas City**
UNL	**University of Nebraska – Lincoln**
WGPu	**Weapons grade plutonium: $< 7\%$ ^{240}Pu**

List of Symbols

A	Amperes
C	Capacitance [F]
d	Distance for charge collection of material thickness [μm]
Є	Electric field [V cm^{-1}]
E_{dep}	Energy deposited [eV]
E_F	Fermi energy [eV]
E_g	Band gap energy [eV]
E_{pr}	Energy required to create an e-h pr [eV]
ε	Dielectric constant
K	Damage constant specific to material and radiation [cm^2 $particle^{-1}$]
kT	Thermal energy
N_A	Acceptor type doping concentration [cm^{-3}]
N_c	Effective conduction band density of states [cm^{-3}]
N_D	Donor type doping concentration [cm^{-3}]
N_{eff}	Effective doping concentration [cm^{-3}]
N_v	Effective valence band density of states [cm^{-3}]
μ	Carrier mobility [cm^2 V^{-1} s^{-1}]
q	Fundamental charge [C]
Q	Charge collected [C]

R	Rate of ion deposition in silicon per incident neutron
τ	Lifetime [sec]
t_{trans}	time to collect the generated charge carriers
t_{plasma}	time to disperse the e-h pr cloud such that they do not self shield
V_{bi}	Built-in voltage [V]
V_{app}	Applied bias [V]
χ	Electron affinity [eV]
ϕ	Fluence [particles cm^{-2}]
ϕ_{inv}	Fluence to achieve inversion [n cm^{-2}]

CHARACTERIZATION OF A BORON CARBIDE HETEROJUNCTION NEUTRON DETECTOR

I. Introduction

1.1 Background

Due to recent worldwide events and the fall of the Soviet Union, the ability to track and intercept special nuclear material (SNM [1]) has become a top priority for U.S. National Security [2]. Screening of inbound shipments at points of entry such as ports and border crossings requires an ability to detect SNM at distances of several meters or more. However, SNM presents a unique challenge for standoff detection due to short range of characteristic gamma/x-rays and/or low intrinsic activity. Many fissile isotopes emit very few spontaneous fission neutrons (^{233}U, ^{235}U, and ^{239}Pu) with ^{240}Pu being the only isotope present in any abundance in SNM to have a significant spontaneous fission neutron emission rate (~920 n g^{-1} s^{-1}) [3]. Furthermore, gamma ray energies typical of these fissile isotopes lie in the region below 200 keV for decays with any appreciable intensity, thereby limiting their range and making it

very easy to shield highly enriched uranium (HEU) and weapons grade plutonium (WGPu) from detectors designed to identify these signatures [4] .

Cosmic-ray induced spallation neutrons further complicate matters since they have the highest emission rate when generated at high Z/air interfaces, which are ubiquitous on ships and cargo containers [5]. The increase in the neutron background as a function of Z is depicted in Figure 1 [6]. Although numerous values abound, the typical background for air/sea interfaces is ~120 n m^{-2} s^{-1} [7], while the background from "ship-effect neutrons" at air/iron interfaces is ~770 n m^{-2} s^{-1} with significant short duration spikes as shown in Figure 2 [7,8]. This presents a significant challenge in detecting a hypothetical weapons mass of 4 kg of 94% ^{239}Pu WGPu which would have an isotropic neutron flux on the order of 3900 n m^{-2} s^{-1} at a distance of 3m assuming no shielding or moderation [7].

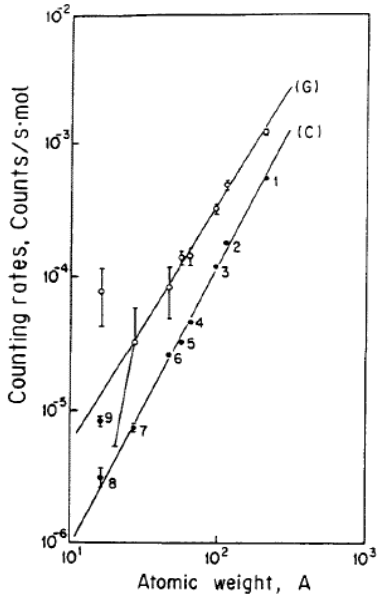

Figure 1. Atomic weight dependence of coincident (C) and gross (G) counting rates. 1:Pb, 2:Cd, 3:Nb-Mo, 4:Cu-Zn, 5:Fe, 6:Ti-Al-V-Sn, 7:Al, 8:H_2O, 9:D_2O [6].

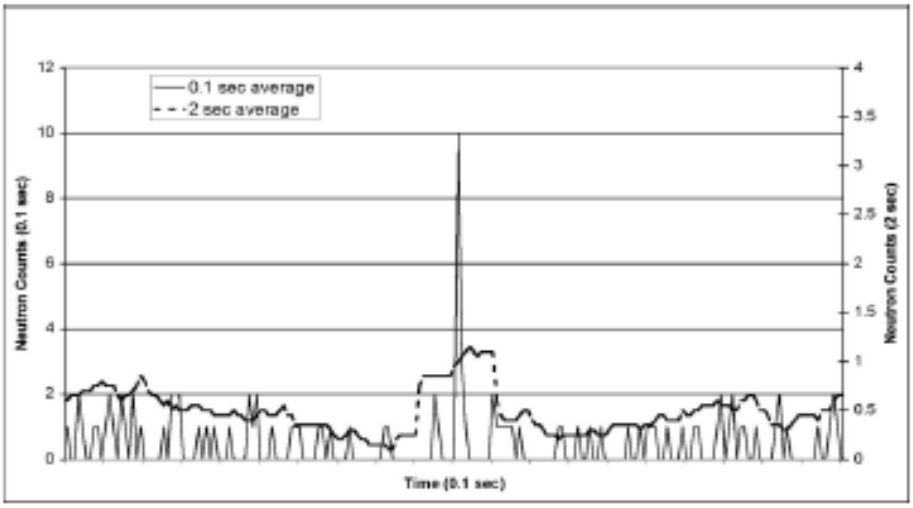

Figure 2. Neutron spike induced by cosmic ray interaction [7].

Since detection of SNM based solely on increased neutron counting rates is subject to the limitations presented above, additional means of distinguishing

SNM are required to reduce the false positive and false negative rates inherent in a neutron-counting rate based detector. Obvious options include spectroscopy and incorporation with a high efficiency gamma spectrometer. As noted previously, the short range of the characteristic gammas for SNM limits the usefulness of gamma spectrometers for standoff detection. While neutron spectroscopy with 100 keV or better resolution would be able to distinguish the characteristic fission spectra of SNM from the cosmic induced neutron background as shown in Figure 3, no current real-time neutron spectrometers exist [8,9,10].

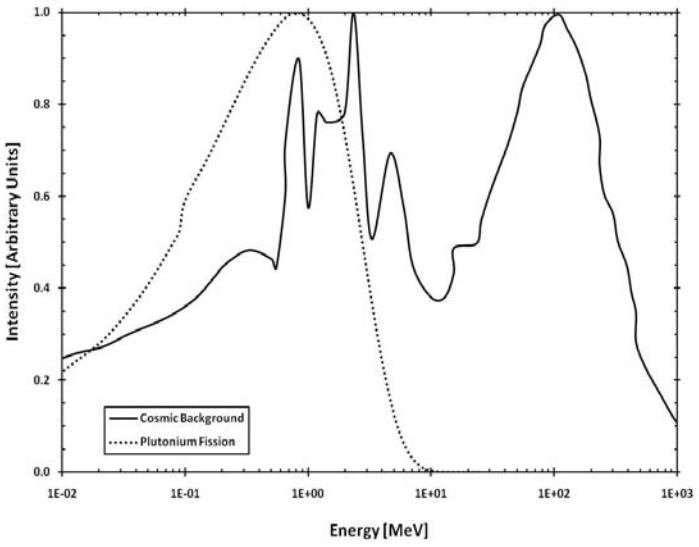

Figure 3. Comparison of cosmic background and plutonium fission neutron spectra [8,9].

The shortage of ^{3}He brought about by the convergence of limited production since the 1988 closure of the Savannah River production facility and

the post-9/11 boom in security related neutron detector usage – shown in Figure 4 – has been restricting the effort to field large numbers of ^{3}He neutron detectors [11]. These factors have resulted in an almost 80% reduction in US stock of ^{3}He since 2000 as is shown in Figure 5 [11]. Consequently, the Defense Threat Reduction Agency (DTRA) and the Department of Homeland Security (DHS) have made finding ^{3}He alternatives a top priority [5,11]. In support of this effort, the Air Force Institute of Technology (AFIT) is currently collaborating with the University of Missouri-Kansas City (UMKC) and the University of Nebraska-Lincoln (UNL) to develop solid-state neutron detectors based on semi-conducting boron carbide (BC) direct conversion diodes.

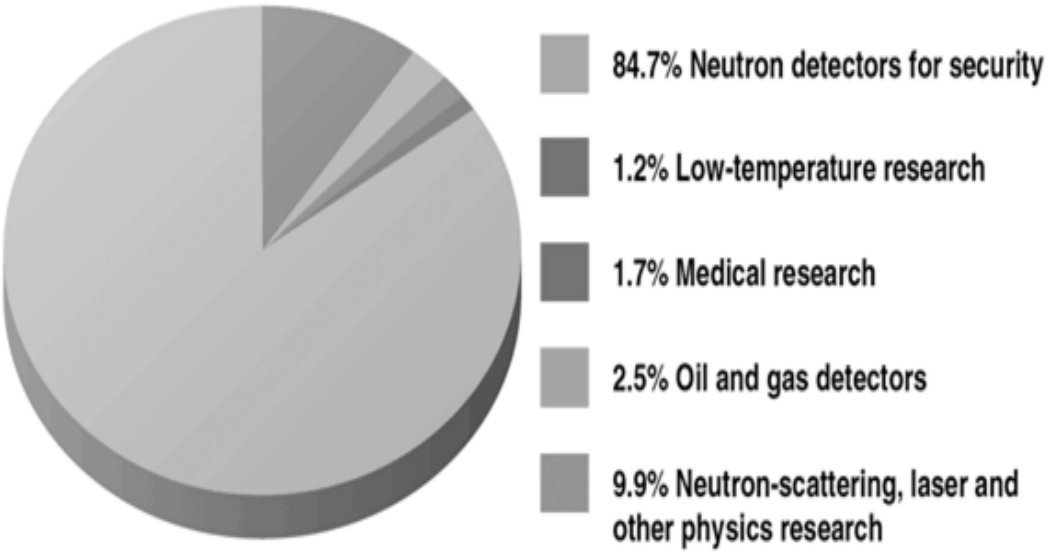

Figure 4. ^{3}He usage as of 2008 [11].

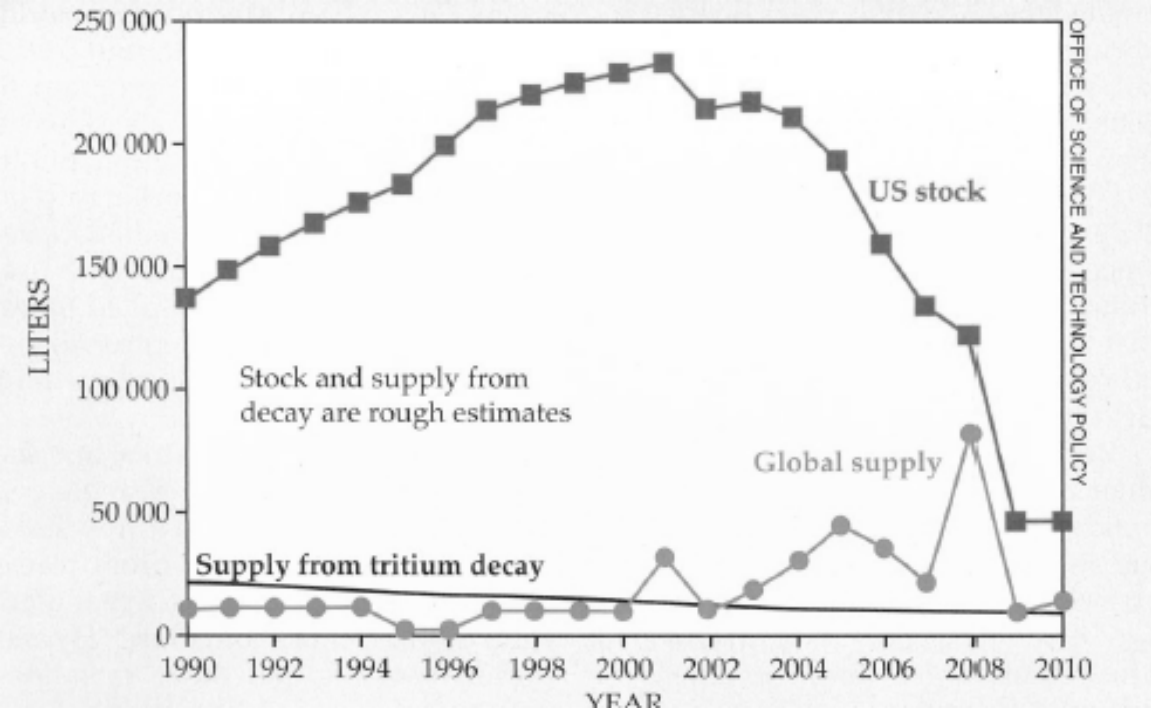

Figure 5. Supply of ^{3}He over past 20 years [11].

Semiconducting BC diodes are, in many ways, nearly ideal neutron detectors having advantages in cross-section, density, charge collection, and gamma discrimination. The primary consideration for a detection medium is its interaction rate with the incident radiation. This is driven by the cross-section and density. As shown in Figure 6, ^{10}B has a capture cross-section second only to ^{157}Gd [5]. Additionally, the density of BC (~2.5 g cm^{-3}) is much higher than that of scintillators (~1 g cm^{-3}) or BF_3 and ^{3}He gas detectors ($<$ 0.1 g cm^{-3}) in common use today [12]. The combination of these two factors results in higher neutron interaction densities and lower neutron mean free path lengths as shown in Figure 7, where BC is second only to Gd_2O_3 in the thermalized region of the

energy spectrum, outperforms all in the epithermal region (< 0.1 MeV), and is second to UO_2 in the fast region.

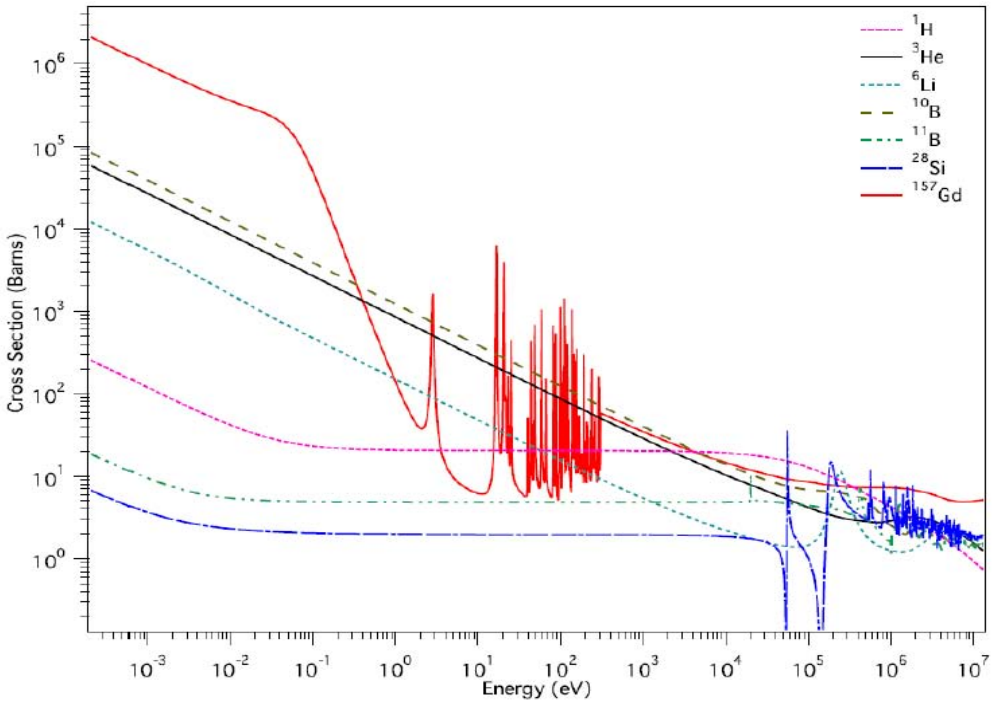

Figure 6. Neutron capture cross-sections of various materials [5].

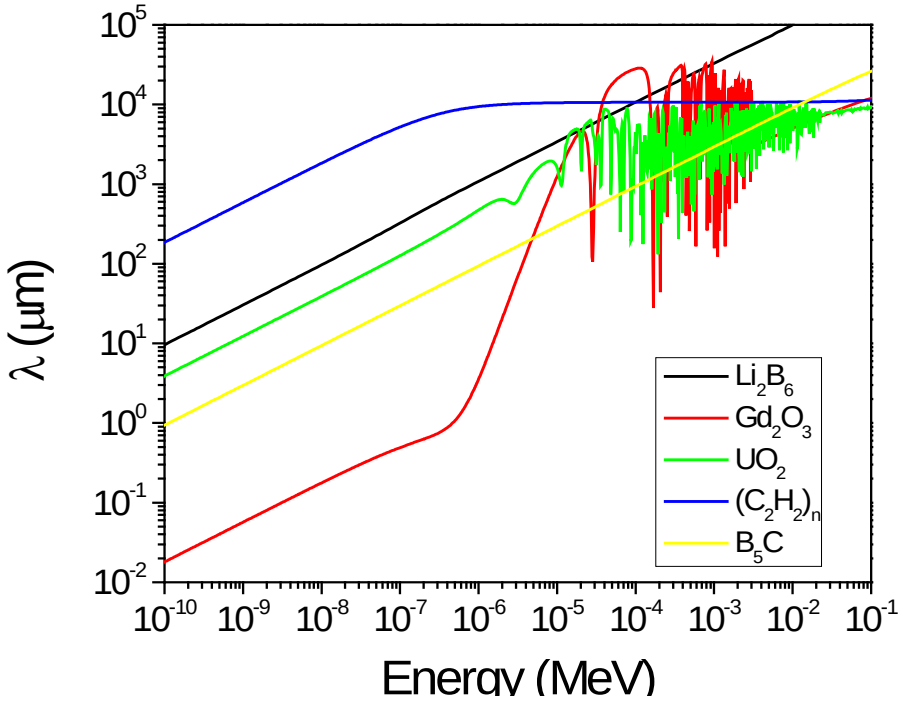

Figure 7. Neutron mean free path in several possible next generation neutron detector materials [10].

High theoretical efficiencies are useless if the resulting radiation byproducts, in this case electron-hole pairs (e-h), cannot be collected efficiently. Again, the ^{10}B reaction is highly beneficial due to the heavy ions generated as capture products 100% of the time, as shown in (1) and (2) [13]:

$$^{10}\mathrm{B} + \mathrm{n} \rightarrow {}^{7}\mathrm{Li}\ (0.84\mathrm{MeV}) + {}^{4}\mathrm{He}\ (1.47\mathrm{MeV}) + \gamma\ (0.48\mathrm{MeV})\ \ [94\%] \quad (1)$$

and

$$^{10}\mathrm{B} + \mathrm{n} \rightarrow {}^{7}\mathrm{Li}\ (1.02\mathrm{MeV}) + {}^{4}\mathrm{He}\ (1.78\mathrm{MeV})\ \ \ [6\%]\ . \quad (2)$$

These heavy ions will fully deposit their charge in only a few microns thereby requiring small depletion widths in the diode and allowing for low bias

operations. The low bias operation is highly beneficial when considering long-term, adaptable field use of these detectors. Low bias operation also allows for the possible realization of a neutron spectrometer based on the incorporation of hundreds or thousands of diodes within a moderating volume as depicted in Figure 8 [10].

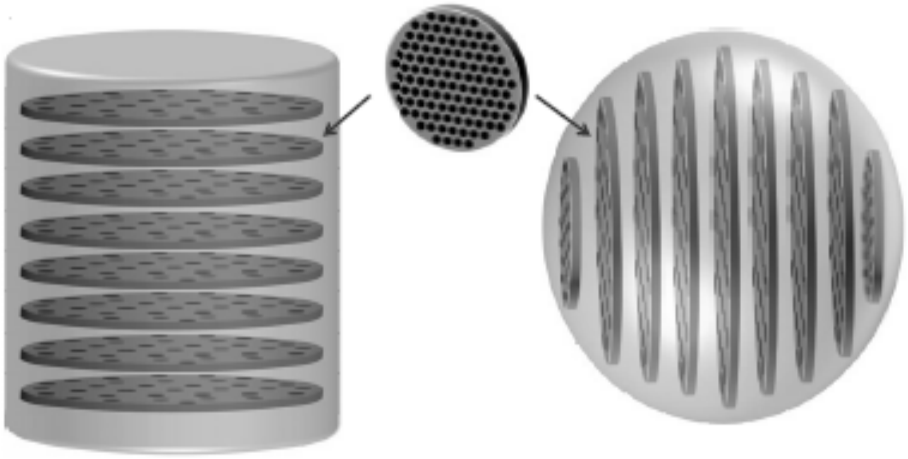

Figure 8. Neutron spectrometer concept based on matrix of semi-conducting BC diodes in a moderating volume [10].

A final consideration for neutron detection is the ability to discriminate between a neutron and gamma interaction in the detector [12]. A BC based detector has two advantages in this area. First, due to the low Z of its constituents, the cross-section for the photoelectric effect is much lower than other semiconductors and neutron detection media, with the exception of ^{3}He as

shown in Figure 9 [10]. Second, as noted above, BC detectors would require a very small depletion width (< ten microns or less) in comparison to the mean free path of gammas in BC (~4cm for 100 keV gamma). These factors permit for energy threshold based gamma discrimination instead of more complicated techniques required in other neutron detectors.

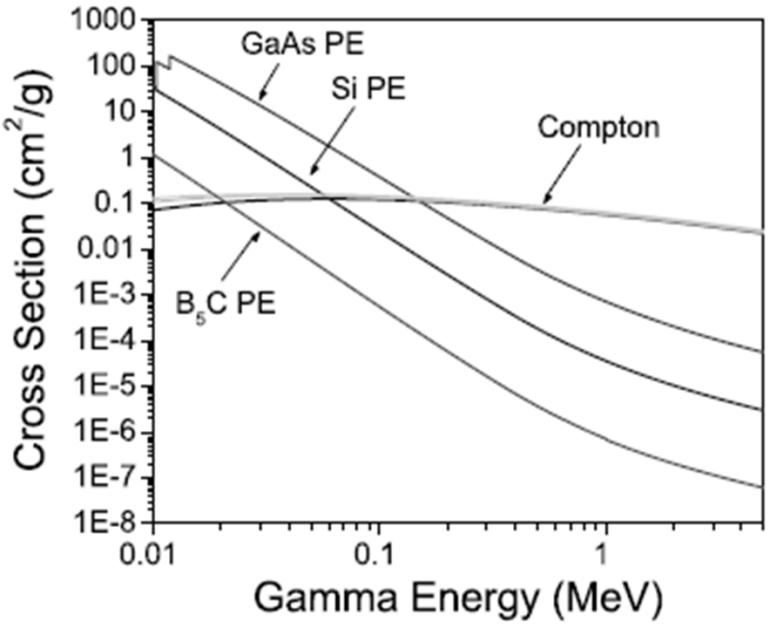

Figure 9. Photoelectric and Compton scattering cross-sections of various semiconductor materials [10]. Other proposed solid state neutron detectors such as Gd_2O_3 would have even higher cross-sections.

BC neutron detection diodes have the desirable characteristics of low power and high efficiency not currently available for other portable neutron detectors. The additional possibility of real-time neutron spectroscopy through an array of BC diodes is especially attractive for the detection of SNM in that

spectrum discrimination can be used in addition to gross neutron counting to reduce false positives and false negatives [9]. It is noteworthy that although SNM applications are the primary initiator for this research, potential applications for a low bias, high efficiency neutron spectrometer abound from reactors, to laboratories, to treaty verification.

However, none of this will be possible without advancing the current state of BC diode technology. Recent work by the AFIT, UMKC, and UNL (AMN) group and others has focused in the areas of improvements in device fabrication [14,15], investigation of physical parameters [14,16,17,18,19,20], detector characterization [21,22], and spectrometer optimization [23,24]. Little systematic work in the area of BC diode optimization has been reported [10,25]. Additionally, little knowledge exists regarding radiation damage in boron-rich solids, and no results have been reported for p-type a-B_5C:H_x thin films on n-type silicon (Si) diodes [26,27]. As such, this work focused on advancing the current p-type a-B_5C:H_x thin films on n-type Si diode technology through optimization using semiconductor industry standard software packages and understanding the radiation induced degradation that would occur during normal anticipated usage of these diodes.

1.2 Objectives of Research

Previous studies of B_5C neutron detectors have used inefficient diodes aimed primarily at demonstrating proof-of-principle detection in these devices [10,13,21,28]. However, to develop state-of-the-art neutron detectors using p-type a-B_5C:H_x thin films on n-type Si diodes, the optimization of these devices for detection characteristics must be studied. In particular, the effect of varying bias, BC thickness, silicon thickness, BC resistivity, and silicon resistivity on the signal-to-noise ratio (S/N) and charge collection (Q) for both the BC and silicon contact was determined using the Synopsys Technology Computer-Aided Design (TCAD) software package [29]. These results were combined with detection efficiency calculations performed using the Geometry and Tracking (GEANT) software. The combination of these two results was used to determine the maximum theoretical performance and optimal build parameters for BC diodes.

Although the optimization of BC diodes is the primary goal of the TCAD and GEANT modeling, the development of a method to optimize semiconducting detectors accounting for both semiconductor and nuclear physics is just as relevant. The methods used (outlined in Chapter III) can be applied to other potential semiconductor detectors. In fact, anywhere nuclear interactions are of interest to semiconductor device function, such as beta-voltaic batteries or single event upset (SEU) mitigation, the method developed here

could be adapted to realize greater device performance. Finally, this model can be updated to reflect the current knowledge of BC physics as more research is performed in this area.

Semiconductor devices exposed to neutron and heavy ion radiation suffer degradation through non-ionizing energy loss (NIEL) events. Although the damage in silicon from (NIEL) events such as neutron collisions has been extensively studied for decades, little research has been done on radiation induced damaged to BC and no known research has been performed in the area of radiation effects for p-type a-B_5C:H_x thin films on n-type Si diodes. The focus of this research was to determine the rate limiting factors affecting diode performance degradation and quantify the point at which that performance degradation could be expected. In particular, was device degradation consistent with silicon, or does the interface and/or BC displacement damage govern the rate of degradation?

Overall, the combination of expected device lifetime from the irradiation studies along with the optimization results provided valuable insight into the optimal build for future generation BC diodes.

1.3 Limitations of Research

The optimization study at this time will be limited to computational methods benchmarked using a limited set of data available at the time of the

model compilation. However, the variable nature of devices grown at different locations – and to a lesser extent, those grown in the same location – limits the development of a quantitatively precise predictive model [9,21,25]. Until future refinements in device fabrication allow for reproducible results, the results obtained from models will be more useful qualitatively than they will be quantitatively. For this reason, S/N and Q are normalized and trends are analyzed more than specific quantitative results.

Furthermore, the computational software used to model the BC diode's electrical transport are based on known, or ranges of known, parameters. For this reason, gaps in the knowledge base for these devices may lead to inaccuracies when using the model for extrapolation to the various builds and operating conditions studied. In some cases, physical parameters did not exist in the literature and had to be deduced based on benchmarks and calculations. Future research into electrical transport in BC will allow for further refinement and improvement of the model.

The major limitation facing the characterization of radiation-induced degradation of BC diodes is the limited availability of samples for irradiation. The samples obtained varied significantly from device to device resulting in the inability to perform fast neutron and alpha irradiations as intended. This resulted in a limited data set of only thermal neutron irradiations from which to

draw conclusions. Additionally, time constraints in reactor operation and the procurement of silicon wafers and BC diodes limited the total deliverable fluence to each diode. In the absence of a robust data set, unambiguous conclusions are difficult to obtain and the results may be better served as a scoping study rather than the definitive answer to the research objectives proposed above. Nonetheless, the results provide valuable insight into the possible limitations that can guide future development and provide a rough benchmark of what can be expected in terms of radiation hardness going forward.

II. Theory

2.1 Semiconductor Properties

Any model is only as good as the physics upon which it is based. As such, an exhaustive search of the literature was performed to determine the best basis on which to construct the TCAD model. The theory included in this section is intended to provide an experimental and theoretical basis from which the TCAD models were developed. It is worth noting that semi-conducting BC exists in many forms. The particular form used by the AMN group, a-B_5C:H_x thin films, is perhaps the least well referenced in literature in terms of physical properties. A majority of the literature references are based on icosahedral or rhombohedral crystalline BC. When discussing the physical parameters, care is taken to note to which form it pertains. In general, a-B_5C:H_x thin film properties were used in the model development where available.

2.1.1 Structure

Boron carbide comes in several forms with differing B:C ratios. The work done by Werheit, Wood, Emin, and others focused on crystalline boron carbide with B:C ratios ranging from 4.3:1 to 11:1 [26,30,31,32,33]. The BC precursors used by the AMN group utilize the $C_2B_{10}H_{12}$ (B_5C) carborane molecule [10,34,35]. For clarity, B_5C will be used when specifically referencing the $C_2B_{10}H_{12}$ carborane molecule while BC will be used in a more general and all encompassing sense.

The structure of crystalline BC varies from icosahedral-type structures to complicated rhombohedral structures as shown in Figure 10 [26,36]. Detailed information on the various structures is not of high importance to this work, but it is noteworthy that the icosahedral structure is the primary conduction mechanism and is common to all three structures (icosahedral BC, rhombohedral BC, and B_5C) [16,31,32,37]. Therefore, in areas where physical parameter data does not exist for B_5C, it is reasonable to believe that those of the other BC species would be similar and could serve as a sufficient starting point.

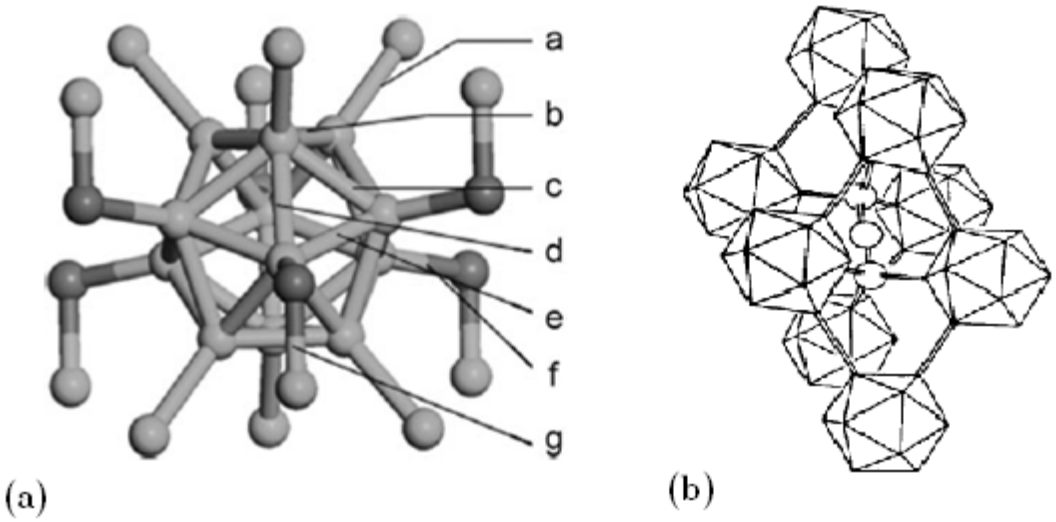

Figure 10. Schematic representation of (a) icosahedral and (b) rhombohedral boron carbide [26,36]. (a) a-g indicate angles which vary based on B:C composition [36].

The closo-carborane molecule forms a slightly distorted icosahedron cage due to the presence of the two carbon atoms [38]. The carbon atom acts as an

electron donor in the carboranes resulting in isomers of the $C_2B_{10}H_{12}$ molecule based on the carbon atoms' position [38]. Figure 11 shows the molecular structure of ortho- and meta-carborane atoms [38]. A unique consequence of these isomers is that they form different majority carrier semiconductors. Meta-carborane (closo-1,7-dicarbadodecaborane) forms an n-type semiconductor while ortho-carborane (closo-1,2-dicarbadodecaborane) forms a slightly p-type semiconductor [39]. This presents a unique opportunity in that detection diodes can be formed without conversion layers thereby enhancing charge collection capabilities [10,22]. Additionally, it is possible to create a heteroisomeric diode formed utilizing ortho-carborane and meta-carborane [39].

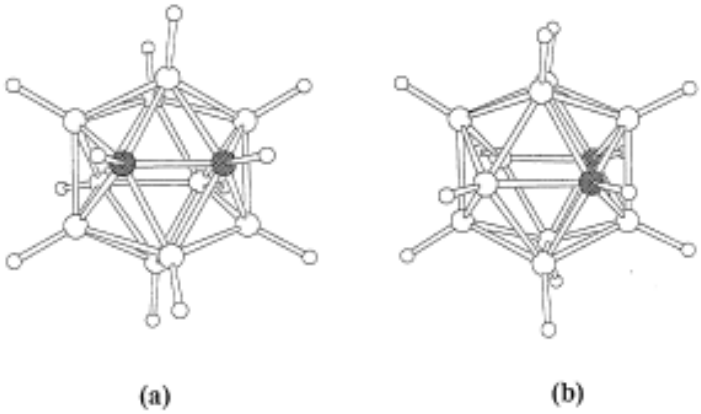

Figure 11. Molecular structure of (a) ortho- and (b) meta-carborane $C_2B_{10}H_{12}$. Carbon atoms are shaded [38].

Ortho-carborane deposited by plasma enhanced chemical vapor deposition (PECVD), see Section 2.2 for further details, forms an amorphous BC

semiconductor often denoted as a-B_5C:H_x. A schematic picture of this structure is shown in Figure 12 [9]. As will be discussed in Sections 2.1.2-2.1.3, this amorphous nature does affect several key electrical transport properties.

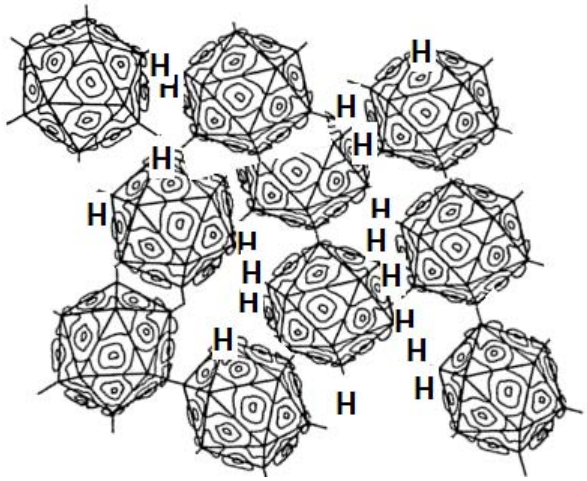

Figure 12. Schematic picture of the a-B_5C:H_x structure [9].

2.1.2 Boron Carbide Electrical Transport

Essentially, two over-arching theories exist to explain the semiconducting nature of BC. The first, proposed by Emin et al., is based on bipolaron hopping [40,41]. This theory assumes that extra holes present in the crystal structure due to the high electron deficiencies common to BC create bipolarons which hop between BC icosahedra [26,42]. However, much of the recent experimental evidence is contradictory with this theory of transport in BC [37,42].

The second theory, developed by Werheit et al., is based on theoretical band structure calculations. The band structure was modified to account for

experimental results. The resulting band diagram is shown in Figure 13 [43]. In this theory, the semi-conducting nature is derived from the high density of anti-site and vacancy defects [42]. These defects are correlated with the high density of gap states split off from the valence band - on the order of 0.1 to 1 per elementary cell (~3×10^{21} elementary cells cm^{-3}) - shown in Figure 13 [43,44]. The resulting Fermi level is affixed within these split-off gap states, thereby determining the p-type semiconducting behavior of most BC [43]. It is this theory that will provide the basis for most of the following discussion. Any experimentally determined differences in B_5C will be explicitly noted.

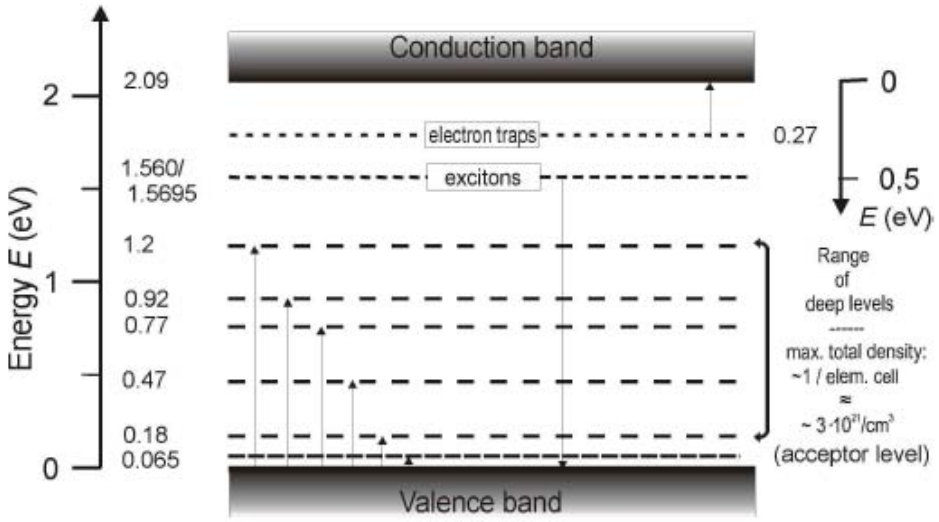

Figure 13. Band diagram for BC proposed by Werheit [43].

It is at this point that the first possible disagreement exists between the BC and B_5C data available in the literature. The band gap of B_5C, with varying

B:C content ratios, was determined through optical absorption measurements, as shown in Figure 14, and is seemingly at odds with the ~2.09 eV band gap shown in Figure 13 [35,43]. However, it is unclear if the ~0.9 eV B_5C band gap indicated by the optical absorption measurements is an indirect interband transition from the valence to conduction band or a non-direct transition between the gap states and conduction band. Werheit does note several non-direct transitions determined through optical absorption in polycrystalline BC ranging from 0.47-2.09 eV (one of which is a 0.92 eV transition) [43]. However, any direct comparisons between the experimental results are limited due to the differing crystal types (amorphous vs. polycrystalline) and the lack of mention of other optical absorption transitions for a given B:C ratio in Dowben's work [35,43].

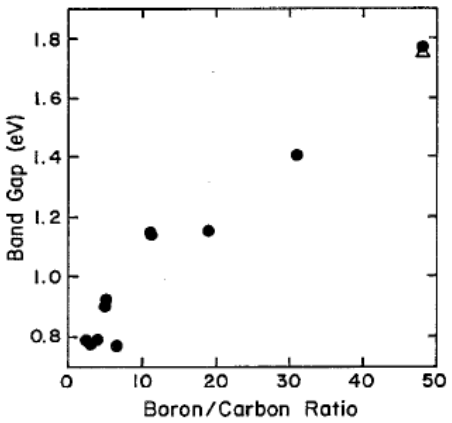

Figure 14. Band gaps determined by optical absorption measurements (circles) and photoluminescence (triangle) for B_5C thin films grown by PECVD [35].

The result of the high electron deficiency induced gap states is a high carrier concentration on the order of 10^{18}- 10^{19} as shown in Figure 15 [42]. These carriers are transported in boron carbide due to hole hopping processes within the partially filled gap states [16]. The hopping transport mechanism is superimposed with a contribution from Drude-type free holes [32,45]. The contribution from free carriers is highly dependent on thermal, optical, or radiative excitation of valence electrons into the gap states [42].

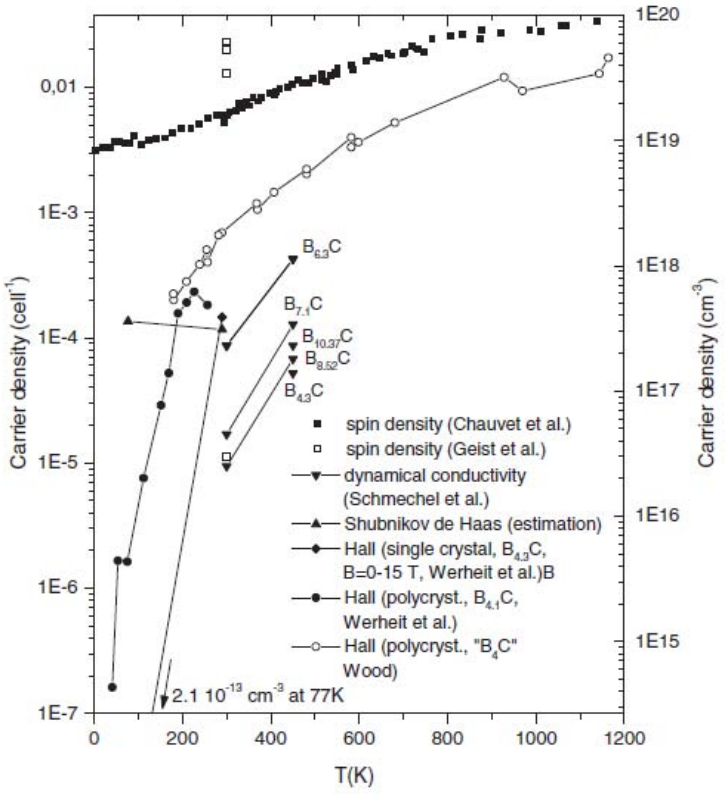

Figure 15. Comparison of carrier densities as a function of temperature determined by different experimental methods for various boron carbide structures. The dynamic conductivity and Shubnikov de Hass values are for free hole densities [42].

A related parameter of electronic transport, the effective mass of carriers, has been experimentally determined to be ~$10m_0$ for the effective mass of free holes and to be ~$3\text{-}10m_0$ for mobile carriers [16]. This is at odds with unpublished work by Dowben, which indicates the effective mass of electrons and holes to be ~$1m_0$ for amorphous B_5C [46].

While untrapped drift mobility is estimated to be quite high (565 $cm^2\ V^{-1}\ s^{-1}$), the large number of gap states creates a high trapping probability such that BC mobility is on the order of 1 $cm^2\ V^{-1}\ s^{-1}$ at room temperature as shown in Figure 16 [42]. However, the B_5C mobility, determined from charge collection times typical of p-type a-B_5C:H_x thin films on n-type Si diodes exposed to a neutron field, is on the order of $10^{-2} - 10^{-4}$ $cm^2\ V^{-1}\ s^{-1}$ [21]. The reduced mobility in B_5C thin films is likely due to the amorphous nature resulting in a higher number of defect sites within the film than would be present in poly- or mono-crystalline BC.

Although information exists regarding the approximate location of traps within BC as shown in Figure 13, no information was available in the literature regarding the density, type, or capture and emission cross-sections of each state [37,43]. This is a significant gap in the knowledge base considering that the semi-conducting nature of BC is derived from these states through hopping and Drude type transport.

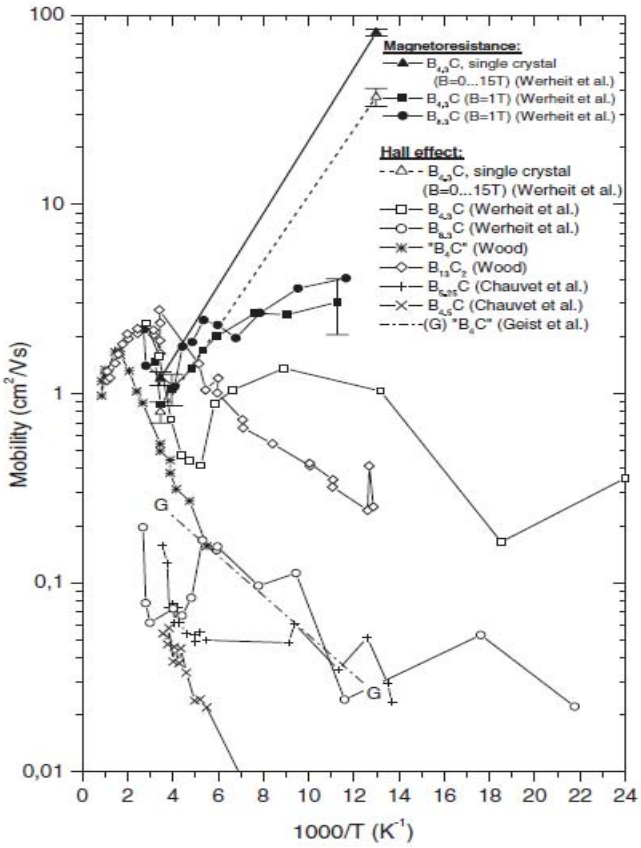

Figure 16. Boron Carbide carrier mobility determined by different experimental methods and authors [42].

2.1.3 Heterojunction Physics

The bulk of BC diodes constructed to date have been based on p-type a-$B_5C{:}H_x$ thin films on n-type Si heterojunctions (see sections 2.4.1 and 2.4.2 for further discussion). As such, the models developed are based on this geometry. Certain physical parameters of interest to device physics are referenced infrequently, if at all, in the BC transport literature. Of interest here are the intrinsic effective doping, N_A; the electron affinity, χ; the dielectric constant, ε; and the built-in voltage, V_{bi}.

The effective doping of BC is not referenced in the electronic transport literature. Instead, the only value available was determined indirectly through capacitance measurements of B_5C diodes grown by the University of Nebraska-Lincoln (UNL) [21]. From the slope of C^2 versus $1/(V_{bi} - V_{app})$, a value of 4.5 x 10^{12} cm^{-3} was obtained for N_A [21]. Similarly, by plotting $1/C^2$ versus V_{app}, a value of 0.7 V was obtained for V_{bi} [21]. Similar results were not available for the UMKC growth process at the time of this writing (nor was the UMKC growth process fully mature), but it is anticipated that these values would be very similar as both use PECVD growth of ortho-carborane on n-type silicon.

Another defining parameter of the electronic band structure is the dielectric constant. This value is again one that differs in the literature. Werheit and Emin report a value of ~10 while Hong et al. report a value of ~8 [15,26,43]. Since the value of 8 for ε is from a group utilizing B_5C, this value is used for the device models.

Perhaps the largest gap in the knowledge base for BC properties is the electron affinity [15]. While no value is specified in the literature, Emin, Werheit, and Clark expect the value to be high due to the weak screening of the nuclear charge and electron deficient nature of BC [26,37,47,48]. To come to a reasonable value, flat-band heterojunction analysis was performed and is

included in Appendix A. A typical heterojunction flat-band diagram is shown in Figure 17 [49]. Through this analysis, a value of 4.58 eV was obtained for χ.

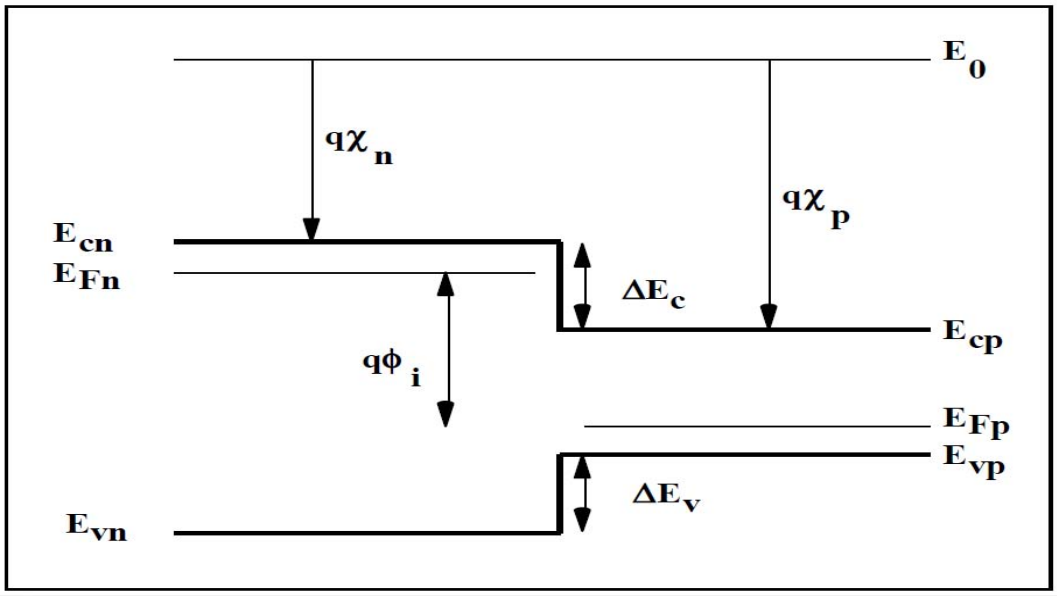

Figure 17. Heterojunction flat-band diagram [49].

2.2 Diode Growth

B_5C diodes utilized in this research are p-type a-B_5C:H_x thin films on n-type Si. Although several techniques exist to grow BC thin films, the PECVD technique is utilized by the AMN group and others [34,35,50]. The steps and equipment utilized in the growth process are shown in Figure 18 [5]. The diode growth is performed on a <100> or <111> silicon substrate using a closo-1,2-dicarbadodecaborane ($C_2B_{10}H_{12}$) precursor [51,52]. Custom designed parallel-plate radio-frequency plasma reactors were used to perform the deposition of the

B_5C thin films [51]. Using this method, B_5C layers are grown up to 22 μm thick [5].

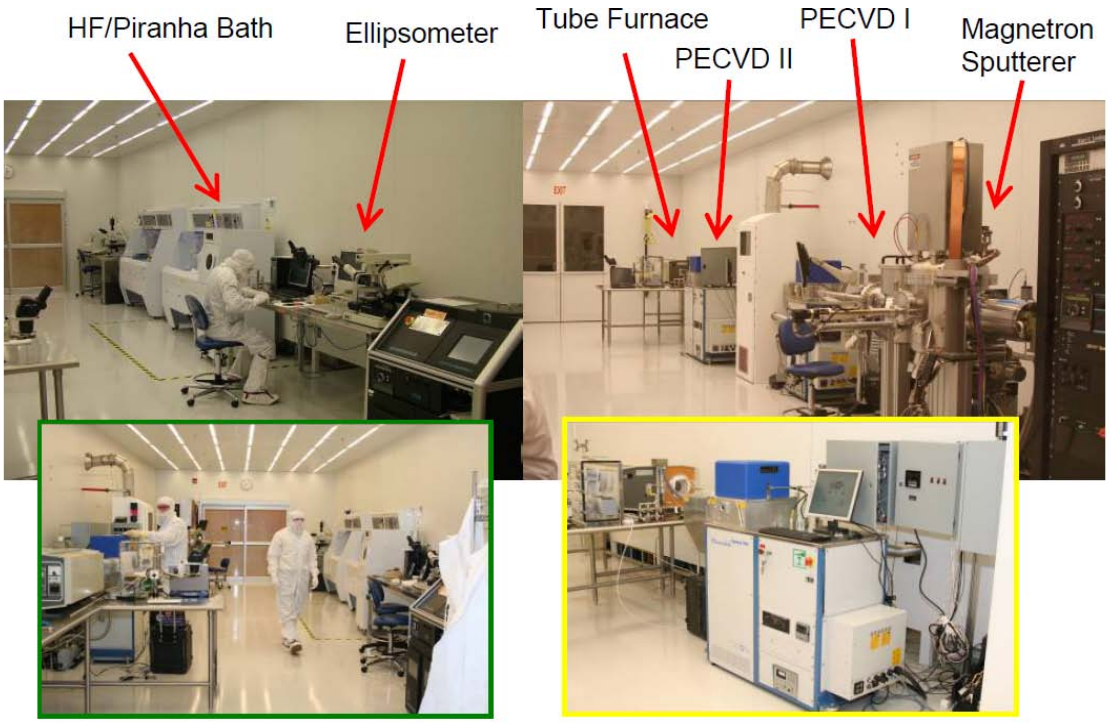

Figure 18. Equipment necessary in the B_5C diode growth process [5].

Although not utilized in this research, it is worth noting that in addition to intrinsically n- and p-type carboranes, it has been shown that it is possible to dope ortho-carborane to an n-type semiconductor using phosphorus and nickel [15,52,53].

2.3 Diode Response to Ionizing Radiation

When radiation interacts in matter, the interactions can be classified into two broad categories: ionizing energy loss events and NIEL events [12,54]. In

semiconductors, the ionizing energy loss events create e-h along the track of the ionizing radiation [54]. The creation of these e-h is governed largely by the band gap of the semiconductor in which they were created, as shown in Figure 19 [55]. It is here that the band gap discrepancy noted in Section 2.1.2 has perhaps the most significant irreconcilable impact. While benchmarks such as current and capacitance can be used to validate the parameters chosen, no such data currently exists for ensuring the correct charge generation within the model. As such, the e-h created in the B_5C layer could vary by as much as a factor of two.

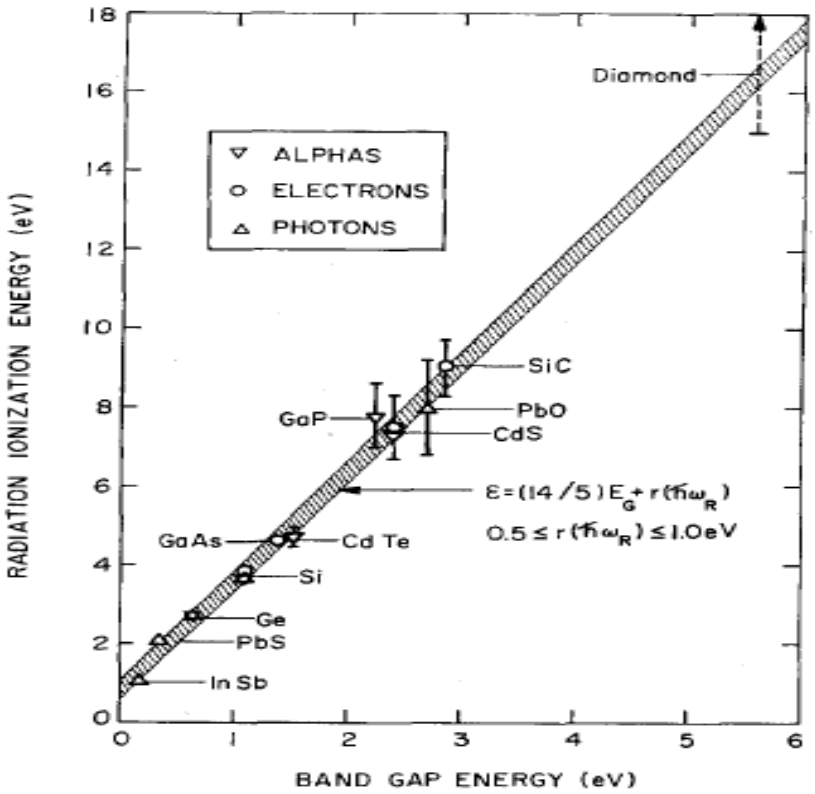

Figure 19. Energy required to create e-h as a function of band gap [55].

It is worth understanding how the e-h pr generation is accomplished in the models since it is here that expectations deviate most from standard equations and definitions. TCAD models this process by computing the generation rate by

$$G(l,w,t) = G_{LET}(l)R(w,l)T(t), \tag{3}$$

where l is the track length in cm, w is the radius perpendicular to the track in cm, and t is the time in seconds. G_{LET} is the linear transfer generation density in e-h prs cm^{-3} and a user definable parameter. $R(w,l)$ is the spatial distribution that can be specified as a Gaussian function such that

$$R(w,l) = \exp\left(-\left(\frac{w}{w_t(l)}\right)^2\right), \tag{4}$$

where w_t is a user definable characteristic distance in cm. $T(t)$ is the Gaussian temporal variation given by

$$T(t) = \frac{2\exp\left(-\left(\frac{t-t_0}{s_{hi}}\right)^2\right)}{s_{hi}\sqrt{\pi}\left(1-erf\left(\frac{t_0}{s_{hi}}\right)\right)}, \tag{5}$$

where t_0 is the moment of heavy ion penetration into the device in seconds (user controllable) and S_{hi} is the characteristic value of the Gaussian in seconds (user controllable) [29]. The TCAD heavy ion models require these inputs be

determined elsewhere to accurately model the electrical transport of the e-h created from the boron capture event.

Diodes in reverse bias serve as suitable detectors due to the rapid collection of these radiation induced e-h. The collection results in a transient current signal that can be distinguished from the steady-state leakage current if the leakage current is sufficiently low. For this reason, and to have good S/N characteristics, a commonly accepted value for detector leakage current is on the order of 10^{-9} A [12]. Current B_5C diodes have demonstrated leakage currents on the order of 10^{-8}-10^{-9} A at low biases with device areas on the order of 0.1 cm^2 or less [21].

Due to the large deposition of energy possible from a boron neutron capture (minimum of 2.31 MeV of heavy ions created), idealized scoping calculations show that it is possible to achieve a peak current pulse of ~10^{-6} A from a single interaction in silicon while the same interaction in BC yields a peak current pulse of ~10^{-9} A. The three orders of magnitude difference is due to the large variation (maybe as much as six orders of magnitude) in mobility between BC and silicon. The transient current was calculated using

$$I_{Transient} = 2\frac{E_{dep}q}{E_{pr}(t_{trans} + t_{plasma})}, \quad (6)$$

where E_{dep} is the energy deposited [eV], q is the fundamental charge [C], E_{pr} is the energy required to create an e-h pr [eV], t_{trans} is the time to collect the generated charge carriers [sec], and t_{plasma} is the time in seconds required to disperse the cloud of e-h such that they do not self-shield (~2-5ns [12]). The charge collection time was found from

$$t_{trans} = \frac{d}{\in \mu}, \tag{7}$$

where d is the distance for charge collection [cm], $\in$ is the electric field [V cm^{-1}], and μ is the mobility [cm^2 V^{-1} s^{-1}].

This large divergence of the current response in the two materials is a main reason for the optimization. As can be seen from the above discussion, the factors which can be used to achieve minimum detectable level (MDL) requirements for S/N are exactly opposite of the desired changes necessary to improve efficiency (i.e. BC thickness).

2.3.1 Conversion Layer Diode

Conversion layer diodes function on the principle of a neutron sensitive layer capping a device as shown in Figure 20 [10]. The secondary capture products scatter and deposit energy in the underlying semiconductor which collects the charge. This device is limited in overall efficiency as illustrated in Figure 21[56]. Despite limitations in overall efficiency, conversion layer devices

benefit from using well-defined, mature underlying semiconductors that can be precisely grown and manufactured [10]. Additionally, many of the benefits previously noted for BC direct-conversion diodes such as low bias operation, "gamma blindness", and spectrometer potential also apply to conversion layer detectors.

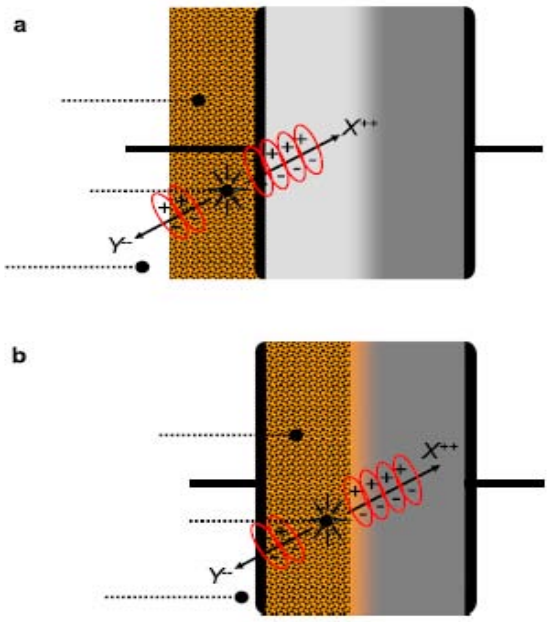

Figure 20. Representation from neutron transduction from (a) conversion layer and (b) direct-conversion solid-state p-n junction heterostructures [10].

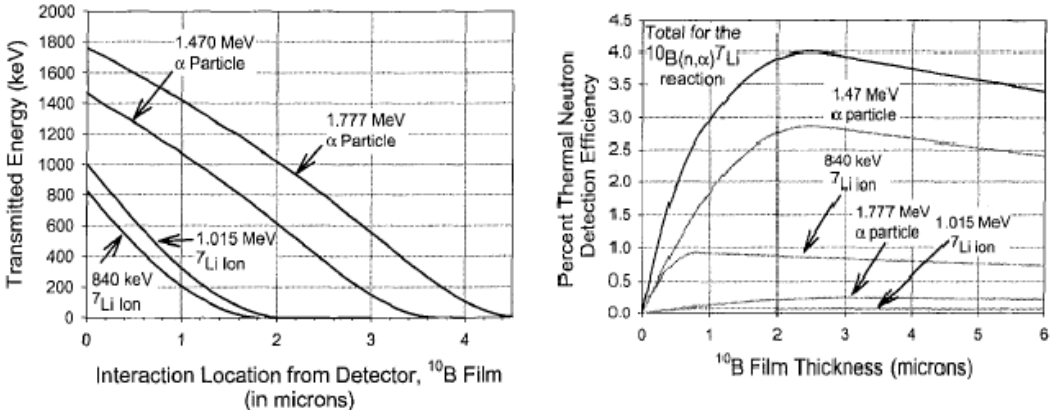

Figure 21. Representative calculations for conversion layer devices showing (a) energy loss as capture event originates further from detector and (b) decreases in detector efficiency despite increasing capture efficiency [56].

2.3.2 Direct-Conversion Diode

By using semi-conducting carboranes, the necessity of using a conversion layer is avoided. Conversion layers introduce low energy tailing indicative of less energy collection in the diode region due to a maximum of one charged particle being collected in the active region of the diode as shown in Figure 20 and Figure 21 [22]. However, by using a heteroisomeric, homojunction, or heterojunction diode, increased charge collection can be obtained by making the BC part of the active charge collection volume of the diode. This principle is illustrated for a neutron capture in a BC on Si direct-conversion diode in Figure 22 [22]. The low mobility for electrons and holes in boron carbide (as low as 10^{-2} – 10^{-4} for both) limit the charge collection efficiencies and lead to much longer charge collection times as compared to silicon [21]. Nevertheless, the removal of

the efficiency cap placed on conversion layer devices is an enormous advantage for direct-conversion devices.

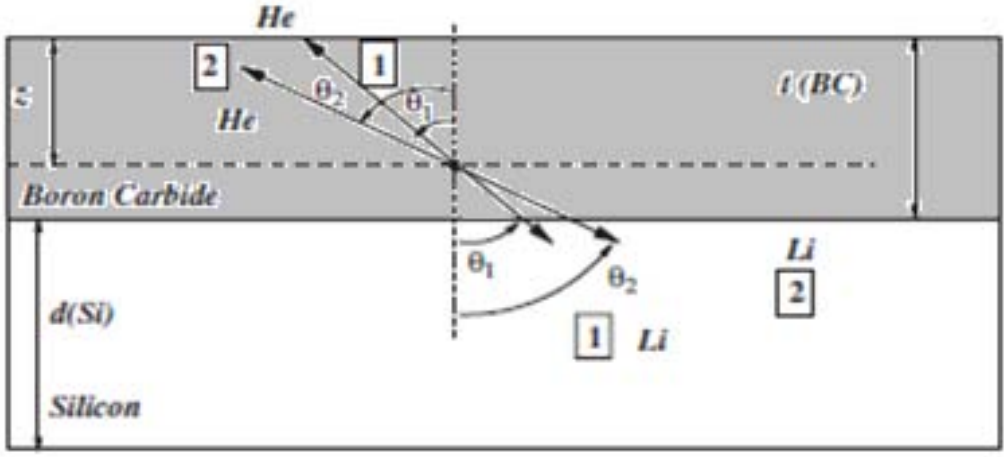

Figure 22. Two representative neutron capture events in a BC (grey shaded area) on Si direct-conversion diode where potentially all, or a significant portion, of the deposited energy can be collected [22].

2.4 Previous Boron Carbide Diode Results

Numerous BC diodes have been constructed and tested [10,14,25,28,35,39,51]. While variations such as B_5C on silicon carbide have been built [51], the following discussion will focus on B_5C heteroisomeric diodes and B_5C on Si heterojunction diodes as the items currently of most relevance to this research.

2.4.1 Boron Carbide Heteroisomeric Detectors

B_5C heteroisomeric devices have been built and tested by Caruso et al. [39,57,58]. Due to the entire space-charge region being composed of a neutron

sensitive semiconductor, these devices have vast potential in terms of gains in intrinsic detection efficiency [58]. Also, the difficulties arising from collection times that differ by three orders of magnitude in heterojunction devices are completely avoided in a heteroisomeric diode. The diodes have exhibited diode-like rectification, desirable reverse leakage currents (on the order of nA at low biases as shown in Figure 23), and depletion widths on the order of the track length of the capture products [39,57]. However, difficulties arose in device scaling such that only very large cross-sectional areas, with only a portion being active, could be grown. Since the intended spectrometer application requires small and reproducible diodes as depicted in Figure 8, the p-type a-B_5C:H_x thin films on n-type Si heterojunction diodes have taken the forefront in AMN group's research efforts.

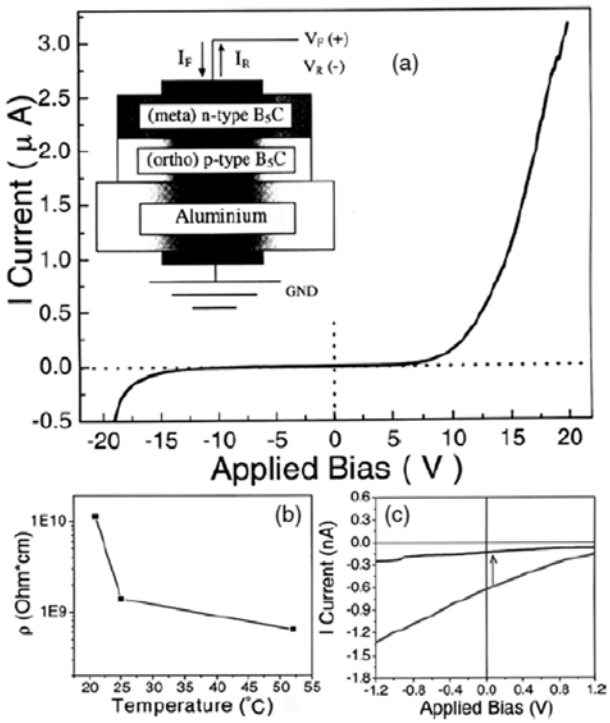

Figure 23. (a) IV characteristics of the isomeric diode. (b) Diode resistivity in reverse bias as a function of temperature. (c) A zero-offset bias is observed in a diode exposed to light, but diminishes in a diode operated in the dark. Inset is a schematic of the diode construction [39].

2.4.2 Boron Carbide Heterojunction Detectors

P-type a-B_5C:H_x thin films on n-type Si heterojunction diodes have been grown by several research groups in the past decade [10,13,14,21,28,59,60]. A scanning electron microscope image is depicted in Figure 24 [5]. Diodes built in this manner have exhibited low leakage currents at low bias (~nA at $<$ -5V) [21,25], neutron detection (albeit at less than ideal efficiencies) as seen in the pulse height spectra from irradiation by reactor neutrons in Figure 25 [10,21,59], and charge collection from both contacts (indicative of B_5C's semiconducting nature) [21].

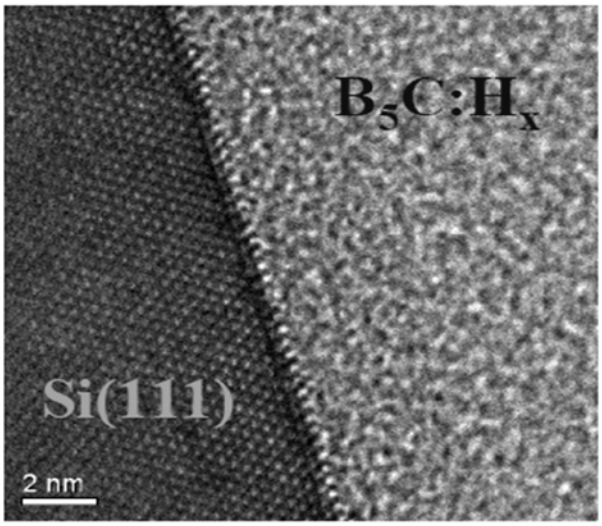

Figure 24. SEM image of a PECVD B_5C on Si heterojunction. Note the disordered nature of $B_5C:H_x$ in comparison to that of silicon [5].

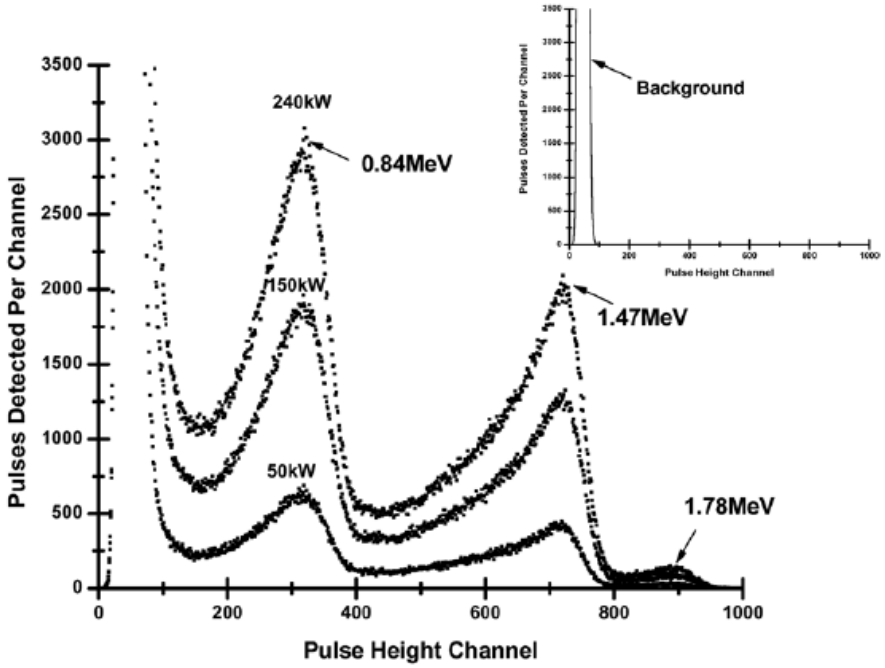

Figure 25. Pulse height spectra from a B_5C heterojunction detector. Each spectra was collected for 600 seconds at the indicated reactor powers. The three identifiable peaks (The 1.02 MeV peak is lost in the continuum between the 0.84 and 1.47 MeV peaks due to its branching ratio) are attributable to the boron capture products as shown in (1) and (2). The inset indicates the background spectra [59].

However, many gaps in the knowledge of the physical and electrical transport parameters have limited the growth of heterojunction diodes capable of >1% detection efficiency [10]. Additionally, the oxygen and moisture sensitivity of the thin films has led to the frequent occurrence of delamination of the B_5C layer [10]. Nonetheless, it is believed that increases in the understanding of the basic physical properties of the B_5C layer, coupled with advances in materials science, will eventually yield a direct-conversion heterostructure diode capable of detection efficiency improvements over solid state conversion layer devices [10].

2.5 Radiation Effects

Any semiconductor is subject to damage from ionizing radiation, non-ionizing radiation, or both [54]. Semiconductors, especially very pure ones, are highly susceptible to non-ionizing knock-on damage. In diodes, ionizing radiation presents a negligible, if any, concern, but the knock-on damage can degrade devices exposed to sufficiently high total dose. The following sections on BC and silicon address the nature of this damage from neutrons and heavy ions and typical levels for the onset of damage based on the available literature. However, that no literature exists regarding radiation effects on the interface formed from a-B_5C:H_x thin film on Si heterojunction. Often, the physics of the interface damage dictate the device's response [54,61].

2.5.1 Boron Carbide

As a semiconductor, BC is relatively new. However, it has been used for decades in the reactor industry in control rods. From this usage, material structure based studies are available. Of primary concern is the damage caused by the boron capture products indicated in (1) and (2) [62]. Of the two, helium and lithium, helium gas bubbles appear to cause the most damage [62]. This phenomenon is illustrated in Figure 26 where the helium bubbles and resulting strains and cracks are clearly evident under magnification [62]. While this damage mechanisms would have a detrimental effect on a crystalline semiconductor, the impact on a disordered and amorphous semiconductor such as B_5C (see Figure 24) is less clear. From first principles, it would appear that very high levels of irradiation (on the order of the intrinsic defect density) would be needed for the damage caused by the boron capture products to be of a concern for electrical transport due to the high number of gap states (defects) present in amorphous semi-conducting B_5C.

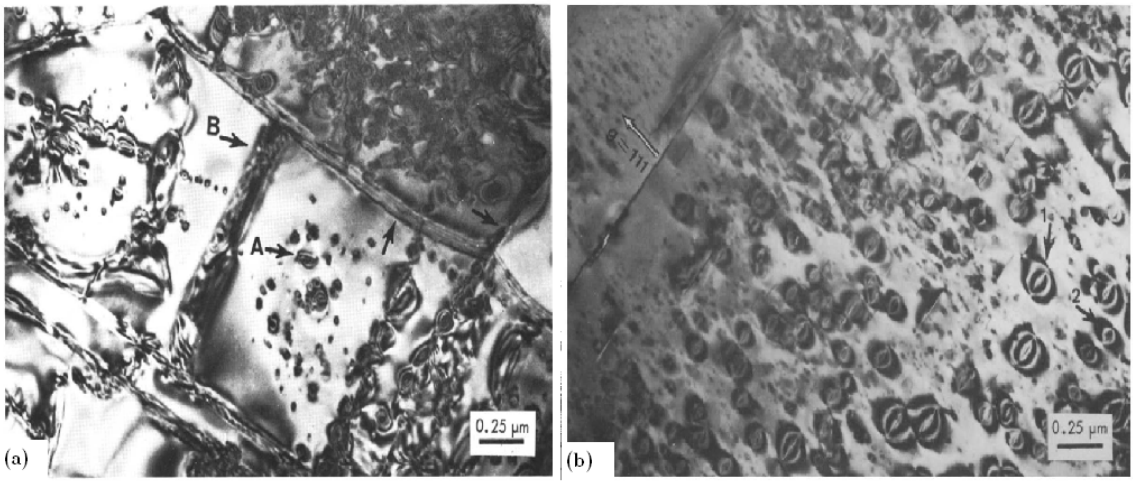

Figure 26. Damage in neutron irradiated BC. (a) A indicates strain fields around helium bubbles and B shows cracks formed from helium bubble coalescence on pre-existing faults. (b) Helium bubbles in BC [62].

Studies performed on variants of icosahedral boron-rich solids have also indicated a high level of radiation hardness [26]. As shown in Figure 26, even in experiments where radiation bombardment was carried out at low temperatures, ~12K, damage such as clustering of defects and amorphization that are typical of common semiconductors was not observed with high-resolution transmission electron microscopy [26]. While this is by no means definitive, such results strongly support the notion that BC is highly resistant to radiation.

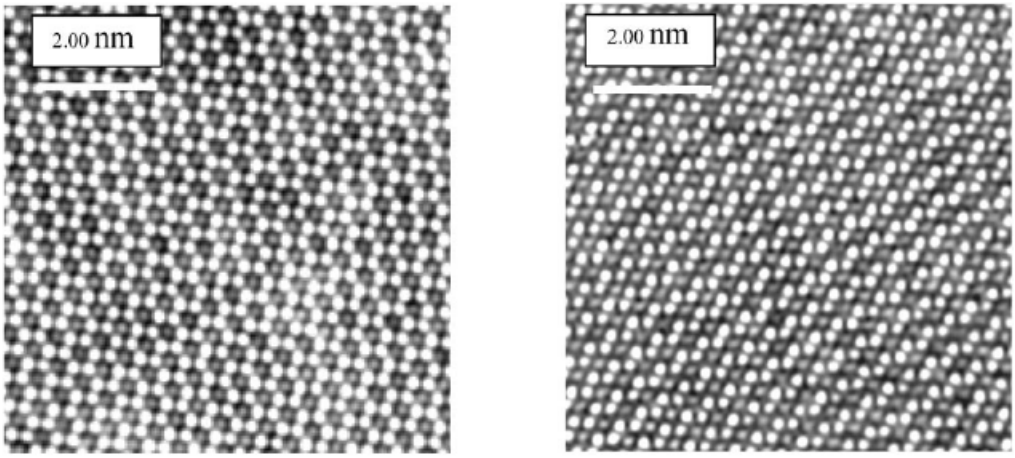

Figure 27. Very high-resolution transmission electron microscopy shows no damage to $B_{12}P_2$ after bombardment (10^{18} electrons cm^2 s^{-1}) by 400 keV electrons to a total fluence of about 10^{23} electrons cm^2 [26].

This apparent lack of radiation damage from irradiation far in excess of those expected to cause damage, based on defect densities alone, indicates that icosahedral boron-rich solids are very adept at annealing out radiation induced damage ("self healing") [26,27]. For this to be the case, displaced atoms must have a mechanism to readily return to the icosahedron. It has been noted that icosahedra damaged by the loss of an atom have a negative charge, indicating the retention of one of the electrons from the displaced atom [27]. The retention of this electron causes Coulomb attraction to promote recombination between a departing boron cation and an icosahedron anion aided by the relatively high

diffusion due to the small size of the cation in comparison to the icosahedral structure [26].

2.5.2 Silicon

In some ways, however, the discussion of BC damage is likely little more than an academic exercise when considering a p-type a-B_5C:H_x thin films on n-type Si heterojunction diodes. Due to the high defect density in BC (~ 10^{18} - 10^{21}) from vacancies and interstitials (evidenced by the high number of gap states in the proposed electronic band structure), one would expect very high levels of radiation to be needed to cause significant damage. Silicon, on the other hand, benefits from none of the radiation hardness advantages enjoyed by BC. Also, in contrast to BC, numerous studies have been performed to classify the nature of NIEL damage in silicon. Several damage mechanisms in n-type silicon are discussed below.

Perhaps the most serious potential consequence of radiation damage in silicon is "type inversion". This is only a factor in n-type materials since all types of radiation tend to make the material more p-type [61]. The mechanism for this inversion is two-fold: (1) removal or inactivation of n-type dopants and (2) creation of defects which behave like p-type dopants [61]. In both cases, the effective doping shifts progressively to less n-type until the point at which it completely inverts and becomes increasingly p-type as depicted in Figure 28.

This phenomenon is of such importance to silicon diode detectors that a function to describe the fluence level necessary to cause type inversion has been developed and is given by

$$\phi_{Inv} = 19cm * N_D, \tag{8}$$

where ϕ_{inv} is the 1 MeV neutron equivalent fluence necessary to achieve inversion [n cm^{-2}] and N_D is the donor doping concentration [cm^{-3}] [63,64].

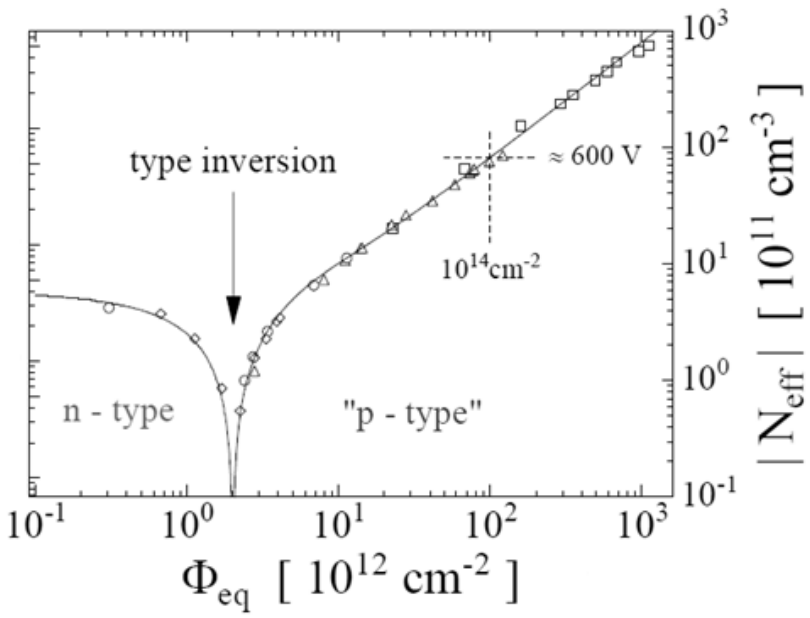

Figure 28. Representative type inversion in high resistivity silicon. Fluence indicated is 1 MeV neutron equivalent [65].

Investigations into the specific damage mechanisms responsible for type inversion have yielded several possible methods of increasing the "hardness" of a silicon based detector [66,67,68,69,70,71]. First, the deep-level defects

responsible for type inversion in n-type silicon only become p-type under bias [67]. Since BC diodes have demonstrated zero bias detection [21,39,59], it is possible that for high neutron environments, this mode of operation, while operating at a reduced efficiency [21], would enhance the lifetime of the BC on Si diode. Second, the primary driver for the type inversion appears to be the formation of the V_20 and V_30 multi-vacancy oxygen complexes (A-centers) [67,68,69,71]. Irradiation of silicon containing high densities of oxygen impurities has shown a reduction in damage by as much as a factor of three as compared to un-oxygenated material [64,72,65,73]. Finally, as demonstrated in (8), through an increase in donor density, and shown in Figure 29, the most effective way to reduce the rate of damage is to decrease the resistivity of the silicon [65,74]. Reduction in silicon resistivity, however, has implications in space charge width (decrease) and charge transport (reduction in mobility) which counteract the accompanying gain in lifetime of the device.

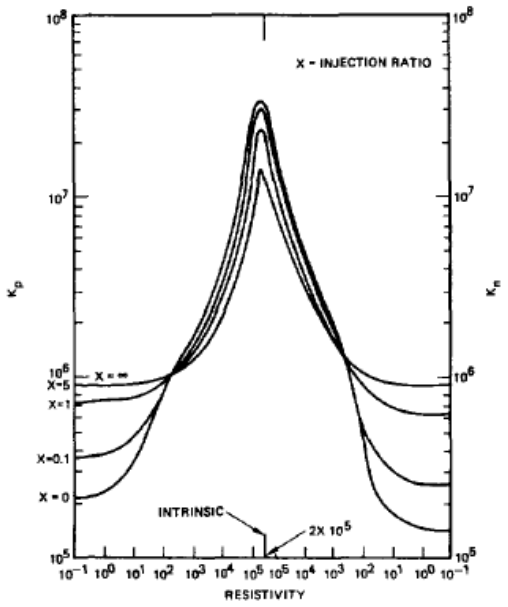

Figure 29. Damage Constant, K, versus resistivity as a function of the silicon injection ratio, x[74].

Another common non-ionizing effect of radiation is the reduction in lifetime, mobility, carrier concentration, and diffusion length of carriers in silicon through scattering and recombination centers introduced into the lattice. Changes of these parameters as a function of irradiation in low resistivity silicon are shown in Figure 30 [24]. The change of each parameter is governed by Messenger-Sprat

$$\frac{1}{\tau} - \frac{1}{\tau_0} = K_\tau \phi, \tag{9}$$

where τ is the lifetime after irradiation in seconds, τ_0 is the lifetime pre-irradiation in seconds, K_τ is the damage constant specific to the material and type of irradiation in cm^2 $particle^{-1}$, and ϕ is the fluence in particles cm^{-2} [75].

The change in each parameter discussed above can be analyzed by substituting the parameter of interest and the corresponding damage constant into (9).

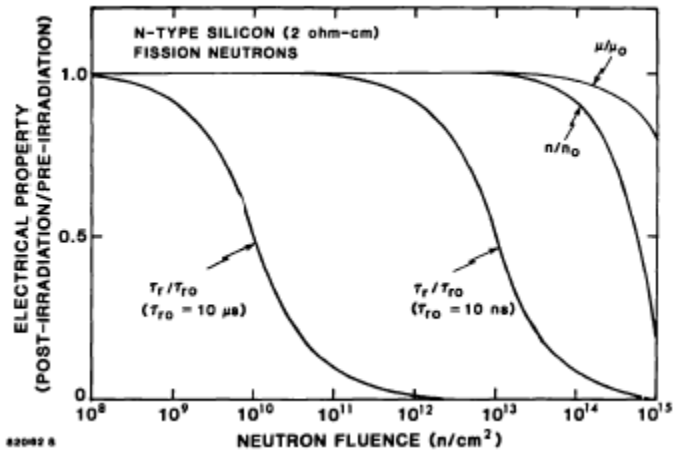

Figure 30. Changes of lifetime, carrier concentration, and mobility in n-type silicon due to neutron irradiation [54].

Another possible effect of radiation induced displacements is the creation of V-V divacancies. These V-V divacancies have been shown to be a facilitator in inter-centre electron-hole recombination that gives rise to large leakage currents [61]. Such increases in the leakage current could significantly degrade the S/N performance of a detection diode. It is significant that the magnitude of this effect, in a similar argument to that presented for BC, is highly dependent on the starting recombination center concentration.

Annealing in silicon is neither as complete nor as rapid as was observed in BC. Figure 31 and Figure 32 show the typical temperatures needed to anneal

various vacancy and interstitial defects created in silicon during irradiation [61]. Unlike BC, very few vacancies or interstitials in silicon anneal at room temperature.

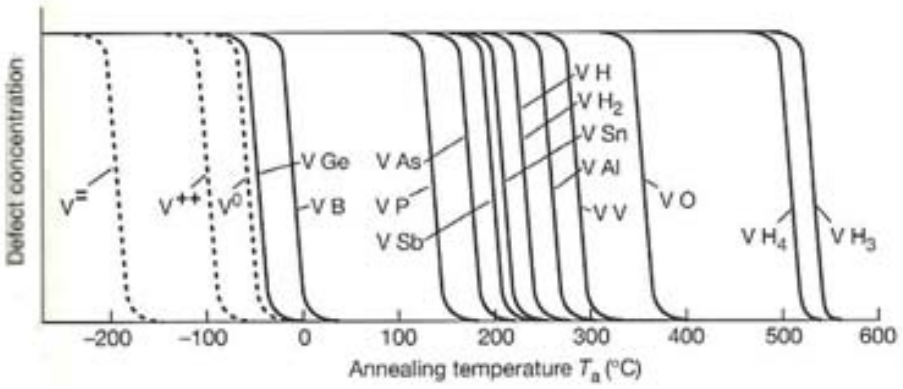

Figure 31. Vacancies and vacancy-defect pair annealing in irradiated silicon [61].

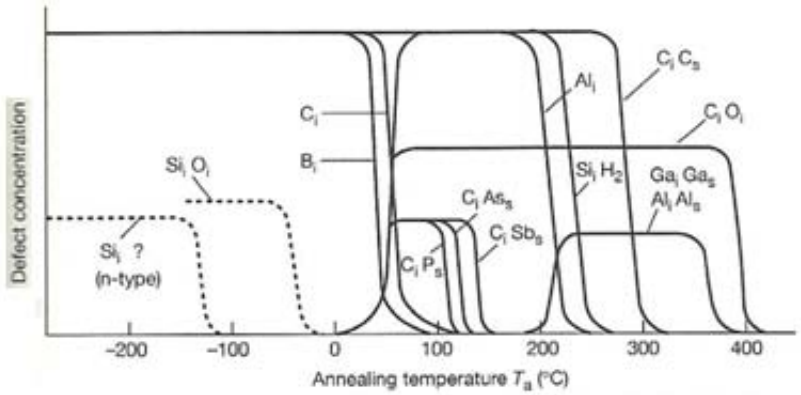

Figure 32. Interstitial defect annealing in irradiated silicon [61].

All of the aforementioned damage mechanisms are manifested in device performance through three primary parameters. First, increases in leakage current are caused by increased bulk current brought about by radiation-induced

generation/recombination levels [61]. This change is illustrated in Figure 33. Second, due to the shift in the effective doping density, N_{eff}, as illustrated in Figure 28, the capacitance (depletion width) initially decreases (increases) to the point of inversion where it subsequently increases (decreases) with increasing fluence [65,76]. Finally, as shown in Figure 34, the charge collection efficiency decreases due to radiation induced charge trapping centers [65]. This decrease is relatively minor in comparison to the reduction in S/N induced by the increase in leakage current in most applications. Prior to type inversion, the change that would most affect detection efficiency and degrade device performance is the increase in leakage current, thereby causing low energy counts that were previously detectable to produce S/N below the MDL.

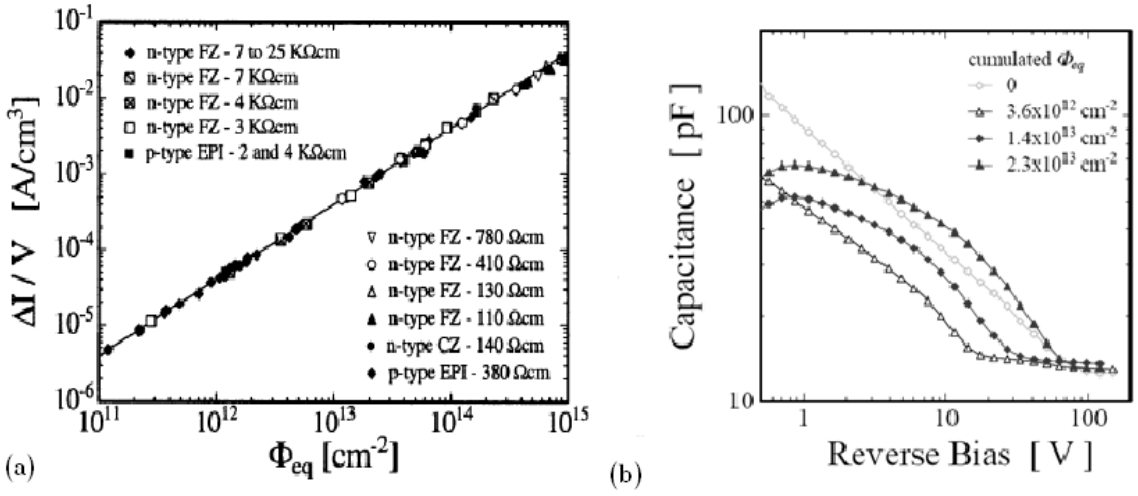

Figure 33. (a) Current density change as a function of 1 MeV neutron equivalent fluence[72]. (b) C-V as a function of 1 MeV neutron equivalent fluence [65].

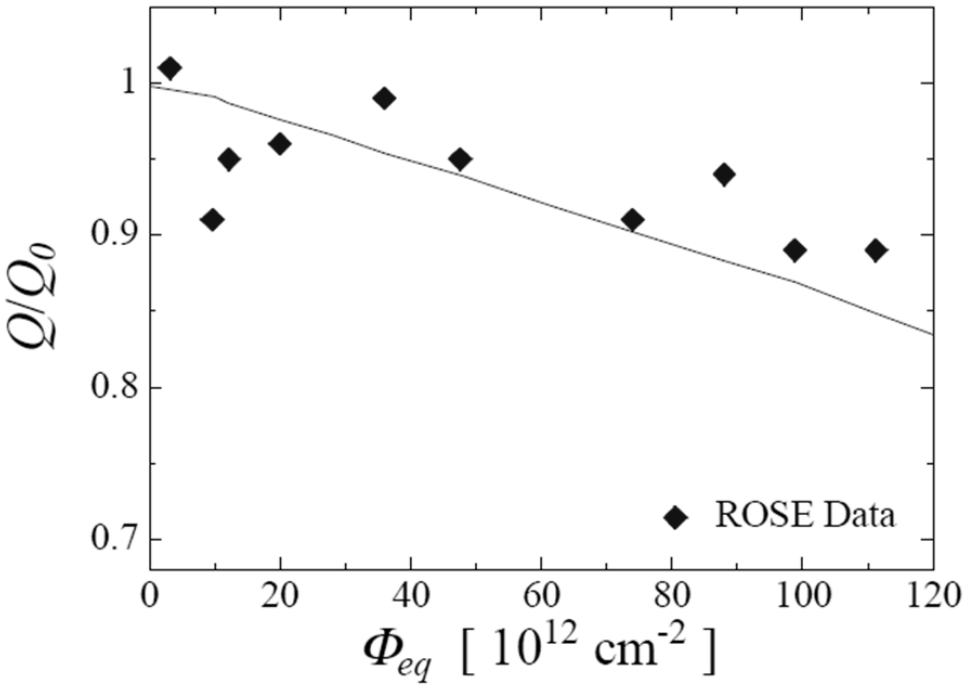

Figure 34. Radiation induced reduction in charge collection efficiency [65].

III. Modeling Methodology

3.1 Overview

In the process of modeling B_5C diodes and their response to a neutron capture event, several simplifications and assumptions were made. Where possible, these were rooted in the best available theory as outlined in Chapter II. It is the goal of the sections of this chapter to identify the decisions and logic employed in the model development.

As noted in Section 2.3, the TCAD heavy ion models required input parameters that had to be calculated using nuclear physics transport models. For this, GEANT and TRIM outputs were used to determine all of the necessary parameters for the heavy ion models.

3.2 GEANT

GEANT is a fully modifiable Monte Carlo based toolkit used for the simulation of a full range of radiation interactions in materials [77]. GEANT was chosen over MCNP because:

1. MCNPX only simulates the resulting ^{4}He boron capture product and
2. MCNP treats energy deposition occurring along μm track lengths as local deposition.

GEANT suffers from neither of these limitations and can track the secondary electrons created by the boron capture products as they ionize the surrounding

materials. The secondary electron energies are ~250 eV with tracks on the nm scale. As such, these particles were treated as local deposition (through cuts set at 500 eV for photons and electrons) in later calculations with no loss in fidelity.

GEANT was used to:

1. Determine the interaction dynamics and energy deposition location of the boron capture products within the B_5C diode as a function of B_5C thickness,
2. Calculate efficiencies as a function of incident neutron energy,
3. Calculate efficiencies as a function of B_5C thickness, and
4. Determine efficiencies and reaction rates of other neutron interactions within B_5C and silicon that may be of interest despite the much smaller cross-sections.

Item one was used to determine TRIM input for development of the TCAD heavy ion models. Items two and three were part of the optimization study where charge collection efficiency results were coupled with capture efficiency to maximize overall detection efficiency within the B_5C diode. Item four was not directly related to any portion of the optimization study, but was companion information that was available and may prove useful in future research. The post-processor developed, see Appendix C.3, produces efficiency, average energy, and energy histograms of each possible neutron reaction product in BC and silicon [10].

Sample GEANT input files used for the simulation are included in Appendix B.1. Table 1 shows the different GEANT cases simulated along with the control parameters used in each case.

Table 1. Matrix of simulation cases showing parameter variations used. Diode area (0.024 cm^{-2}), silicon thickness (525 μm), and material composition ($B_5C:H_x$/Si with 100% ^{10}B) were unchanged in each simulation.

BC Thickness	Neutron Energy							
	0.025 eV	1 eV	10 eV	100 eV	1 keV	10 keV	100 keV	1 MeV
0.5 μm	X	X	X	X	X	X	X	X
1 μm	X	X	X	X	X	X	X	X
1.5 μm	X	X	X	X	X	X	X	X
2 μm	X	X	X	X	X	X	X	X
2.5 μm	X	X	X	X	X	X	X	X
3 μm	X	X	X	X	X	X	X	X
3.5 μm	X	X	X	X	X	X	X	X
4 μm	X	X	X	X	X	X	X	X
4.5 μm	X	X	X	X	X	X	X	X
5 μm	X	X	X	X	X	X	X	X

3.3 TRIM

TRIM was used to obtain track length and linear energy transfer [LET] information for the capture products using the average energy deposited by each ion as specified by GEANT [78]. For BC, the chemical formula $C_2B_{10}H_{12}$ was used with a density of 2.5 g cm^{-3}, and elemental silicon with a density of 2.32 g

cm^{-3} was used for the ions in the silicon substrate. The tracks were subdivided into 100 segments to allow for more accurate accounting of the LET along the track length. The variation of the LET along track length is demonstrated for an 800 keV alpha in Figure 35.

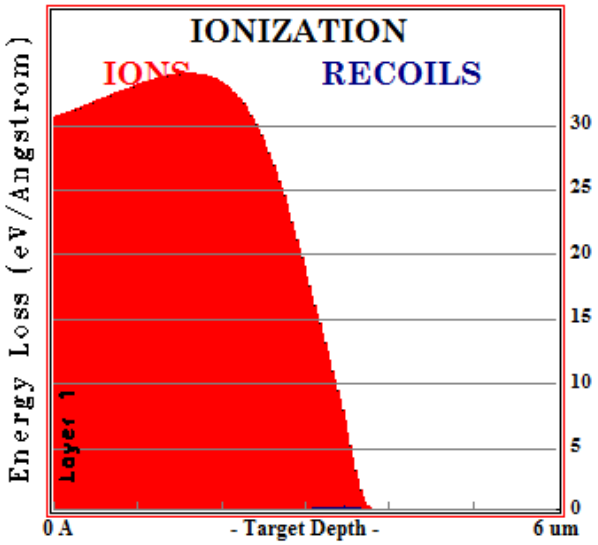

Figure 35. Energy loss profile (LET) as a function of depth into a target.

TRIM can also be used to provide information on radial energy range and straggling. This is a method of defining the spread of the ion tracks in a material. Unfortunately, since single tracks are required in TCAD, this information does little to provide the necessary track volume input required. As a simplification, each track is defined as being a cylinder, 5 nm in radius [79,80]. This is not a completely accurate picture as shown in Figure 36, where the track width varies over the length of the track (and would be different for the He and

Li ions) [81]. However, in the context of the current model limitations (little to no information on recombination and trapping within BC), it provides a sufficiently accurate method to model the heavy ion interactions. Furthermore, the simple cylindrical geometry simplifies meshing while minimizing nodes thus increasing computational efficiency as described in Section 3.4.1.

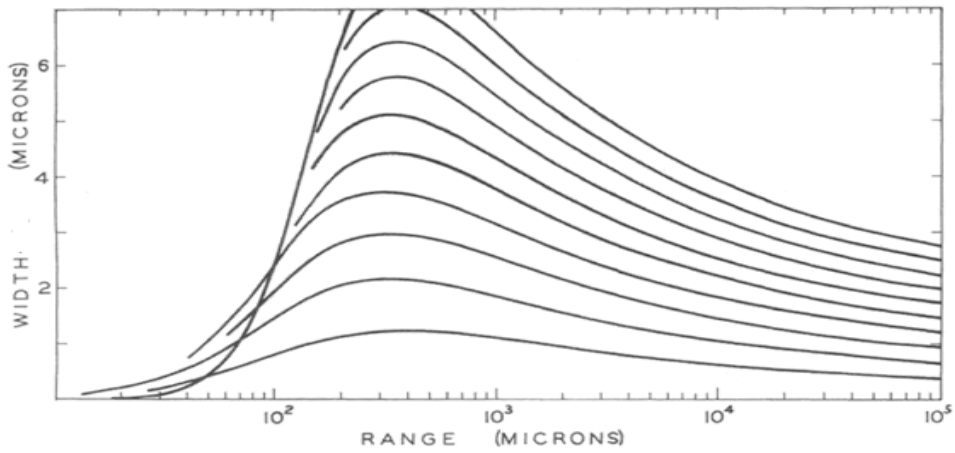

Figure 36. Ion track width (solely charged) as a function of range and Z of the incident ion in G-5 emulsion (ρ = 3.8 g cm^{-3}). Ranges of ions and material differ from those present in BC diodes, but results are illustrative ion track width and factors governing its distribution [81].

3.4 TCAD

While the preceding sections focused on the input to the TCAD heavy ion models, the following will focus primarily on the development of the diode itself and the accompanying electrical transport physics within TCAD. The final parameters used to define the physical models are discussed in Section 4.3.1 in Table 7.

3.4.1 Geometry and Gridding

To avoid the introduction of edge effects and allow for accurate modeling of the depletion width, a full scale model was developed in TCAD as depicted in Figure 37. The standard geometry, depicted in Figure 37, was based off the North Dakota State University (NDSU) #1 diode. It was a 2μm B_5C layer deposited on 525μm 8000 Ω-cm silicon with an 875μm radius silver contact on the BC side and a solid silver contact on the silicon side. The device is symmetric in the X- and Y-axis orientations and the depth of the layers is along the Z-axis.

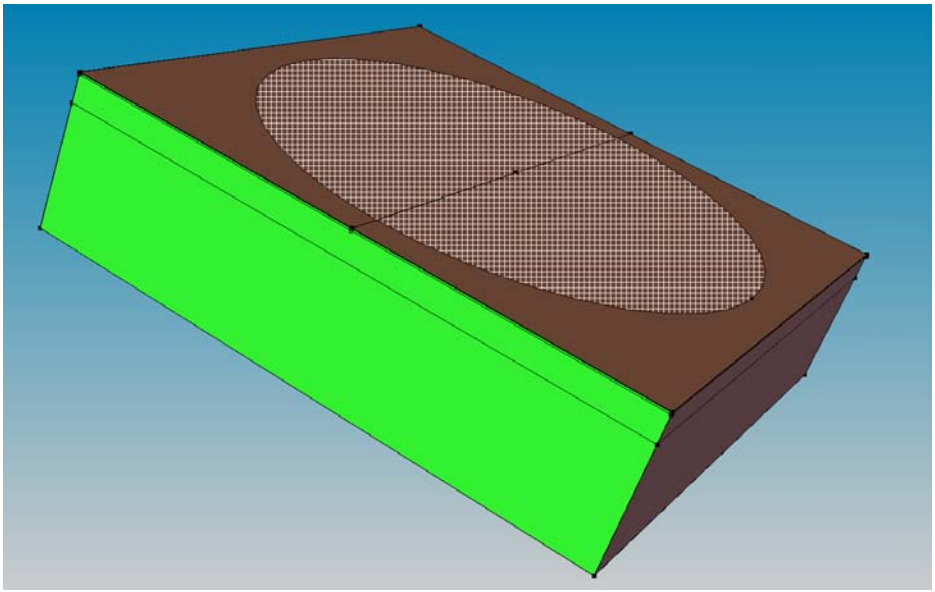

Figure 37. B_5C diode as modeled in TCAD. Top layer (brown) is B_5C (2 μm), green portion is silicon (525 μm), cross-hatched circle represents B_5C contact, and a solid contact is along back face (not shown). Black lines represent gridding regions. Diode area is 2000 x 2000 μm, and it is 527 μm thick.

However, this full scale model approach requires some sacrifice in gridding because of limited memory on the available stand-alone Linux boxes (8 GB) and the AFIT cluster (4GB). Increased meshing requires accessing the swap memory (16 GB for both) which drastically increases computational time thereby limiting the number of optimization scenarios that can be simulated in a fixed period. To preserve fidelity, the same meshing scheme was used in each model with only the B_5C and silicon Z extents being variable in the optimization simulations where BC thickness was studied. Figure 38 shows the gridding used in the diode. Table 2 lists the specific grid sizes used in each defined region. In general, gridding is fine at the interfaces and progressively coarser with increasing distance from the interface, finer in Z than in X and Y (which are symmetric), and finest of all in the ion box to allow resolution on the nm scale. This method allows for the finer precision in regions where the electric field, depletion width, and pair generation change the most while working within memory allocation restrictions. However, the coarse gridding can introduce artifacts in the data (i.e. in diodes which have depletion widths in the Si Bulk 1 or 2 as defined by Table 2).

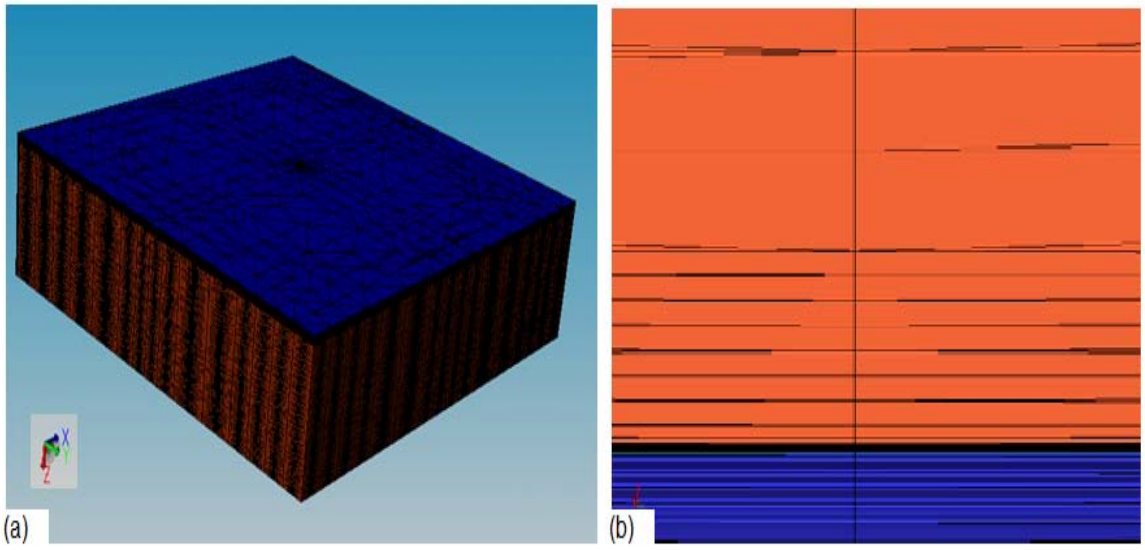

Figure 38. (a) Diode grid with same dimensions as Figure 37. (b) Zoomed in view of depletion region gridding. For scale reference, the BC region depicted (blue shading) is 2 μm thick.

Table 2. Grid meshing parameters for each defined region. Distances specified are for 2μm B_5C on 525μm Si.

Region	X		Y		Z	
	Min	Max	Min	Max	Min	Max
BC Ion Box	0.05	0.1	0.005	0.01	0.005	0.01
Si Ion Box	0.005	0.01	0.005	0.01	0.05	0.1
BC (0μm – 1.9μm)	100	225	100	225	0.05	0.1
Interface (1.9μm – 2.1μm)	100	225	100	225	0.025	0.05
Si Interface (2.1μm – 5.5μm)	125	225	125	225	0.2	1
Si Bulk 1 (5.5μm –25μm)	125	250	125	250	1.5	3
Si Bulk 2 (25μm – 525μm)	150	250	150	250	4	15

The "ion box" represents the final simplification that was made based on gridding resolution maximization. It is in this "ion box" that the boron capture

products are confined. This allows for maximum resolution in as small of a region as possible to fully capture the ion tracks while minimizing total device nodes that must be simulated. Additionally the boron capture products, ^{4}He and ^{6}Li, are emitted back to back and isotropic with ranges on the order of 1-4 microns. However, many simulations used BC layers less than the resulting particle range in the material. In order to achieve full energy deposition of the capture products, one option would be to have the "ion box" placed at an acute angle with respect to the junction as to allow correct modeling of this back to back emission. This would dramatically increase the number of mesh nodes thereby reducing the resolution that could be obtained elsewhere. An alternative solution was developed as depicted in Figure 41 from Chapter 4 to simulate a full energy deposition event. In silicon, the particle was given a trajectory perpendicular to the BC-Si junction. In the BC region, the particles were given paths parallel to the junction so as to ensure full deposition within the region. While the orientation of the tracks with respect to the junction will affect the charge collection through differing initial recombination rates, this is presented as an idealized case that is computationally manageable.

3.4.2 Baseline Model Development

Limited benchmark data existed at the time of model development. Diodes obtained subsequently, see Section 5.1, were qualitatively (NDSU#2 -

#4) or quantitatively (UMKC#1) different from the devices used as benchmarks. Immature growth procedures resulted in variations between diodes grown at different locations or times requiring future model adjustment to match the final diode characteristics.

In this research, two diodes were used as benchmarks. UNL#1 was used in a paper published by Hong et al. to obtain electrical characterization data [21]. NDSU#1 was obtained from NDSU via UMKC for irradiation experiments in August 2010. Neither provided the full information needed for benchmark purposes. From UNL#1, capacitance vs. voltage (C-V) characteristics, rise time (BC and Si), and current at a single bias point (-19 V) were obtained experimentally. From NDSU#1, well-defined current vs. voltage (I-V) characteristics from 0 to -5 V were also obtained experimentally in this research.

The methodology used to develop a model that replicates the benchmark devices' characteristics is rather simple in comparison to other methods available in the literature [82]. Due to the variations in each device along with the wide range of parameters as illustrated in Table 3, precision gained by such an approach would largely be artificial and hyperbole in the case of the B_5C diodes.

Table 3. Summarized range of parameters for crystalline BC (Werheit model) and a-B_5C (UNL/Dowben model).

Parameter	Boron Carbide (Werheit Model)	Amorphous Boron Carbide (UNL/Dowben Model)
E_g [eV]	~2.09 [43]	~0.9[35]
$\mu_{untrapped}$ [$cm^2\ V^{-1}\ s^{-1}$]	~565 [16]	100-300 [46]
$\mu_{efective}$ [$cm^2\ V^{-1}\ s^{-1}$]	~1 [16]	10^{-2} – 10^{-4} [21]
ρ [Ω-cm]	Unspecified	10^6 - 10^{12} [83]
N_c/N_v [cm-3]	10^{18} - 10^{20}[16]	10^{18} - 10^{20}[46]
N_A [cm^{-3}]	Unspecified	~4.5 x 10^{12} [21]
∈	Unspecified	~8 [15]
m_p	1-10[16]	~1 [46]
N_T [cm-3]	~10^{21}	Unspecified
τ [sec]	Unknown	Unknown
χ [eV]	Unknown	Unknown
Recombination Rates	Unknown	Unknown
Trapping x-section [cm^2]	Unknown	Unknown

First, basic models were developed as a starting point to determine how best to model the device within TCAD. Owing to the large uncertainties in the band gap and traps, the following four models, based off the Dowben and Werheit models, were tested:

1. 2.09 eV E_g with traps
2. 2.09 eV E_g without traps
3. 0.9 eV E_g with traps
4. 0.9 eV E_g without traps

Each of these models had starting parameters of $\mu = 1$ (electron and hole), $N_c/N_v = 10^{19}$, $\varepsilon = 8$, $\chi = 4.3$, $N_A = 4.5$ x 10^{12}, $N_T = 10^{21}$ (for #1 and #3), and all other parameters were TCAD defaults. From this point, the sensitivity of each parameter was determined in a similar manner to that described in Section 3.4.3. Due to the extremely low currents (10s of fA), it became obvious that the 2.09 eV E_g models were inadequate matches to the benchmarks.

Model variations that investigated the interaction dynamics of the traps with relation to the leakage current and depletion width led to the conclusion that a combination of factors would preclude including traps within the model. First, the options available for specifying trap type (electron or hole traps) did not adequately capture the occupation dynamics of the split-off gap states formed in the electron deficient BC. Second, an almost infinite range of possibilities existed regarding the possible combinations of trap location, density, type, capture cross-section, and emission cross-section with little to no information in the literature on which to base choices. Finally, inclusion of the traps, most likely due to the incorrect occupation dynamics (i.e. the split off states are positively charged when empty vs. the TCAD traps which are neutral when empty) nearly always led to type inversion in the diode. This resulted in positive space charge creation in the p-type region under reverse bias and vice

versa. The culmination of these factors led to the removal of preliminary model # 3 as an option.

This left model #4 as the most viable. However, once traps were removed, the starting baseline parameters had to be established as *effective* parameters to account for the lack of trapping and emission dynamics within the diode. Electron affinity and band gap were set as described in Appendix A.1. Mobility was defined so as to agree with rise times from literature as described in (7). The remaining parameters were left as the best available values from literature as described above. Finally, the recombination rate was adjusted in each material to account for the absence of traps. This factor, in many senses, is an externally applied factor that covers for gaps in the BC property knowledge base. However, the trap densities and recombination currents in different diodes can vary significantly making this a good-fitting parameter to use after fully specifying the other parameters to the extent they are known.

3.4.3 Sensitivity Procedures

Sensitivity studies provide several useful pieces of information regarding the model and diode. Some of the benefits of sensitivity studies are:

1. Guiding baseline model development as discussed in Section 3.4.2,
2. Determining areas where the model diverges more rapidly (i.e. biases and/or ranges of parameters),

3. **Guiding future research by determining relative importance of physical parameters,**

4. **Verifying model consistency (i.e. current rises with lower E_g etc.), and**

5. **Providing an indication of the manner in which the current will shift based on physical parameter updates so that revised optimization results can be inferred without full re-simulation.**

For this research, the sensitivity was defined as

$$\frac{\Delta I(V)}{I(V)} = S\frac{\Delta x}{x}, \tag{10}$$

where $I(V)$ is the current as a function of bias (A), x is the parameter of interest, and S is the sensitivity [84]. In (10), a sensitivity value of one indicates direct proportionality.

In this method, each parameter is investigated over a specified range, which is tied to the ranges of possible values shown in Table 3, while the other parameters are held constant. Table 4 illustrates the parameters and ranges utilized in this sensitivity study. The one exception to the one-parameter variation rule is when χ and E_g were varied simultaneously (consistent with the calculations shown in Appendix A.1) to maintain a consistent heterostructure flat band diagram.

Table 4. Parameters and ranges used for sensitivity studies.

Parameter	Range
X [eV]	3.4-4.8
E_g [eV]	0.8 – 1.0
X & E_g [eV]	0.8 – 1.0 (in terms of E_g)
$r_{contact}$ [μm]	750 – 900
μ (e) [$cm^2 V^{-1} s^{-1}$]	10^{-4} – 100
μ (h) [$cm^2 V^{-1} s^{-1}$]	10^{-4} – 100
μ (both) [$cm^2 V^{-1} s^{-1}$]	10^{-4} – 100
N_c [cm^{-3}]	10^{18} – 7.5 x 10^{21}
N_v [cm^{-3}]	10^{18} – 7.5 x 10^{21}
N_c/N_v	0.1 – 10
ρ_{Si} [Ω-cm]	1 – 20k
N_A [cm^{-3}]	10^{11} – 10^{14}

3.4.4 Optimization Procedures

For optimization, two metrics were defined to assess the relative performance of each configuration against its peers. First, S/N was defined as the ratio between the peak current pulse produced from the heavy ion interaction to the steady state reverse saturation current. The second metric used, Q, or charge collected, was found from the difference between the integration of the area under the current pulse resulting from the heavy ion interaction (from 0 to 100 μs) and the area under the saturation current (also

from 0 to 100 μs). Both of these calculations were accomplished using post-processors whose input files are shown in Appendix C.2.

The use and origin of each of these metrics can provide vastly differing results. As mentioned in Chapter II, the result of a heavy ion interaction in a diode is e-h which are subsequently separated and collected at the contacts. This produces a current pulse whose magnitude is directly proportional to the pulse width (driven by the mobility of the material). Some detector circuits can function by directly reading this resulting current pulse [12]. However, BC has a very low mobility, for both electrons and holes, resulting in a very long pulse (10s of μs) whose magnitude is extremely low. For cases such as these, and most detectors in general, an integrating preamplifier is placed in the detection circuitry to take the pulse width out of the equation and amplify what is otherwise a very small signal. In the case where an integrating preamplifier is used, the total charge collected is indicative of the performance of that detection circuit. It is for this reason that the Q optimization results will likely be found to be more predictive than the S/N results.

The Q and S/N results have little quantitative value due to the assumptions made on the trapping and recombination dynamics necessitated by a lack of research data mentioned in previous sections. However, any change in the models regarding traps and/or recombination rates brought about by new

research will affect each optimization scenario uniformly. In this way, the Q and S/N optimization results still have intrinsic qualitative value. For this reason, the Q and S/N magnitudes were normalized to the maximum magnitude for a given optimization parameter. This still preserves the parameter optimization information while limiting the presentation of what is likely misleading quantitative values.

Using the methods outlined, the optimization cases shown in Table 5 were evaluated. Similar to the sensitivity studies, only the indicated parameter was varied while the others served as controls. Contrary to the sensitivity studies, the results were dependent on the resulting transport of the heavy ion induced charge and the resulting current pulse instead of the reverse bias I-V characteristics. Since collection can be experimentally measured at either contact (not simultaneously due to the drastically different collection times), Q and S/N were defined for the transport of electrons (holes) to the silicon (BC) contact. Finally, each of these parameters, over the full range, was simulated at the following values of reverse bias to quantify the change of Q and S/N at different operating bias conditions: 0.25V, 1V, 2.5V, 5V, 7.5V, 10V.

Table 5. Parameters and ranges considered in optimization study. The effect of each for collection at either contact was also evaluated.

Parameter	Range
BC Thickness [μm]	0.5 – 5
Si Thickness [μm]	250 – 525
ρ_{Si} [Ω-cm]	1 – 20k
ρ_{BC} [Ω-cm]	8.3×10^{7} – 8.3×10^{10}
Operating Reverse Bias [V]	0.25 – 10V

IV. Modeling Results and Analysis

4.1 GEANT Efficiency and Interaction Dynamics

Although the primary purpose of the GEANT simulations was to produce efficiency and ion transport data from the boron capture reaction, a wealth of information regarding reactions of secondary importance, such as recoils and those listed in Figure 39, is readily available. For example, at 1 MeV and higher neutron energies, recoil and threshold capture events can generate hundreds of keV to MeV particles at rates greater than 1 per 100 incident neutrons. These events would constitute background and extra useful signal that may be significant in some applications.

Isotope	Reaction	Norm. (%) (1 eV)	Norm. (%) (1 MeV)	Norm. (%) (10 MeV)	Abs. (%) (1 eV)	Abs. (%) (1 MeV)	Abs. (%) (10 MeV)	Nat. Iso. Abd. (%)	Q-value (MeV)
Boron	${}^{1}_{0}n + {}^{10}_{5}B \rightarrow {}^{7}_{3}Li^{*}(1.472\,MeV) + \alpha(0.840\,MeV)$	99.9	99.6	37.1	42.3	8.8	3.4	19.9	2.312
	${}^{7}_{3}Li(1.776\,MeV) + \alpha(1.013\,MeV)$								2.790
	${}^{9}_{4}Be + {}^{2}_{1}H$	—	—	27.8	—	—	2.6		−4.361
	${}^{10}_{4}Be + {}^{1}_{1}H$	2.2×10^{-7}	0.4	35.1	9.5×10^{-8}	3.8×10^{-4}	3.2		0.226
Silicon	${}^{1}_{0}n + {}^{28}_{14}Si \rightarrow {}^{25}_{12}Mg + \alpha$		37.2 (12 MeV)			10.1 (12 MeV)		92.2297	−2.654
	${}^{28}_{13}Al + {}^{1}_{1}H$		60.7 (12 MeV)			16.5 (12 MeV)			−3.840
	${}^{1}_{0}n + {}^{29}_{14}Si \rightarrow {}^{26}_{12}Mg + \alpha$		57.9 (12 MeV)			13.4 (12 MeV)		4.6832	−0.034
	${}^{29}_{13}Al + {}^{1}_{1}H$		42.1 (12 MeV)			9.7 (12 MeV)			−2.897
	${}^{1}_{0}n + {}^{30}_{14}Si \rightarrow {}^{27}_{12}Mg + \alpha$		67.7 (12 MeV)			2.8 (12 MeV)		3.088 72	−4.200
	${}^{30}_{13}Al + {}^{1}_{1}H$		32.3 (12 MeV)			2.1 (12 MeV)			−7.778

Figure 39. Isotope specific reactions from BC detector materials[10].

Fundamental nuclear physics allows the theoretical capture efficiency to be calculated from

$$f_{captured} = 1 - \exp[-\sigma n x], \tag{11}$$

where $f_{captured}$ is the fraction of incident neutrons which are captured, σ is the microscopic capture cross section [cm^2], n is the atom density of the neutron sensitive material, and x is the neutron sensitive material's thickness [cm]. The resulting ^{10}B capture efficiencies (assuming 100% ^{10}B and a 25 meV beam of neutrons) from (11) and GEANT are shown in Figure 40. Since the slope is given by the cross section, a fit of the GEANT data results is of the form

$$\varepsilon = 3.47 t_{BC} \tag{12}$$

where ε is the capture efficiency and t_{BC} is the boron carbide thickness [μm].

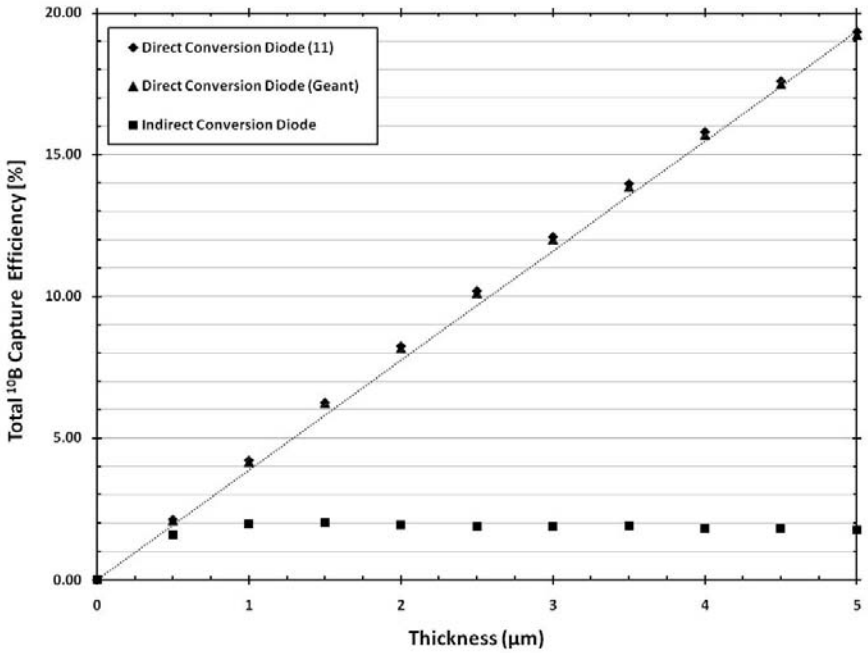

Figure 40. Total capture efficiencies in BC calculated by various means. The dotted line represents the fit of the data presented in (12). The Si ion efficiency indicated is the efficiency at which boron capture products enter the silicon substrate (i.e. indirect conversion device).

The results in Figure 40 are broken into direct and indirect conversion diode results. The indirect conversion efficiency was calculated from the efficiency that boron capture products enter the silicon substrate following a capture event. This is representative of the efficiency cap when collecting from the silicon contact where the device is essentially serving as an indirect conversion device. In this case, the efficiency is limited to ~2% at 1.5μm and decreases slightly with increasing BC thickness. This somewhat counterintuitive result is best understood in terms of the very short range of the 0.84 MeV Li ion

(1.4μm) and the reduction in capture for differential volume elements closer to the interface (due to source depletion) as the thickness is increased.

4.2 Final Ion Model

Since TCAD simulates single ions and does not model the full deposition process, a "typical" energy-deposition scenario was used as described in Chapter 3. The resulting model had the ^{6}Li ion fully deposited in BC, and the ^{4}He ion partially deposited in both layers based on the average energy deposition obtained from GEANT. Table 6 is a summary of the final parameters used for the ion deposition models in TCAD. In each case, the TRIM and GEANT generated input into TCAD conserved e-h to within 1% of that calculated from the use of the e-h generation energy obtained from Figure 19 and Knoll [12,55]. The full input, to include the LET and track subdivisions, is included in Appendix B.2.

Table 6. Final ion model parameters. Wt is the characteristic Gaussian radius of the track, S_hi is the characteristic Gaussian temporal distribution of the charge, l is the track length, and GLet is the linear energy transfer function.

Parameter	^{4}He in Silicon	^{4}He in BC	^{6}Li in BC
Energy Deposited (MeV)	0.8	0.69	0.79
e-h	2.6×10^{5}	2.2×10^{5}	2.6×10^{5}
W_t [cm]	5×10^{-4}	5×10^{-4}	5×10^{-4}
S_hi (t_{plasma}) [s]	1×10^{-9}	1×10^{-9}	1×10^{-9}
l [cm]	2.86×10^{-4}	1.26×10^{-4}	2.15×10^{-4}
G_{Let} [prs cm^{-3}]	Variable	Variable	Variable

After alteration of the track directions consistent with the description in Section 3.4.1, the TCAD generated e-h pair density is shown in Figure 41. In the scenario depicted in Figure 41 (model of NDSU#1), Z represents distance into the BC diode with zero being located at the start of the BC layer and 527 μm being the ending location for the silicon (2 μm BC and 525 μm Si). UNL#1 extends from 0 – 2000μm in both the X and Y directions. The non-uniformities noted in Figure 41 are due to meshing limitations as described in Section 3.4.1.

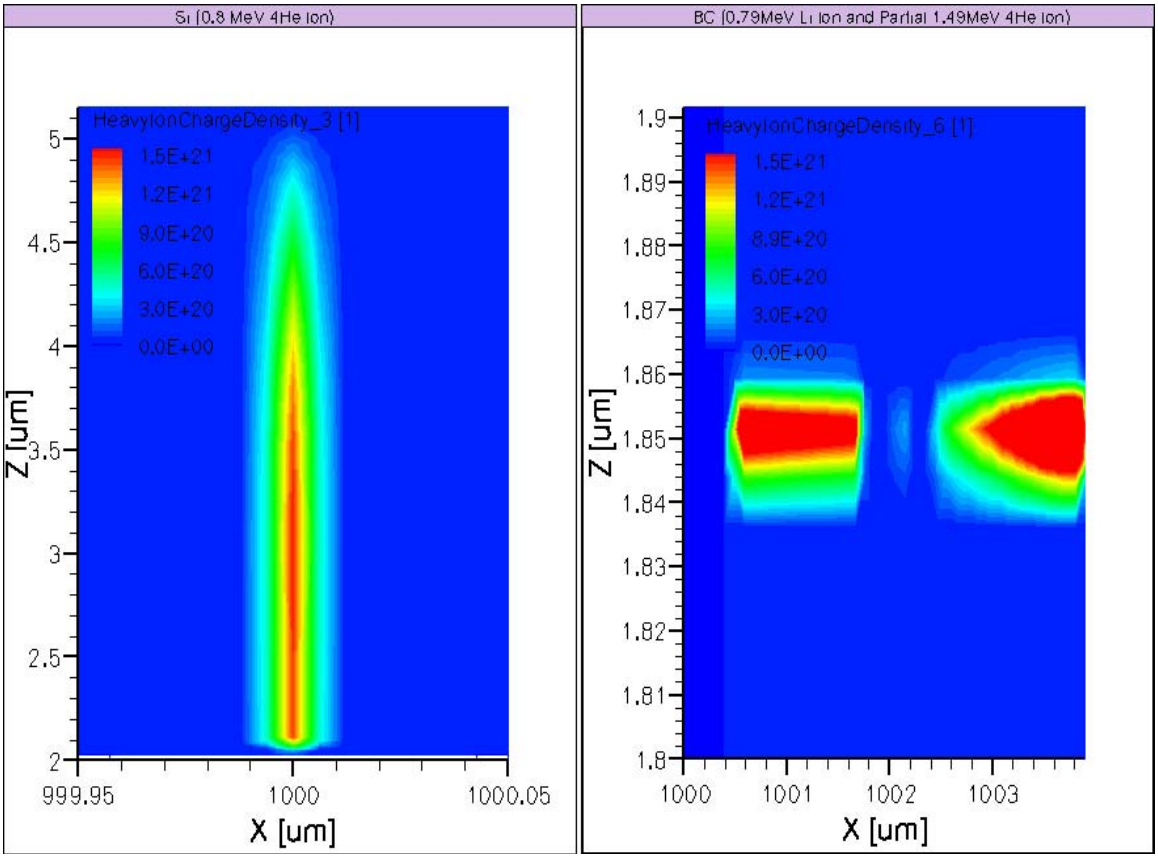

Figure 41. Representative heavy ion tracks in TCAD. The units for the scale are e-h cm^{-3}.

TCAD allows plotting of various parameters of interest as a function of time to allow for tracking of the diode response and e-h transport following the insertion of heavy ions. While not useful in directly answering the optimization goals of the research, it is informative to demonstrate that the ion models behave in accordance with expected physics and transport times outlined in Appendix A.2. Without understanding the timing origins of the resulting transient response, a full explanation for the optimization results is not possible and/or may be inaccurate.

A representative transient current response in BC is shown in Figure 42. Of immediate note is the characteristic double peak feature in the resulting hole current. This is attributable to the large local field generated due to the low mobility within BC. This large electric field temporarily accelerates a portion of the generated holes to the BC contact much faster than otherwise possible due to the steady state electric field. However, not all of the holes benefit from this effect due to generation in the silicon substrate and self shielding within the e-h pr cloud (plasma time). Figure 42 and Figure 43 show this effect graphically through the displacement current (time-varying electric field).

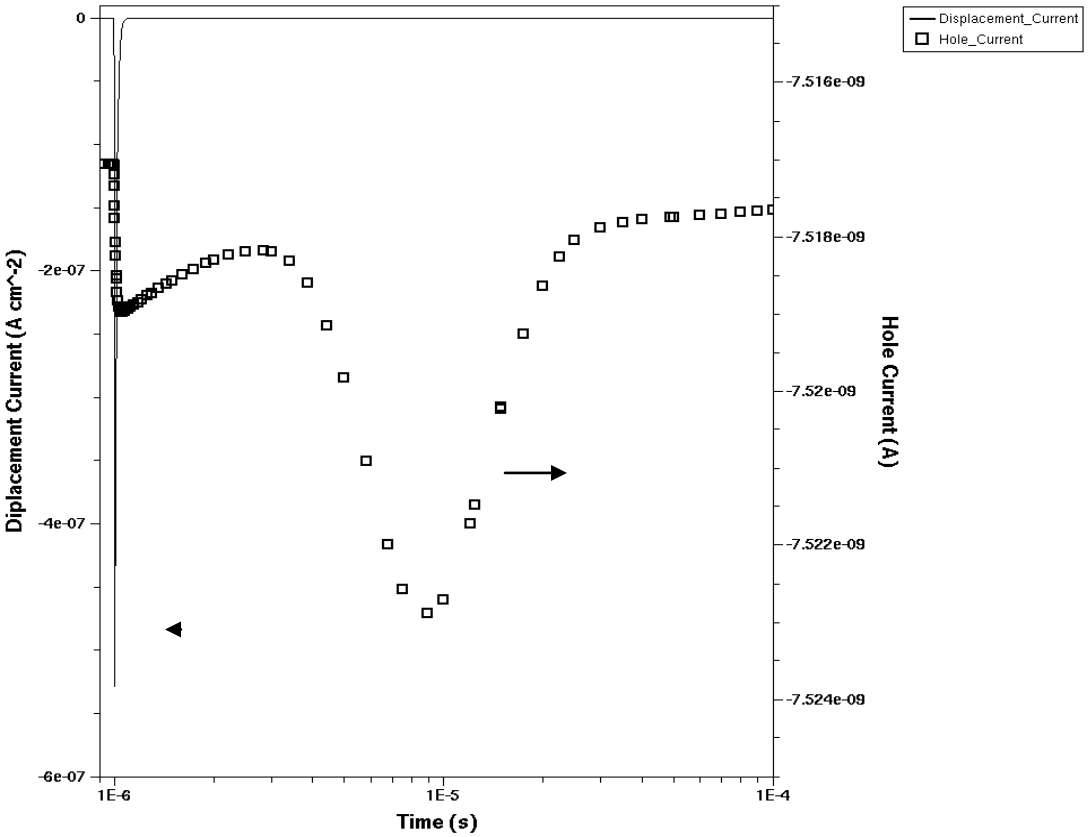

Figure 42. Displacement and hole current in BC resulting from heavy ion deposition.

In Figure 43 through Figure 45, the electric field, hole current density, and electron current density are shown as a function of time. The time for each figure is located at the top of each sub-frame. In all three, the legend is given by red indicating the maximum value and blue indicating the minimum. The interface occurs at 1 μm (UNL#1). The white lines in the Si region (above 1 μm) and BC region (below 1 μm) indicate the TCAD calculated depletion width. For referencing, the frames are numbered along the rows from left to right and top to bottom (i.e. the bottom left is frame 4). In Figure 43, the electric field

can be seen to rapidly increase (for the above stated reasons) from the steady state value shown in frame 1 throughout the BC region in frames 2-4 (ns time scale). In frame 5 (μs time scale), the electric field in BC is highly distorted with low (green) and high regions visible due to the movement and separation of charge. Finally, in frame 6, the electric field starts returning to steady state as the remaining holes reach the BC contact.

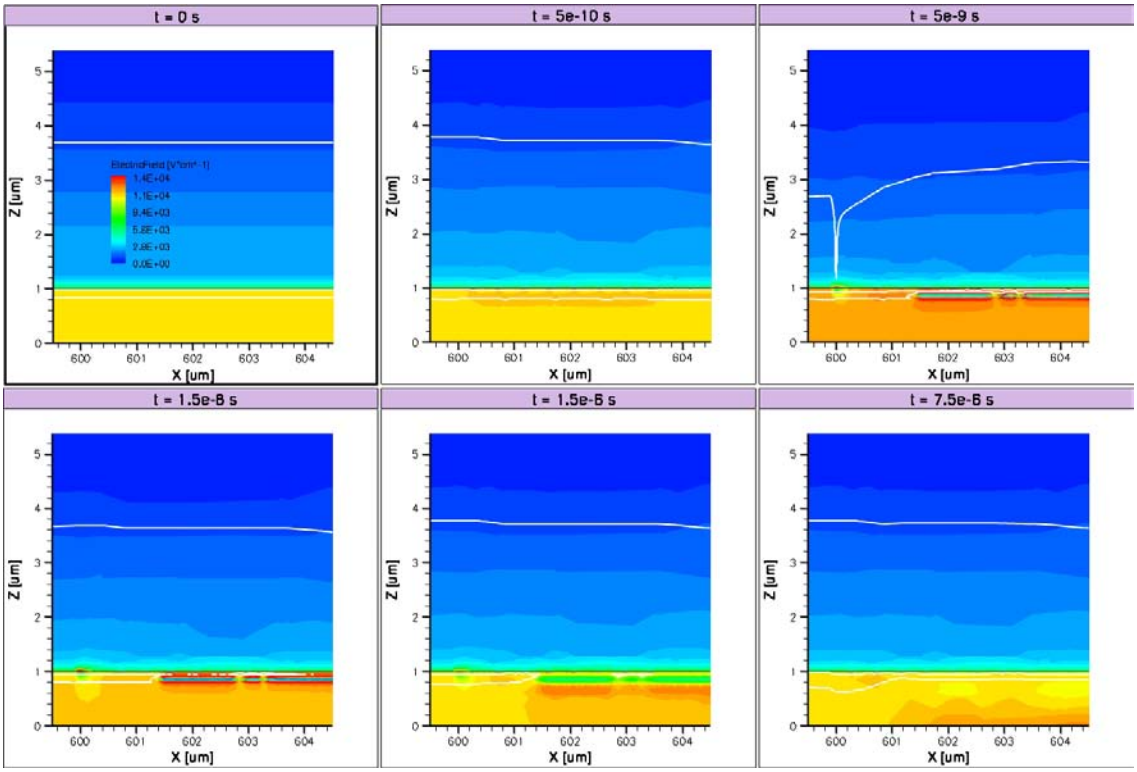

Figure 43. Electric field variation as a function of time in UNL#1 following heavy ion deposition.

The hole (electron) current density is depicted in Figure 44 (Figure 45). The generation of a high density of e-h is shown in frames 2-3. By frame 4, the

e-h have separated in the silicon region while they are still tightly packed in the BC region due to the large difference in mobility in the two regions. By frame 5, the initial e-h in silicon have largely dissipated and the BC electrons have started to transit the interface into silicon. In frame 6, the holes are beginning to reach the BC contact and the electrons have all been transported to the Si contact. The diode has not yet returned to steady state values due to the continued electric field variations shown in Figure 43 from the continued transport of holes in BC.

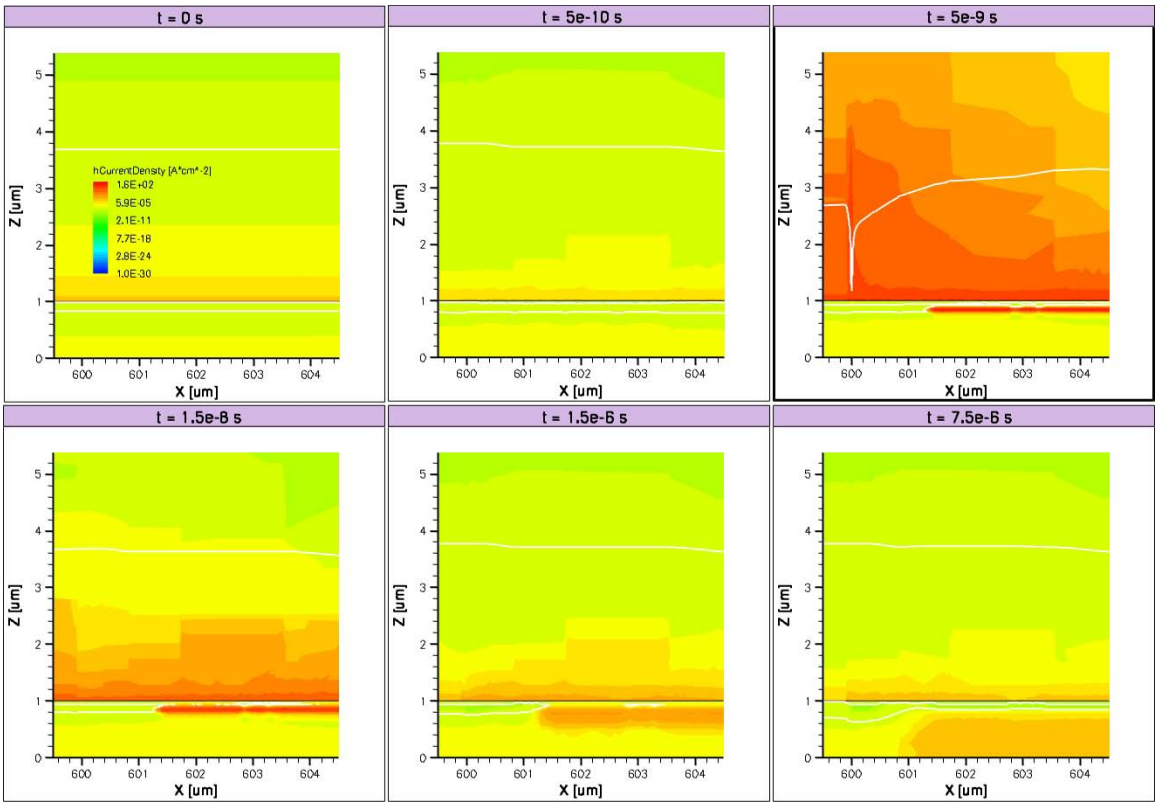

Figure 44. Hole current density as a function of time in UNL#1 following heavy ion insertion.

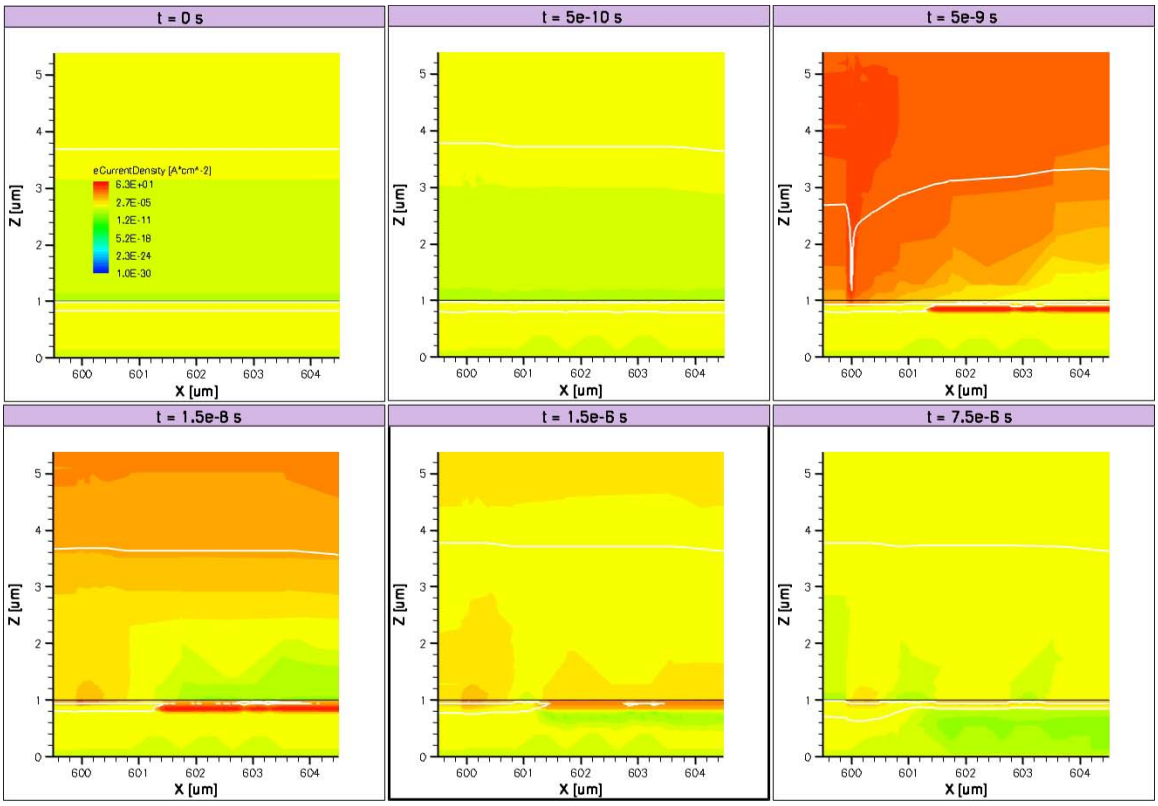

Figure 45. Electron current density variation as a function of time in UNL#1 following heavy ion insertion.

4.3 TCAD Results

4.3.1 Final Model Parameters

The final model parameters for the UNL#1 and NDSU#1 models are shown in Table 7. The one significant difference noted between UNL#1 and NDSU#1 is the band gap. The band gaps of different processes vary slightly due to changes in trap densities or slight deviations from the ideal 5:1 B/C ratio of ortho-carborane as shown in Figure 14. The NDSU parameters were used as the baseline in the optimization and sensitivity studies.

Table 7. Final BC parameters utilized in TCAD model.

Parameter	UNL#1	NDSU#1
X [eV]	4.58 [calc]	4.58 [calc]
E_g [eV]	0.9 [35]	0.95 [35]
$r_{contact}$ [μm]	500 [21]	875 [25]
μ (e) [$cm^2 V^{-1} s^{-1}$]	0.001 [21]	0.001 [21]
μ (h) [$cm^2 V^{-1} s^{-1}$]	0.00075 [21]	0.00075 [21]
N_c [cm^{-3}]	10^{19} [16,46]	10^{19} [16,46]
N_v [cm^{-3}]	10^{19} [16,46]	10^{19} [16,46]
N_c/N_v	1	1
Ni [cm-3]	2.85 x 10^{11} [calc]	1.08 x 10^{11} [calc]
ρ_{Si} [Ω-cm]	1.85 x 10^9	1.85 x 10^9
N_A [cm^{-3}]	4.5 x 10^{12} [21]	4.5 x 10^{12} [21]
Eionization	0.065 [16]	0.065 [16]
ε	8 [15]	8 [15]
E_F [eV wrt midband]	-0.071 [calc]	-0.096 [calc]

4.3.2 Comparison to Benchmarks

The above models were validated through comparison to known benchmarks as outlined in Section 3.4.2. UNL#1 was taken as the starting model because it had both current (albeit at only one point) and capacitance measurements from which to benchmark. Figure 46 shows the comparison between the modeled and measured capacitance density. The model agrees to within ~20% or better over the 0 to -10V range.

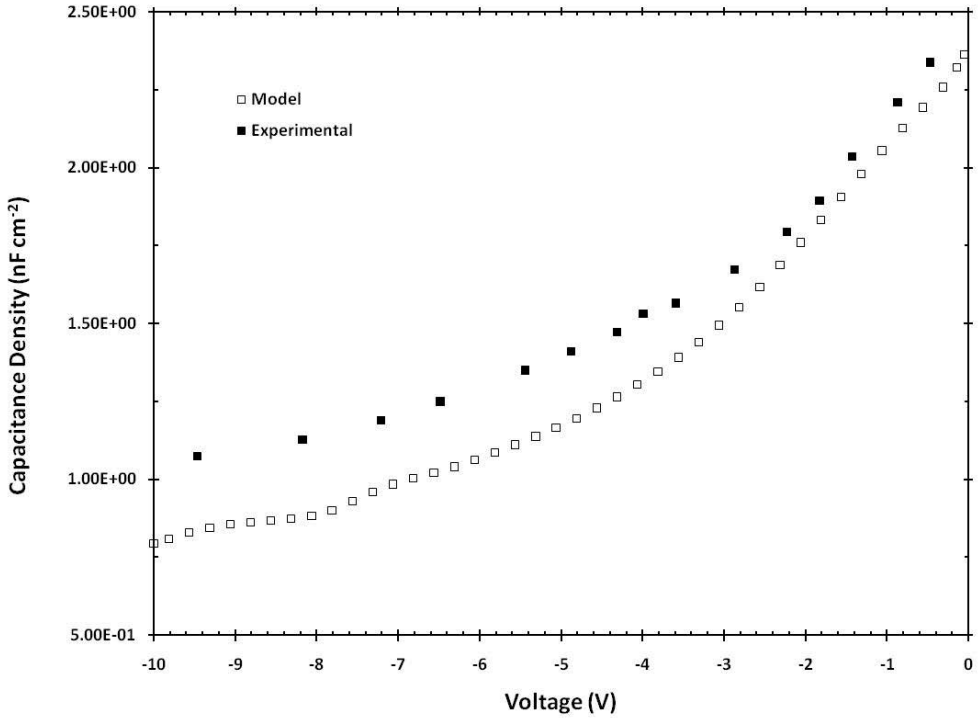

Figure 46. Comparison of experiment and model capacitance densities for UNL#1 [21].

There are several reasons for the inexact match between the two. First, the model parameters do not fully encapsulate the actually transport physics and instead are *effective* parameters designed to simulate key parameters as close as possible. Gaps in the knowledge of key BC parameters and the absence of key transport mechanisms in TCAD (specifically trap occupation dynamics) necessitated this usage of effective parameters. Second, the TCAD methodology of defining the space charge region introduces a level of variation between the model and experiment. From experiment, BC is fully depleted even at zero bias on the basis of space charge existence throughout the region [21,35,46]. As

shown in Figure 47, TCAD does not always calculate this based on the quasi-fermi level (UNL#1), but the space charge does indicate full depletion. However, despite these inconsistencies, the two methods of calculating depletion width from the TCAD results (capacitance assuming full BC depletion and the quasi-fermi level) tend to bracket the experimentally determined value (calculated assuming full BC depletion) as shown in Table 8. Assuming full BC depletion, the depletion width can be calculated from the capacitance density by

$$x_n = \varepsilon_{s,n}\left(\frac{1}{C_j} - \frac{x_p}{\varepsilon_{s,p}}\right), \tag{13}$$

where C_j is the capacitance density [F cm^{-2}], x is the depletion region [cm], and ε is the dielectric constant[49]. The final limitation, discussed in Section 3.4.1, is the increasing coarseness of the gridding with increasing distance from the interface. As the depletion width increases, it enters into coarser regions thereby limiting the precision achievable at high biases.

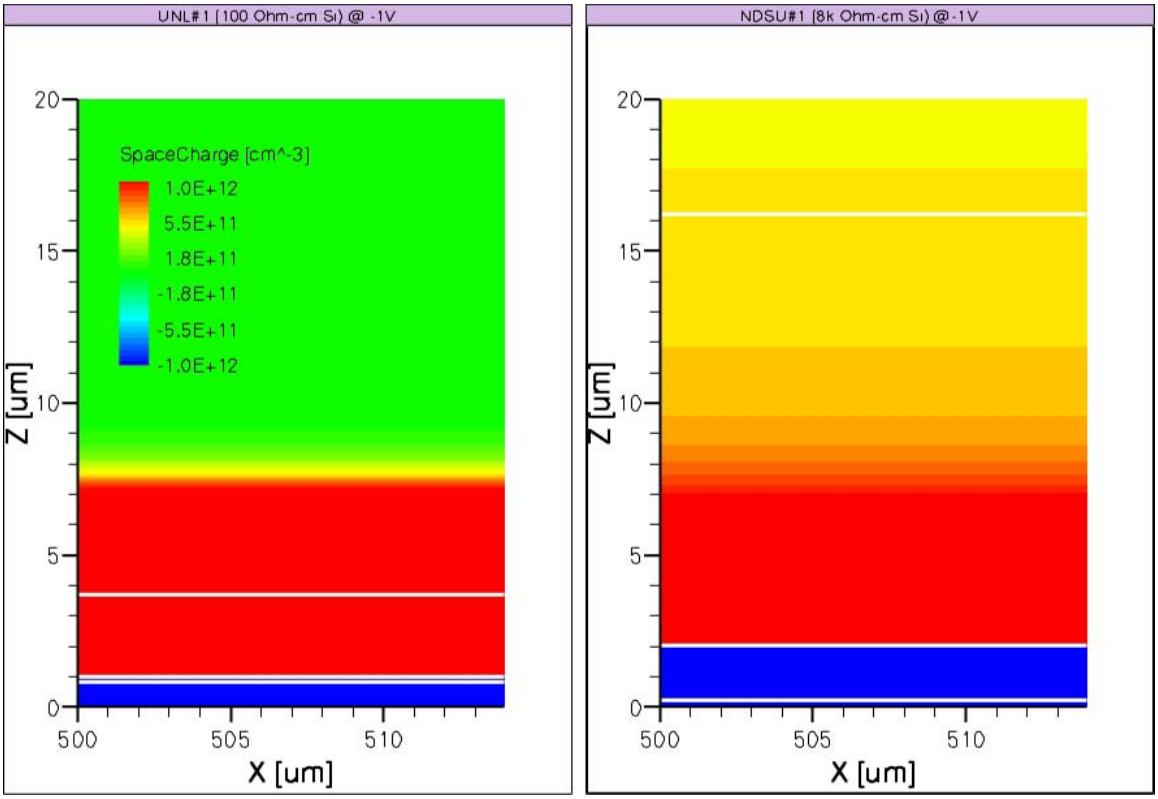

Figure 47. Comparison of UNL#1 and NDSU#1 depletion widths calculated on the basis of the quasi-fermi level[29].

Table 8. Comparison of experimentally determined depletion width to that calculated in the TCAD models. *Assuming full BC depletion

	Depletion Width @ -1V Bias (µm)
Experiment*	**3.3**
Model (Quasi-Fermi / Capacitance*)	**2.8 / 3.6**

The resulting I-V curve generated for the model parameters listed in Table 7 for UNL#1 is shown in Figure 48. As indicated, the bias agrees to within 7% at the only bias point available for comparison (-19V) [21]. Although

closer values could be obtained, by adjusting the 2nd or 3rd decimal place of the parameters, this additional precision is not warranted for the reasons outlined in Chapter 3.

The models were then modified to simulate the NDSU#1 diode. As shown in the NDSU#1 curve in Figure 48 and Figure 49, a direct conversion of model parameters did not yield I-V model results comparable to experiment. However, adjustment of the band gap replicated experimental results reasonably well as indicated in Figure 48 and Figure 49. Over the range where experimental data is available (0 : -5V), the model matches to within 10%.

Once the UMKC process is mature, obtaining several diodes from which to develop full benchmarks will allow a more complete model to be developed. This model would be much more quantitatively representative of the diodes that are utilized by the AMN group. However, the current model, while having some artifacts, is useful in qualitative determination of optimization parameters necessary for future generation diodes.

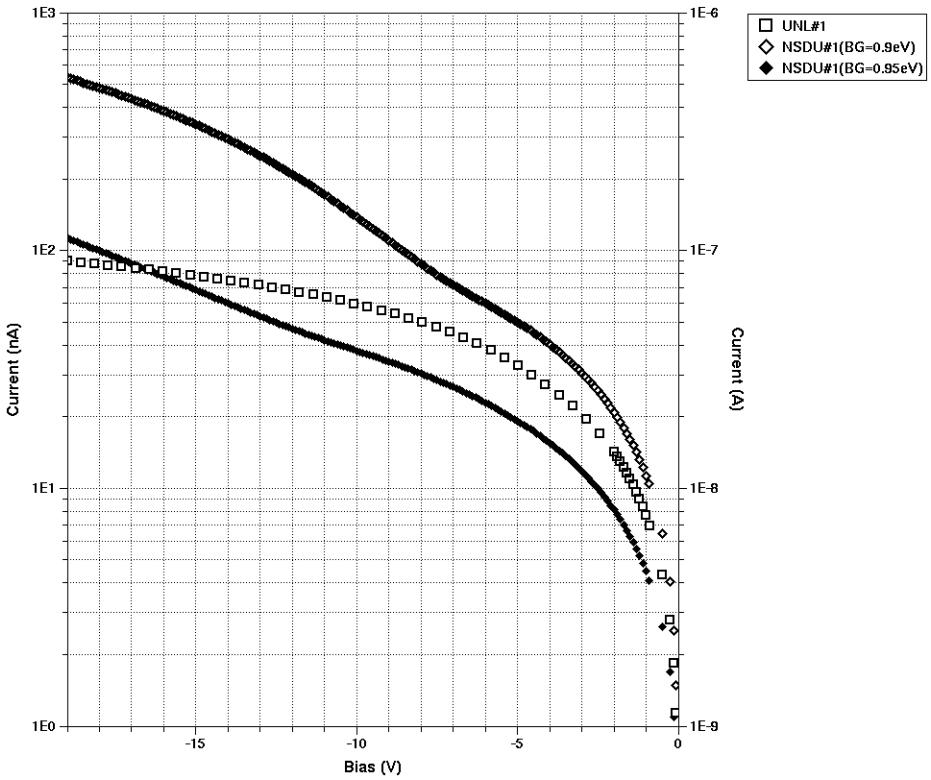

Figure 48. Comparison of TCAD I-V curves for UNL#1 and NDSU#1. The final model utilized NDSU#1 with a 0.95eV band gap.

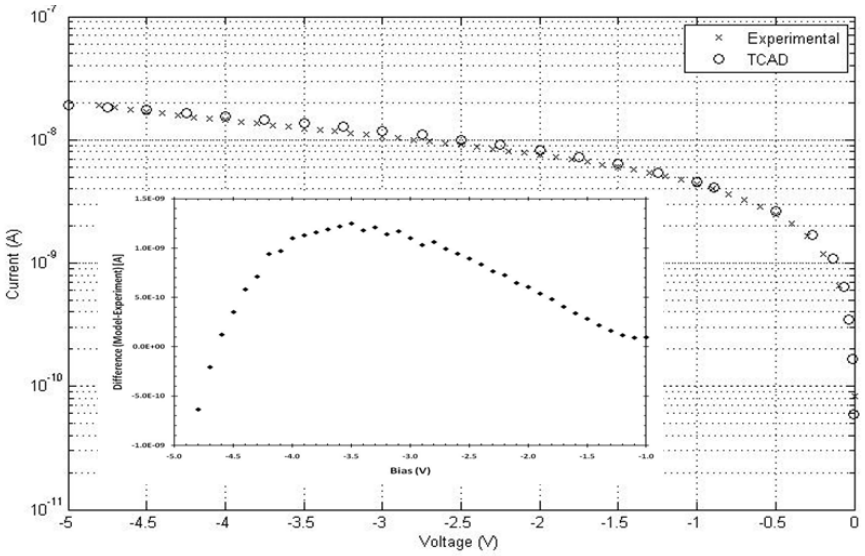

Figure 49. Comparison of TCAD model to experimental results for NDSU#1. Experimental results only exist for up to -5V bias. Inset indicates difference in current between experimental results and the TCAD model.

4.3.3 Sensitivity Results

The benefits of sensitivity studies were outlined in Section 3.4.3. Primarily, the following results will illustrate model consistency, areas of vulnerability, and highlight the parameters of most interest for future research. Only a portion of the results listed in Table 4 will be shown below due to repetitive conclusions and limited space.

The first method to analyze the sensitivity results is as a function of a parameter of interest. This can

1. Illustrate expected changes in the leakage current should research find the parameters used were incorrect,
2. Demonstrate relative sensitivity of the region in which the actual
3. parameter lies in comparison to deviations of that parameter,
4. Illustrate artifacts and/or inconsistencies in the model.

In each of the cases shown below, the absolute sensitivity is plotted for clarity, and the nominal parameter is indicated on the plot. Consistent with the artifacts introduced above, there are some data points that deviate from the general trends depicted in the figures. Some of these are attributable to meshing artifacts, while others are due to a change in the physics. Where applicable, these deviations will be identified and explained.

Figure 50 depicts the sensitivity of the model to changes in the electron affinity. Very high sensitivity values indicate the relatively unstable footing on which the model is based. The electron affinity was determined from heterostructure band analysis as described in Appendix A.1 and is not based on any experimental measurements from literature as was discussed in Chapter II. The large sensitivity arises from the change of the heterojunction band structure with changes in χ. This change reaches a peak at approximately χ=3.9 eV where V_{bi} (the energy gap between the Fermi levels) is at a minimum right before the band structure inverts. Further decreases in χ bring V_{bi} closer to the experimentally determined 0.7 V, albeit in an inverted band structure, thereby causing the decrease in sensitivity shown below 3.8 eV. A general trend also shows higher sensitivity at lower biases. For this reason, zero bias detection was not included in the optimization research. However, the modeling R_0A is only 15% higher than the R_0A determined experimentally, which is indicative of the qualitative agreement with material resistivity in this region. At very low reverse biases near 0 V, TCAD tends to calculate much lower currents than physically possible. Consequently, low bias modeling results tend to be the least comparable to experimental measurements.

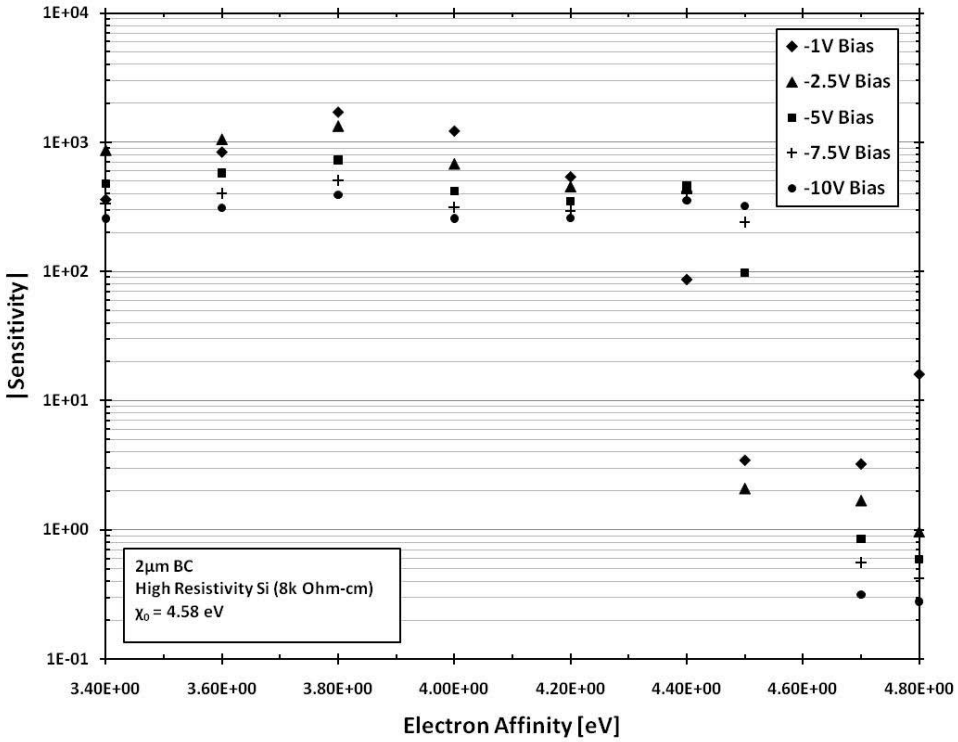

Figure 50. Sensitivity of BC electron affinity.

Figure 51 illustrates the artifact introduced by reaching the maximum number of grids in the simulation. Since the change in current should be directly proportional to the change in device area, the simulated results can be directly compared to the ideal results. The ideal sensitivity can be found by combining the leakage current equation and (10). After simplification the result is

$$S = \frac{\left|r^2 - r_0^2\right|}{r_0\left|r - r_0\right|}, \tag{14}$$

where r is the radius of interest [μm] and r_0 is the nominal radius [μm]. Although the 750 and 800 μm contact radius sensitivity values are very close to ideal, the 850 and 900 μm contact radius sensitivity exceeds the expected ideal values. This is due to the coarse grid in the X and Y planes where the grid spacing is as shown in Table 2. However, the negligible variance of the sensitivity as a function of bias demonstrates model consistency with transport physics as the bias should have no effect on the area's sensitivity.

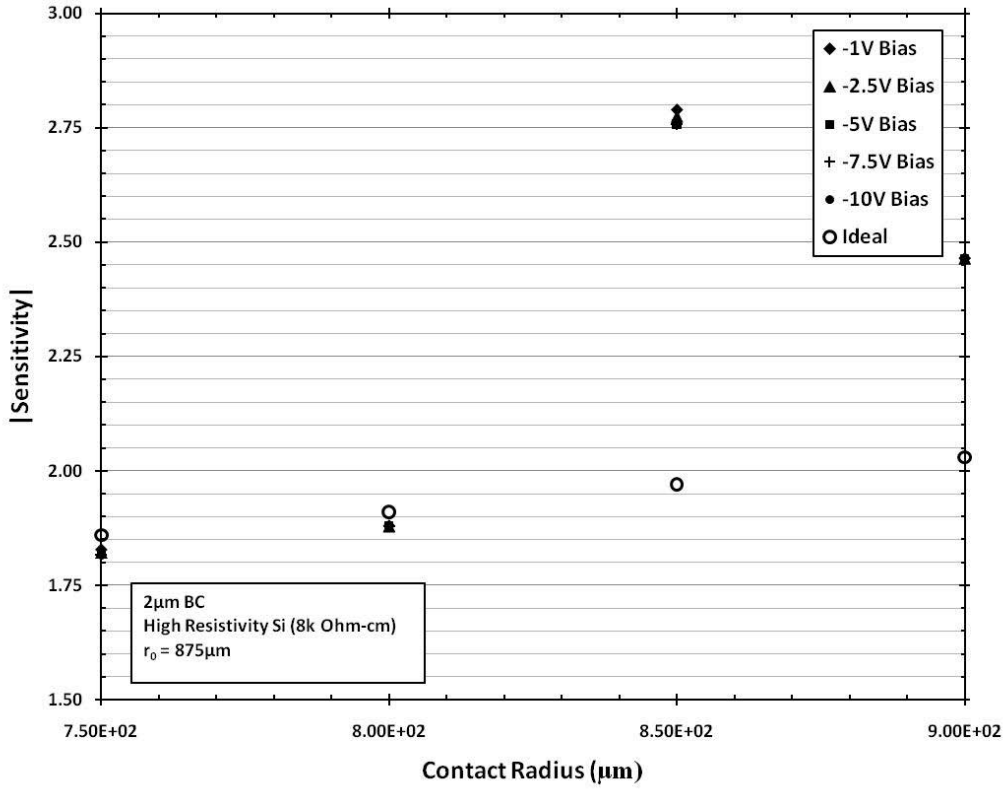

Figure 51. Sensitivity of BC area (contact radius).

Figure 52 shows the band gap sensitivity. These are somewhat idealized results in that the electron affinity would be expected to change with varying band gaps in actual devices, but there is no information on the relationship (or electron affinity in general) resulting in the determination of each parameter's sensitivity in isolation. The results largely reaffirm the electron affinity noted above. The changing band gap alters the band structure significantly, but unlike the electron affinity, it does not invert at any point. Instead, the sensitivity increases as the modeled band gap deviates progressively further from the calculated band structure in Appendix A.1.

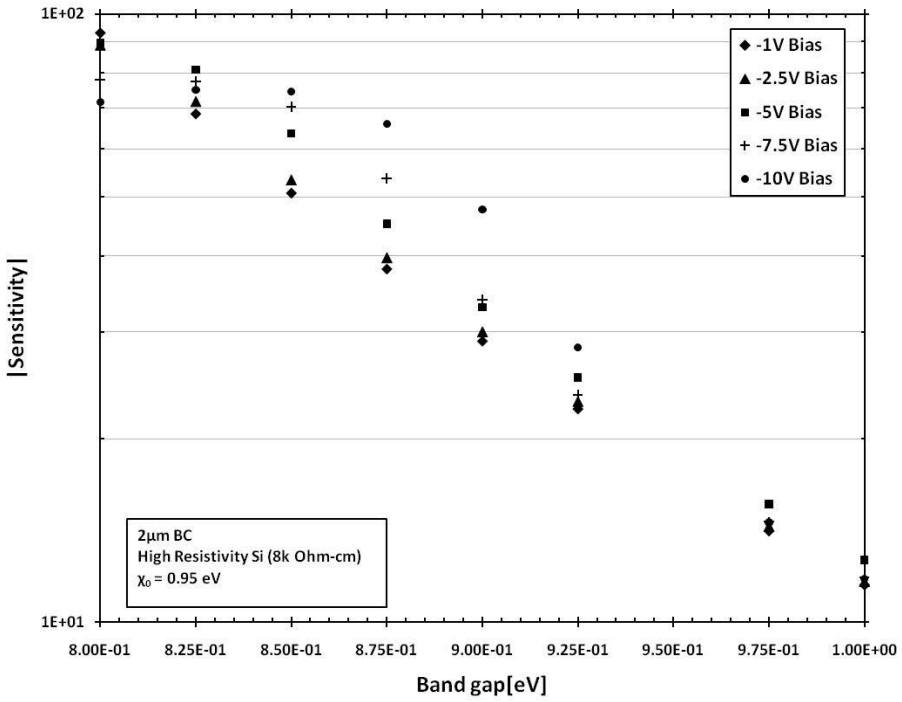

Figure 52. Sensitivity of BC band gap.

The electron and hole mobility sensitivities are shown in Figure 53. These results show that the BC mobility, as in Table 7, is directly proportional to the current. In this region, extrapolated device response is predictable for order of magnitude variations in the mobility assuming a similar ratio between the two is maintained. This feature is useful as expected improvements in fabrication should yield higher mobility through lower trapping.

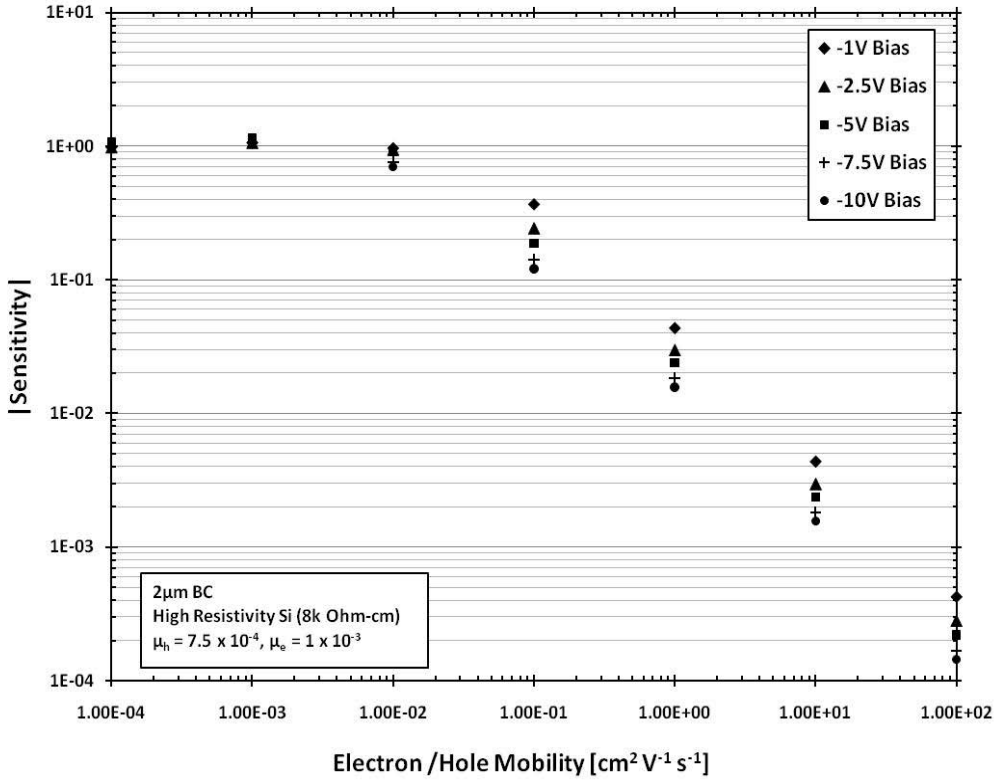

Figure 53. Sensitivity of BC electron and hole mobility.

The N_c/N_v ratio is another parameter from which there was no literature available. In the absence of data, a ratio of one was chosen. As Figure 54

shows, varying this ratio does affect the leakage current as expected but not as dramatically as parameters such as χ or E_g. This information helps stratify the most useful parameters to target for future experimental determination. At high reverse biases ($\square$ -7.5 V), the sensitivity deviates from the lower bias sensitivity at low N_c/N_v ratios. This is the result of the much lower density of conduction band states available for electron excitation. This results in a decrease in the rate of excitations at higher biases and a smaller relative increase in the leakage current thereby producing a smaller sensitivity value.

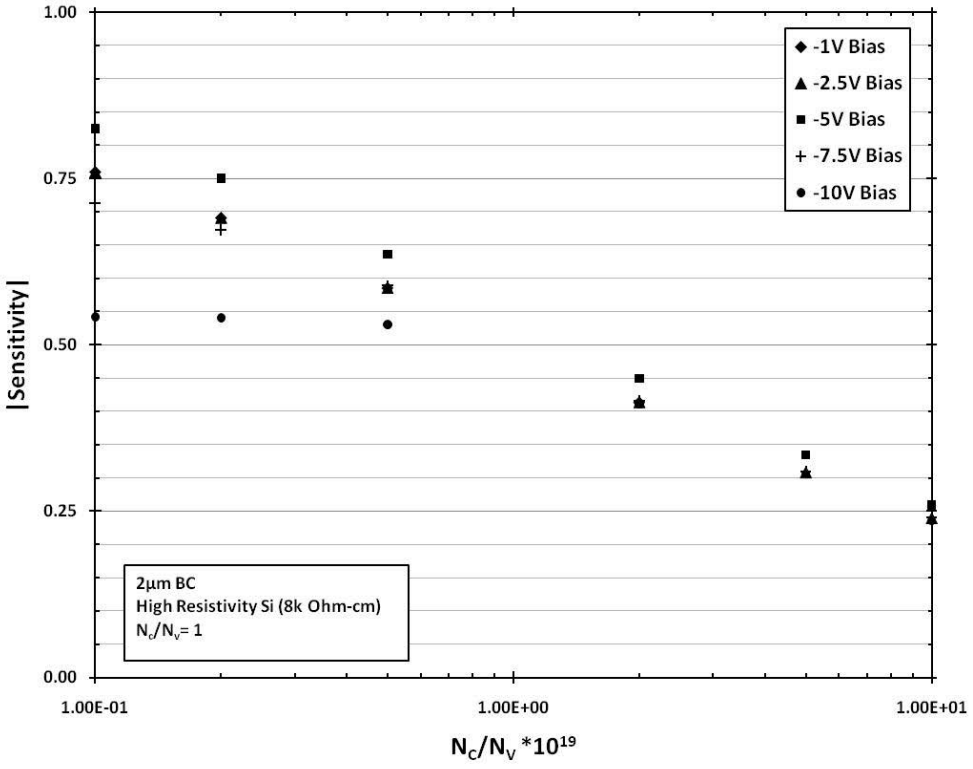

Figure 54. Sensitivity of BC N_c/N_v ratio.

Figure 55 portrays the sensitivity of the model to changes in silicon resistivity. Sensitivities trend to higher values at lower resistivity and higher bias due to an increasing mu-tau product. However, the maximum sensitivity is orders of magnitude lower than E_g or χ.

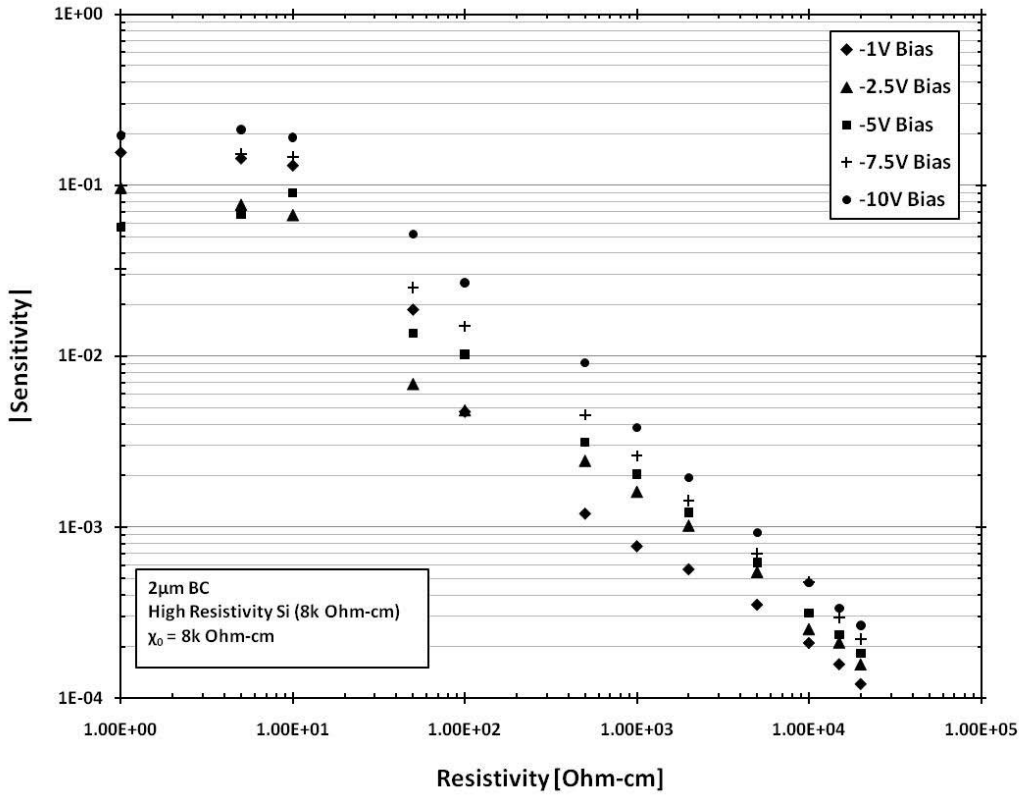

Figure 55. Sensitivity of silicon resistivity.

The second method for analyzing sensitivity results is by plotting the average sensitivity of the parameters as a function of bias. Such a plot is shown in Figure 56. This method is useful to:

1. Demonstrate the relative importance of each factor in terms of the model sensitivity to that parameter,

2. Illustrate artifacts and/or inconsistencies in the model, and

3. Shows regions of increased sensitivity for modeling.

The most striking feature in Figure 56 is the model sensitivity to χ and E_g variations. These parameters drastically alter the band structure and are the most important parameters in terms of future research to improve the model fidelity. Parameters such as the device $r_{contact}$ and N_D are significant, but relatively easily measured for each device. Finally, parameters such as E_g, N_c, N_v, N_c/N_v, μ_e, μ_h, and $r_{contact}$ show little to no discernable bias dependence consistent with semiconductor physics below ~ -7 V. The bias dependence that is evident in these parameters at $>$ -7 V indicates that the effective parameterization of the BC physics properties is not as accurate at higher biases and subject to more uncertainty than when in the range of information available for benchmarks (0 : -5V). Parameters expected to vary with applied voltage (N_D, N_A, χ) do exhibit a bias dependence of the sensitivity value.

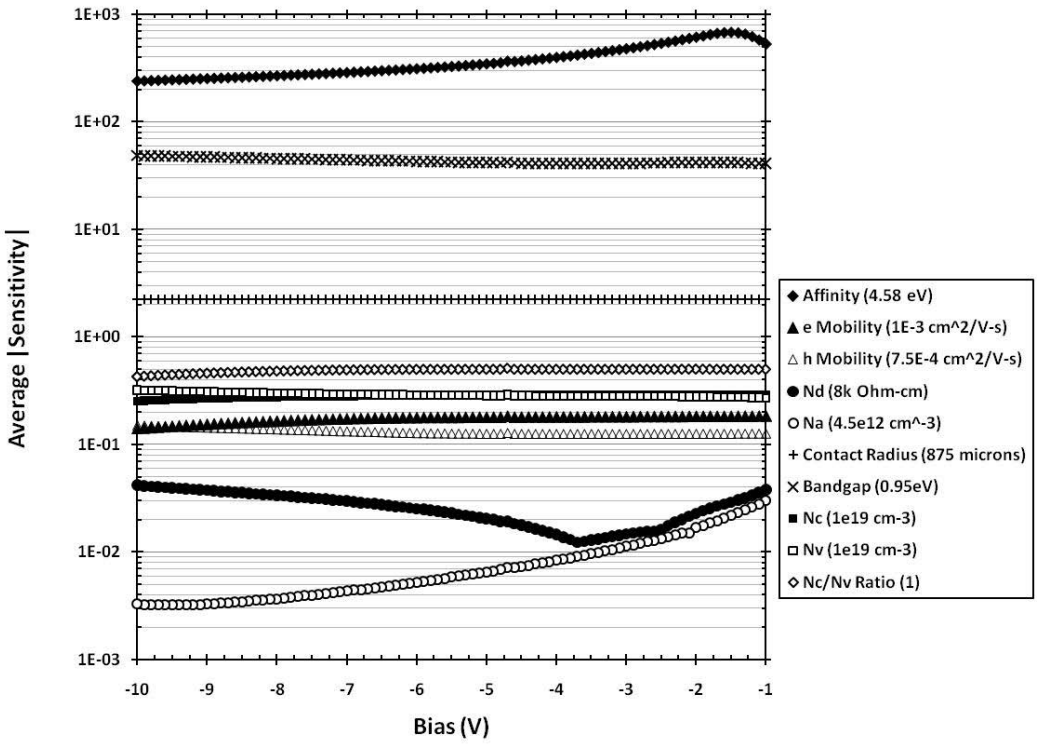

Figure 56. Sensitivity of various parameters as a function of bias.

4.3.4 Optimization Results

Diodes with p-type B_5C on n-type silicon were optimized for S/N and total charge collected, Q. These are two key parameters for detector performance that can be coupled with the efficiency results presented in Section 4.1 to produce a theoretically ideal set of build parameters for future generation diodes. In general, Q is a more useful parameter as described in 3.4.4. As such, the results presented will focus on these, with S/N results shown to identify key differences between the two methods. Where the S/N results are not shown, care will be taken to identify what differences, if any, exist. Finally, collection at

both the BC and silicon contact was optimized. The silicon contact results are presented first.

As with all computational methods, precision and computational time have conflicting requirements. In this case, the transient current was calculated at user-defined points in time. These points were chosen to be tightly spaced where the peak values were expected to occur, but the peak was sometimes not fully captured. Additionally, the Q values are only as accurate as the discretized pulse and the numerical method used to integrate (Simpson's 3/8 Method).

For the case of silicon resistivity the S/N results, Figure 57, parallel the Q results, Figure 58. In both cases, the peak occurs at ~10 Ω-cm. These are analyzed using the mu-tau product. Higher resistivity silicon has a lower mu-tau product indicating longer transit times, higher trapping, and higher recombination. The longer transit times are the primary driver for the decrease in S/N due to an increase in pulse time and the accompanying decrease in pulse height. The longer transit times, which result in higher recombination (due to a higher minority carrier concentration) and charge trapping, reduce the collected charge. As the resistivity decreases, these factors continually decrease resulting in higher S/N and Q. However, below ~100 Ω-cm, the depletion width in silicon starts to decrease below the track length of silicon. Therefore, the reduction in total charge deposited outweighs the benefits of lower resistivity, and a decrease

in the S/N and Q are seen below 10 Ω-cm. The idealized scenario chosen (ion track with the average energy of a ^{4}He ion entering silicon and a track perpendicular to the junction interface) skews the results slightly. Tracks with lower energies, non-perpendicular tracks, or ^{6}Li ions would all result in less penetration into the silicon, requiring a smaller depletion width. Smaller depletion widths would result in a charge collection peak at a lower value of silicon resistivity making resistivity values in the 1 Ω-cm range viable.

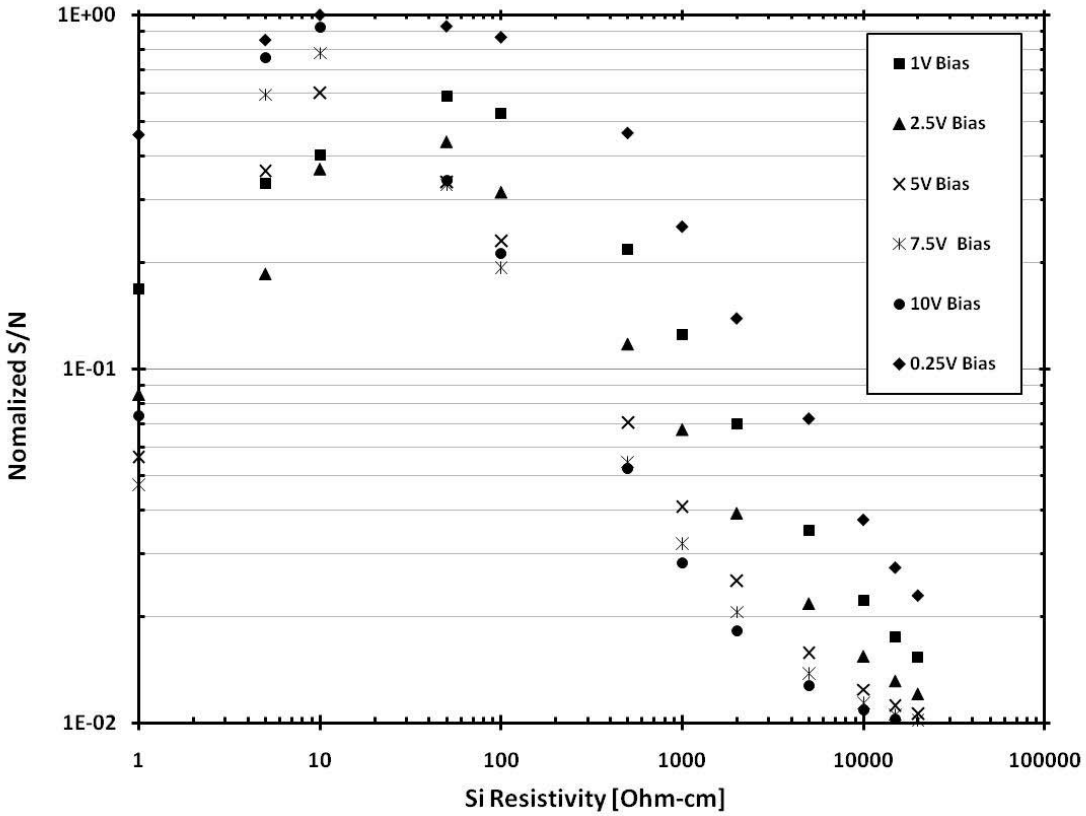

Figure 57. S/N optimization of silicon resistivity for silicon contact collection.

The one distinguishing difference between the S/N and Q results for silicon resistivity is the effect of bias. In Figure 57, the S/N values are peaked for lower biases. This is due to the lower reverse leakage currents dominating the increase in recombination and transit time. However, when considering the charge collected, higher biases lead to less recombination, less trapping, and a higher Q. The normalized Q for collection at the silicon contact was functionalized in a piece-wise form given by (15).

$$\begin{aligned} Q_{\rho_{Si}}^{SCCon} &= \left(0.095\left|V_{app}\right|+0.05\right)\left(-0.017\rho_{Si}^{2}+0.2867\rho_{Si}-0.1843\right) && for\ \rho_{Si} \le 10\Omega - cm \\ Q_{\rho_{Si}}^{SCCon} &= 1.34\left|V_{app}\right|\rho_{Si}^{-0.96}+4.2\rho_{Si}^{-0.96} && for\ \rho_{Si} > 10\Omega - cm \end{aligned} \quad (15)$$

Figure 58 shows the above fit to the -10 V data set; further fittings are not included for clarity. In general, the function agrees to less than 10% for $\rho \le 10$ Ω-cm and for $\rho \ge 500$ Ω-cm while agreeing with the remaining range of resistivities to within a factor of two.

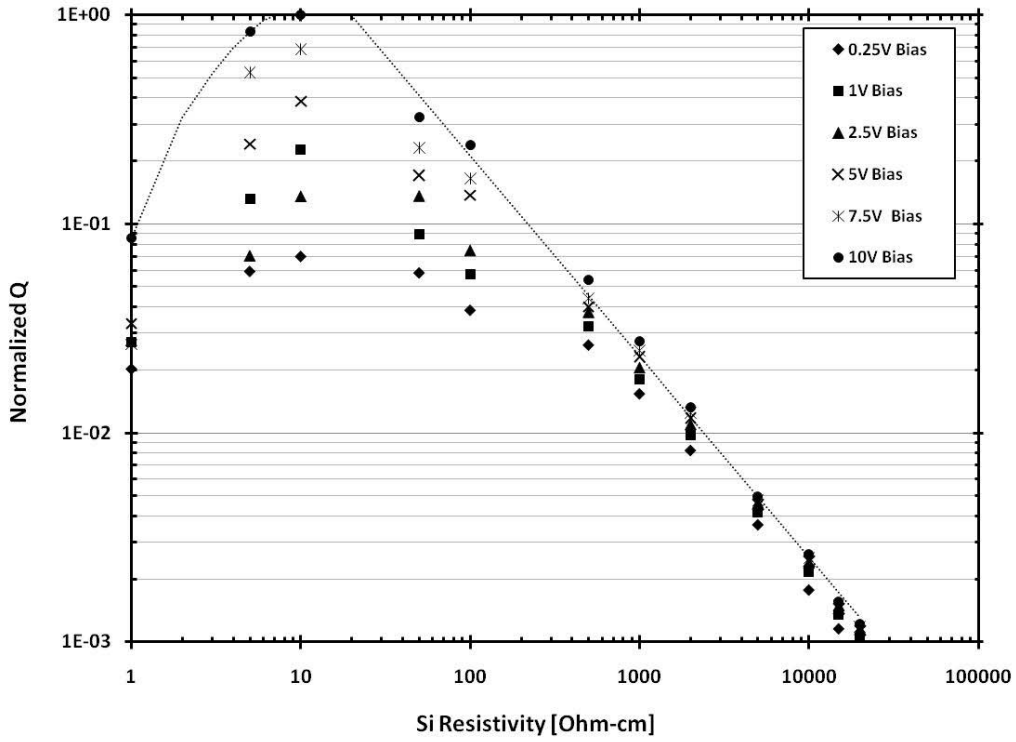

Figure 58. Q optimization of silicon resistivity for silicon contact collection.

Optimizing silicon thickness is rather intuitive but useful to quantify. As shown in Figure 59, as the silicon thickness decreases, the probability of charge trapping is reduced. The bias dependence also applies where higher bias results in higher Q. The S/N results are similar, albeit with different normalized values, and the caveat that the lower bias produces higher S/N due to the dominance of the reduced leakage current. A functional form parameterizing the increase in normalized Q for changes in silicon thickness is given by

$$Q_{t_{Si}}^{SiCon} = \left(1.49 - 0.00315 t_{Si} + 2.44 * 10^{-6} t_{Si}^2\right) \left|V_{app}\right|^{0.7}. \qquad (16)$$

Values computed from (16) are generally within 4% or better of the TCAD produced Q values.

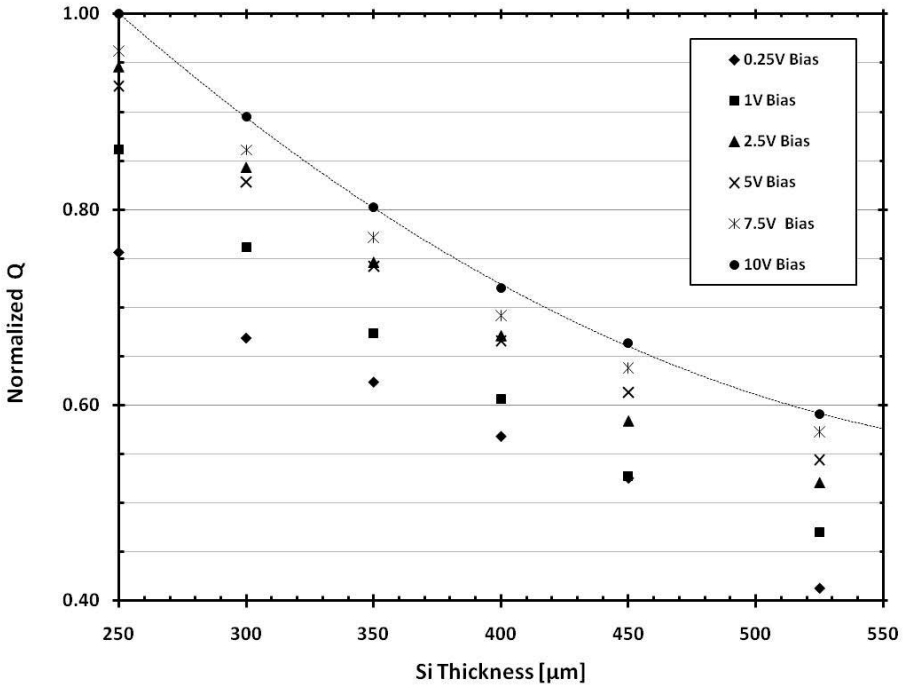

Figure 59. Q optimization of silicon thickness for silicon contact collection.

The BC thickness also affects S/N and Q for silicon contact collection as shown in Figure 60. Due to the orientation of the ion track in BC, parallel to the junction interface, the effects of increased charge collection from thicker BC layers is not accounted for. However, because of the very high resistivity of the B_5C, the reverse leakage current decreases with increasing B_5C thickness. This results in an increasing S/N ratio with increasing B_5C thickness. The bias dependence for S/N is attributable to reduced leakage at lower biases.

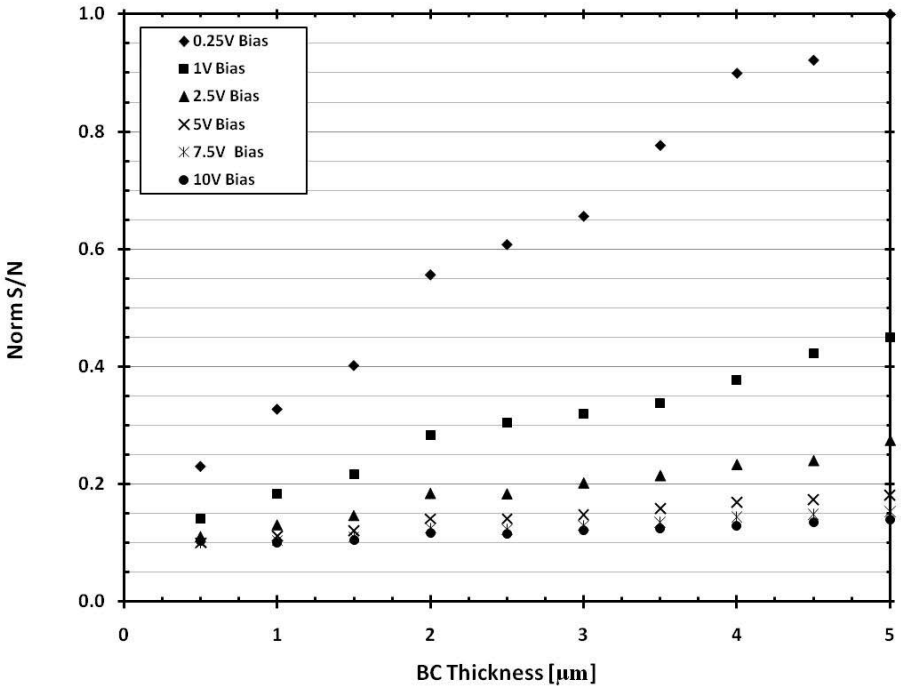

Figure 60. S/N optimization of BC thickness for silicon contact collection.

Figure 61 shows the effects from varying BC thickness on Q. These results trend towards higher Q at smaller BC thickness and higher bias. This is attributable to the higher electric fields existing in both the silicon and BC layers when thinner BC is used. These higher electric fields reduce the recombination of the ion-induced e-h thereby increasing the total charge collection. Additionally, the higher electric field enables a portion of the electrons to cross the junction with sufficient timing (tens of ns or less) in order to contribute to the transient silicon pulse. Other than the 0.5 µm at -10 and -7.5 V bias, this effect is minimal. These two values may be artifacts and not truly representative of expected gains in Q. Ignoring those two points, the

normalized Q as a function of BC thickness and bias at the silicon contact can be found from

$$Q_{t_{BC}}^{SiCon} = t_{BC}^{-0.18}\left(0.0093\left|V_{app}\right| + 0.224\right). \quad (17)$$

This equation provides results that are consistent with the computed Q values to $< 15\%$ over the range of biases and thicknesses presented in Figure 61. For comparison, (17) is plotted at -10V in Figure 61.

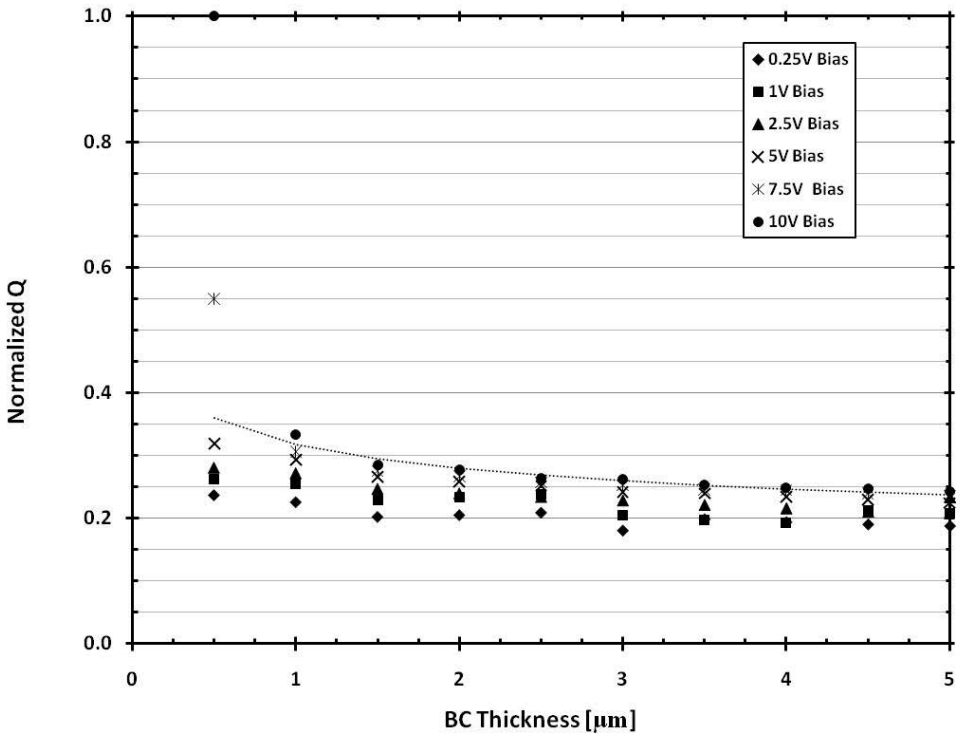

Figure 61. Q optimization of BC thickness for silicon contact collection.

It is different when collecting from the BC contact. For example, the silicon resistivity had a very substantial impact on Q from the silicon contact.

However, as is shown in Figure 62, it has negligible impact due to the very short diffusion mu-tau for holes to the junction ($< 3.5\mu m$). There are trends towards slight reduction in Q for higher values of resistivity. The non-uniformity noted in Figure 62 are artifacts due to discretization of the current pulse described previously in this section.

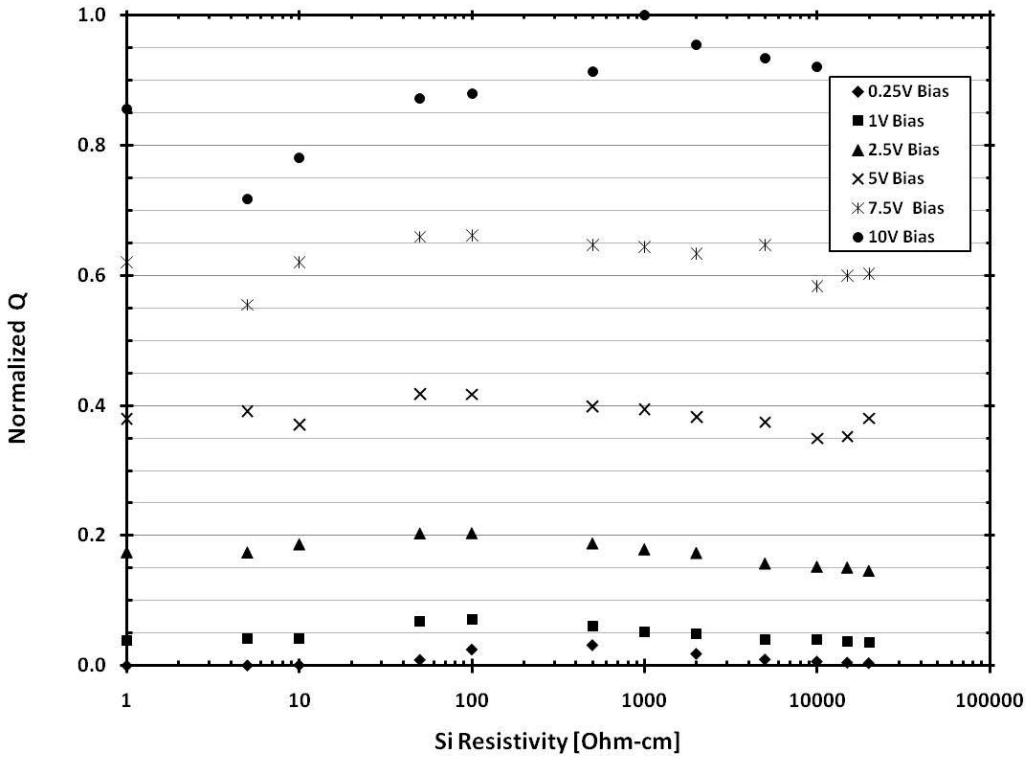

Figure 62. Q optimization of silicon resistivity for BC contact collection.

Figure 63 shows that the silicon thickness, while important for the charge collected at the silicon contact, is a not a factor in increasing S/N or Q. This is due to the small depletion widths ($\leq$ five microns) necessary in silicon to collect

the charge. However, Figure 63, and to a lesser extent Figure 62, definitively shows the influence on Q of increasing bias in the absence of other parameter changes. By averaging the Q values at each bias, a functional form for normalized Q as a function of applied bias at the BC contact is given by

$$Q_{bias}^{BCCon} = 0.0464 * \left| V_{app} \right|^{1.27}. \quad (18)$$

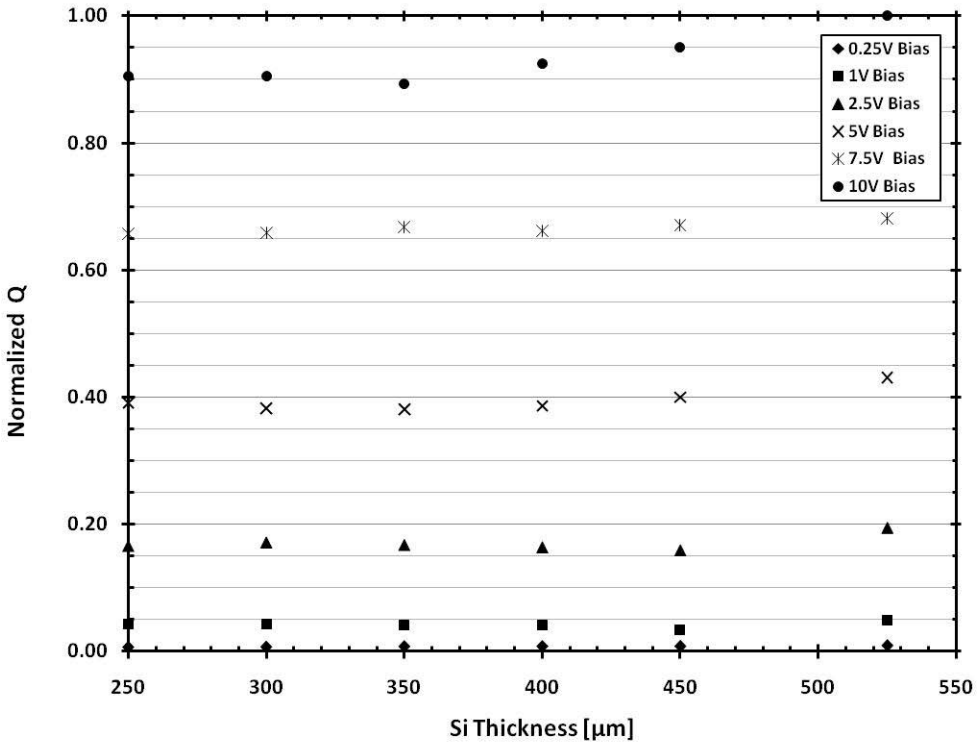

Figure 63. Q optimization of silicon thickness for BC contact collection.

The most important parameter affecting the Q in BC is the BC thickness. The physical process by which the total charge collected is reduced is very similar to that noted above for increasing silicon thickness. The key difference

for the BC results is that BC has a much higher trapping probability and lower mobility than silicon. This leads to a greater decrease in Q for increases in BC thickness as shown in Figure 64. The normalized Q for a given BC thickness and applied bias is approximated by

$$Q_{t_{BC}}^{BCCon} = \left(0.0072t_{BC}^4 - 0.11t_{BC}^3 + 0.616t_{BC}^2 - 1.55t_{BC} + 1.64\right) * \left(0.104\left|V_{app}\right| + 0.039\right). \quad (19)$$

This approximation is less accurate than previous ones. Generally, the results are within a factor of two or better for biases above 1V.

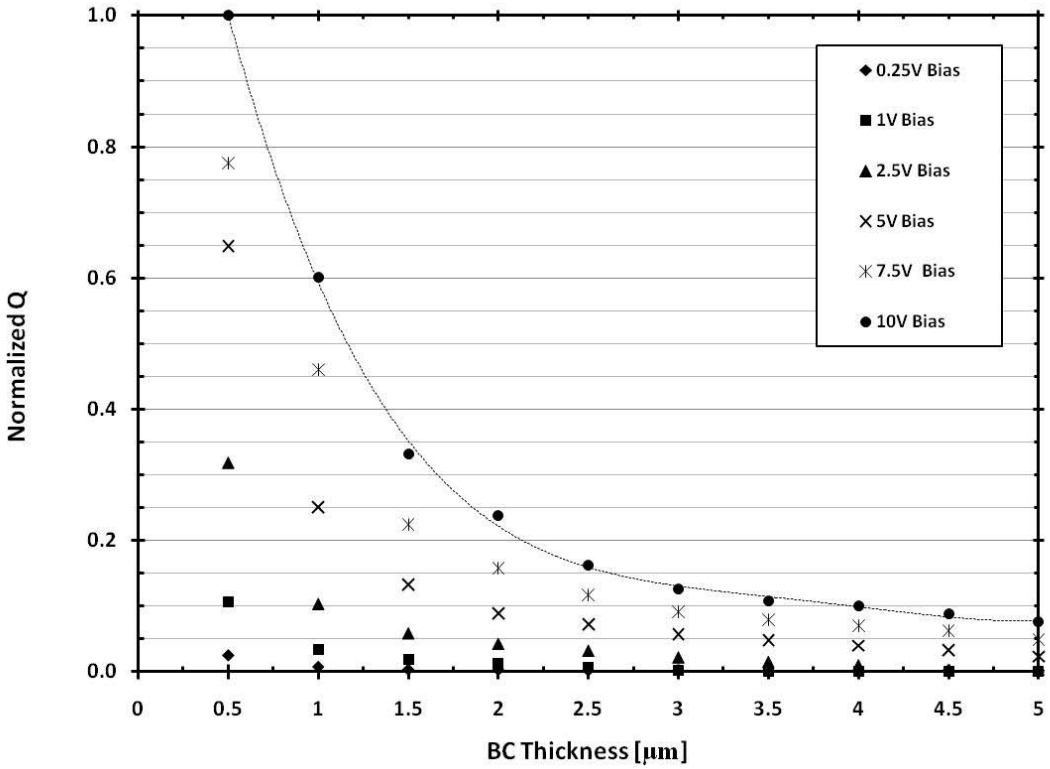

Figure 64. Q optimization of BC thickness for BC contact collection.

Changes to BC resistivity had no impact on the charge collection at either contact as shown for the BC contact in Figure 65. This is more indicative of an artifact of the method in which the model was developed. The physics to control doping dependence lifetime and mobility within the semi-conducting BC is not well defined since effective parameters were used. Therefore, in the absence of this physics, the models necessary to effect changes in the mu-tau product (the driving mechanism for the change in Q or S/N for varying resistivity) were not included. The same logic that applied to the silicon substrate would theoretically apply here in that lower resistivity should result in higher Q due to a higher mu-tau product. The primary difference would be the absence of a peak due to full depletion of BC even at 0 V bias. However, no experimental evidence exists to support this claim at this time.

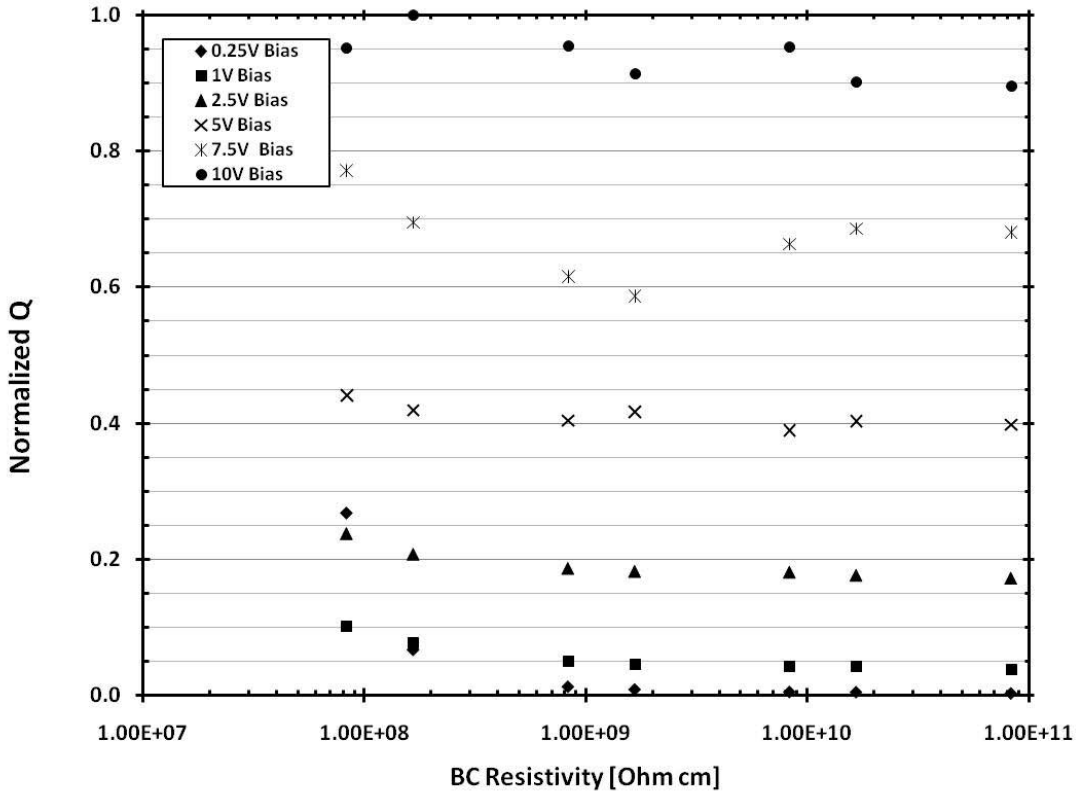

Figure 65. Q optimization of BC resistivity for BC contact collection.

This section has presented several methods for optimizing Q and the efficiency by varying parameters. In order to support an optimization method, one would need:

1. Experimental results that could be used to scale the normalized Q values and

2. A MDL for an intended detection system.

Unfortunately, neither of these are available at this time. Instead, the parameterization methods presented in equations (12) and (15) - (19) can be used to estimate the relative charge collection for a given set of growth and

operation parameters. When the charge collection for a given diode is determined experimentally, (15) - (19) can be scaled to estimate the charge collection for future growths. Given a MDL, this can be combined with (12) to determine the optimum design parameters and operating conditions necessary for each application.

By presenting normalized Q results and allowing for future scaling to experimental values, the effect of model assumptions and simplifications is minimized. For example, the orientation and amount of energy deposited in each detection layer impacts on the absolute charge collection. In the model, an idealized scenario was chosen. However, by normalizing the resulting Q its effect on the parametric functions is minimal, whereas the impact on an un-normalized function representing Q would change by as much as a factor of two.

V. Radiation Effects Measurement Methodology

5.1 Devices

Five B_5C diodes were obtained from NDSU and UMKC to determine the effects of NIEL induced device degradation and device lifetime. The diode characteristics are listed in Table 9. NDSU#1 was irradiated in an experiment conducted on 9 September 2010, and the others were irradiated on 15 and 17 December 2010. NDSU#4 was never irradiated due to wire bonding failure prior to the experiment. The UMKC growth process was relatively new, while the NDSU process had been used to produce diodes for research in the past.

Table 9. Diode characteristics. Each diode had a 2μm PECVD B_5C layer.

Name	ρ_{Si}	$A_{contact}$	Test Location	Comment
NDSU #1	8k Ω-cm	0.024 cm^2	Thermal Column	09Sep10 irradiation
NDSU #2	20k Ω-cm	0.031 cm^2	Thermal Column	As Deposited
NDSU #3	20k Ω-cm	0.039 cm^2	Thermal Column	As Deposited
NDSU #4	20k Ω-cm	0.062 cm^2	Thermal Column	Heat Treated
UMKC #1	20k Ω-cm	1.96 cm^2	Thermal Column	SiN cap

The devices were shipped in aluminum mounting hardware with a single BNC connection as shown in Figure 66. This setup was insufficient for neutron irradiation experiments due to:

1. A high metal content that would become activated and

2. No straightforward way to integrate a second BNC mount to allow for C-V measurements.

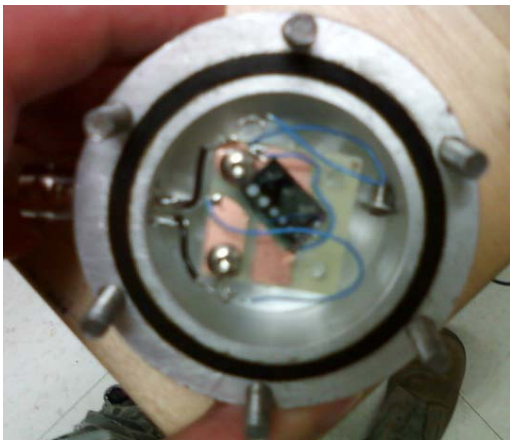

Figure 66. Diode and mount as shipped from UMKC and NDSU.

Mounting hardware was developed for each intended irradiation location. The thermal and 7" column mounts are depicted in Figure 67. Each was designed to allow for in-situ measurements for up to three devices at a time. To limit thermal neutron absorption and flux distortions, the thermal column mount was designed to limit material near the diode. The 7" column mount included a cadmium lined cavity to "harden" the neutron spectra, to allow damage attribution to fast (1 MeV equivalent) neutrons and limit boron capture product damage.

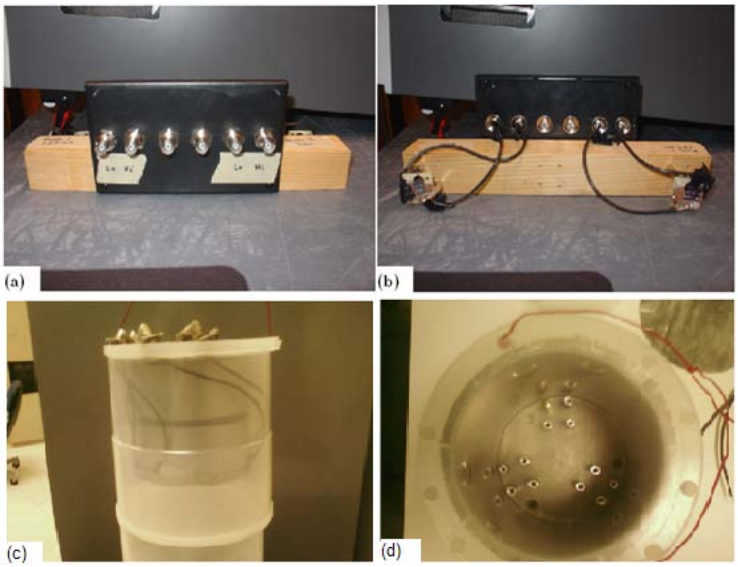

Figure 67. Diode mounts developed to control up to three diodes for in-situ measurements. (a) Front of thermal mount. (b) Back of thermal mount. (c) Outside view of 7" mount's cadmium cavity. (d) Inside view of 7" mount's cadmium cavity.

5.2 Data Collection

To quantify the effect of NIEL damage in B_5C, in-situ C-V and I-V characteristics were measured throughout the irradiation. The following sections describe the equipment used and methodology employed in taking these measurements. Additionally, the procedures used to pre-characterize the diodes and flux are specified.

5.2.1 Equipment

The following equipment, as shown in Figure 68, was used in the irradiation experiments:

1. Kiethley 4200 Semiconductor Characterization System

2. Kiethley 590 C-V Analyzer

3. Kiethley 707 Switch Box

4. RG-58 BNC cables and adapters

Figure 68. Equipment set-up at Ohio State Research Reactor (OSURR).

5.2.2 Collection Methodology

The use of the Keithley 4200 allowed for full automation of the measurement process in KITE using user-developed code written in its C-based KULT program. The programs that were developed are included in Appendix B.3. In general, the automation scheme allowed for I-V and C-V measurements (with user specified range and step size for each) to be taken utilizing a user-specified number of diodes. The measurements were taken at user-defined timing intervals which, could be asymmetric. An average and standard deviation of the current was obtainable by allowing a user-specifiable number of I-V curves to be taken at each interval for each diode. A similar capability for C-V

measurements does not exist due to the time required to take C-V curves, but it also is not necessary due to the much more stable results obtained from C-V measurements. The parameters used for the irradiations and pre-characterization routines are shown in Table 10.

Table 10. KITE automation input parameters.

Parameter	Value
I-V Range, Step Size	1:-10V, 0.1V
C-V Range, Step Size	1:-10V, 0.5V
IV Loops	4
Loop Time	~42 seconds
Loop Rate	~1 min^{-1}
Measurement Time	4 hrs

5.2.3 Pre-Characterization Procedures

The following pre-characterization measurements were taken for each diode:

1. I-V and C-V curves of each device,
2. I-t and C-t profiles for each device, and
3. A full four hour automated run of I-V and C-V curves.

The first pre-characterization provided information allowing for quantitative comparison of each device in a small data set. It, however, was not used as the background measurements from which the radiation induced increase (decrease)

in current (capacitance) was compared. Instead, the third characterization listed above allowed for a measurement-by-measurement comparison of the pre- and post-irradiation results thereby accounting for the increase (decrease) in current (capacitance) as a function of time under bias. The second pre-characterization was performed to quantify the shifts of C-V and I-V characteristics as a function of time under bias.

5.2.4 Flux Measurements and Equivalency Procedures

Flux measurements were taken in the thermal column at the location where the diode mount was to be placed. This is defined as stringers G6 – G8 with 24" of graphite block removed. Cadmium covered and bare gold foils were mounted on a 2x4 and placed at the center point corresponding to each stringer. They were then irradiated for approximately 30 min, and the resulting activated foils were counted. The results are summarized in Table 11.

Table 11. Cadmium difference flux measurement results from thermal column at OSURR. All measurements accurate to $\pm$ 20%.

Location	Thermal Flux [n cm^{-2} s^{-1}]	Fast Flux [n cm^{-2} s^{-1}]	Cadmium Ratio
G6	5.17×10^{9}	9.38×10^{6}	551
G7	5.64×10^{9}	9.77×10^{6}	577
G8	5.44×10^{9}	9.44×10^{6}	576

To facilitate comparison to the 1 MeV neutron equivalent results shown in Chapter II, an equivalency scheme was developed. This methodology is described in Appendix A.2. For a 20k Ω-cm silicon substrate, an approximate thermal flux of 3.5×10^{13} n cm^{-2} is needed to obtain type inversion.

Flux spectra measurements were provided for the 7" column by the reactor staff for a point 12" from the bottom of the column. Using an approximation, this spectrum was converted to a 1 MeV neutron equivalent flux through the procedures outlined in ATSM 722 by subtracting off the 0.3 eV (cadmium cutoff) and lower portion of the spectrum [85]. This approximation is justified on the basis of relative damage contributions. The uncorrected flux profile is shown in Figure 69.

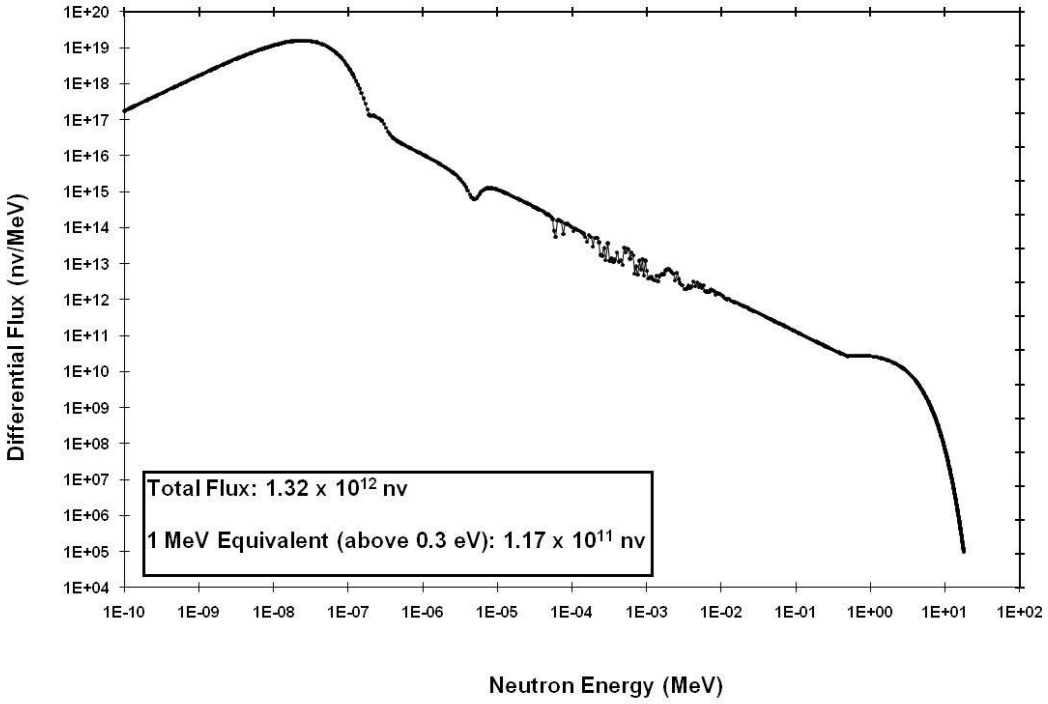

Figure 69. 7" column flux profile with total and 1 MeV neutron equivalent fluxes indicated.

5.3 Irradiation Procedures

5.3.1 Thermal Column

Diode irradiations in the thermal column were conducted on the 15th (NDSU#2 and NDSU#3) and 17th (UMKC#1) of December. The reactor was operated at 10% power for 15 minutes and 90% power for 3.75 hours. The measurement equipment was arranged as shown in Figure 68 with the diode mount placement illustrated in Figure 70. In-situ measurements were taken as described in Section 5.2.2.

Figure 70. Diode mount placement in thermal column.

5.3.2 In pool 7" Column

Due to anomalous results obtained from the diodes irradiated on the 15th of December, as described in Chapter VI, the diodes originally scheduled for these irradiations (NDSU#4 and UMKC#1) were instead switched to thermal column irradiations in an attempt to corroborate the previous results obtained with NDSU#1 or those obtained on the 15th of December.

VI. Radiation Effects Results and Analysis

6.1 Pre-characterization Results

Devices NDSU#1 - #4 and UMKC#1 were characterized as described in Section 5.2.3. These results establish a baseline from which to compare a device pre- and post- irradiation. Additionally, the pre-characterizations allowed for inter-device comparison and identification of anomalous devices. I-V characteristics of all five devices are shown in Figure 71. There is significant variability amongst the five in terms of rectification and leakage current. Due to device area differences, a more useful comparison is the current density as a function of voltage as shown in Figure 72. The only devices that compare favorably are NDSU#1 and NDSU#3, albeit with NDSU#3 having much lower rectification. The other devices have leakage current densities that are an order of magnitude higher or lower than NDSU#1 and NDSU#3. NDSU#2-#4 and UMKC#1 all have significantly lower rectification than NDSU#1. NDSU#1 is taken as the nominal case from which others are compared. Although UMKC#1 also exhibits strong diode characteristics, the large area and poor leakage current limit the quality of the results that are obtainable.

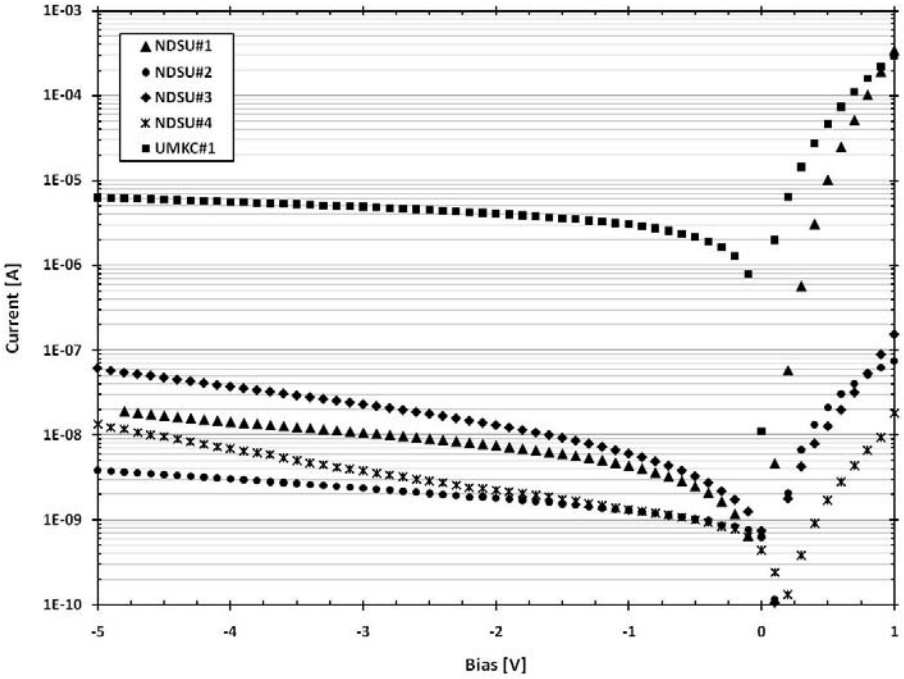

Figure 71. Pre-Irradiation I-V characteristics of B_5C diodes.

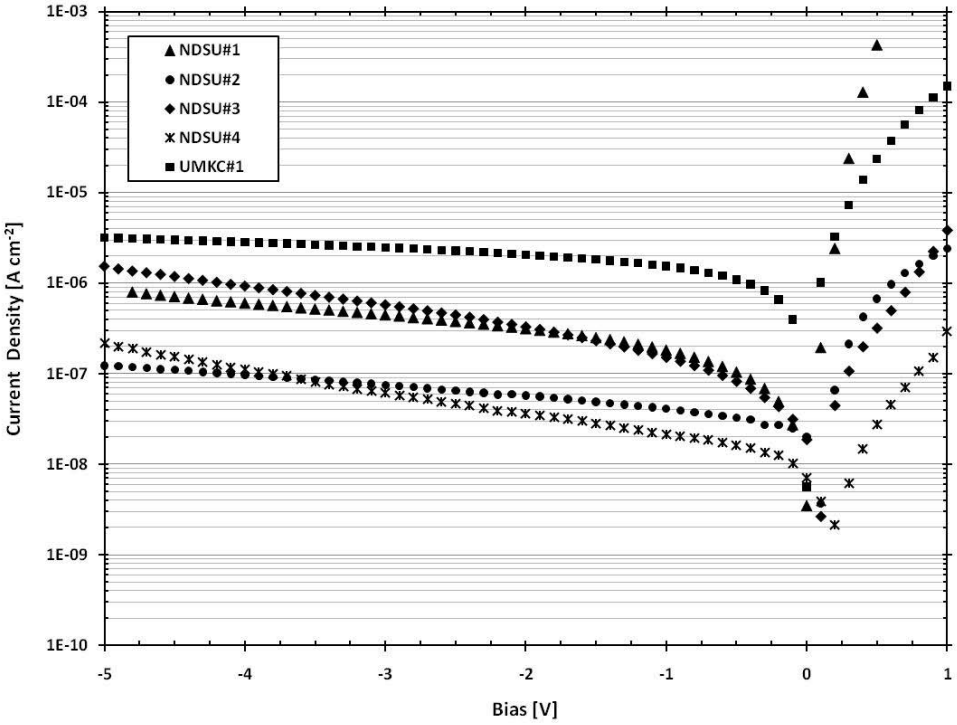

Figure 72. Pre-Irradiation current density characteristics of B_5C diodes.

C-V characteristics are presented in Figure 73 for all five diodes. Two observations are immediately apparent. First, the shapes of NDSU#2 - #4 do not correspond to the expected C-V curve for a diode. In diodes, as the reverse bias increases, the depletion width increases thereby lowering the capacitance. The opposite effect takes place in NDSU#2 - #4 where the capacitance increases after a period of approximately constant capacitance ($<$ -3V). This relationship is more typical of a p-MOS capacitor with a large offset from positive fixed charge. This, however, is inconsistent with stated growth on n-Si. Lacking other data, explanation for this behavior is not consistent with the measured I-V characteristics and is left unresolved.

Second, the capacitance varies by almost two orders of magnitude between devices. Since the device areas are significantly different, it is once again instructive to look at the capacitance density as shown in Figure 74. However, in this case, the capacitance density of NDSU#1 is two to three orders of magnitude greater than the other devices. While a portion of this is attributable to the lower resistivity of NDSU#1 (8k Ω-cm) compared to the other devices (20k Ω-cm), this large increase in capacitance density is unexplainable in terms of known growth parameters and processes.

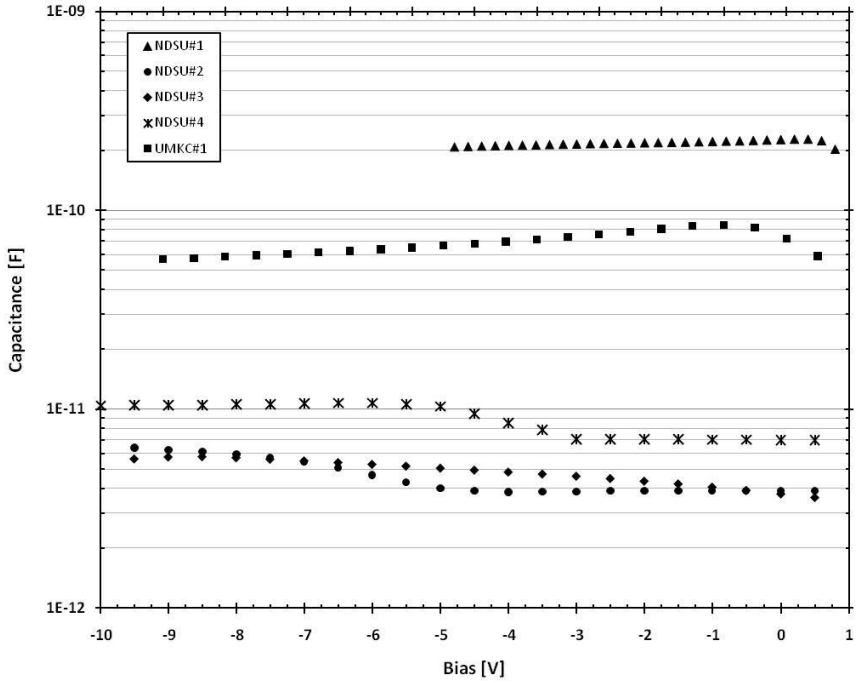

Figure 73. Pre-Irradiation C-V characteristics of B_5C diodes.

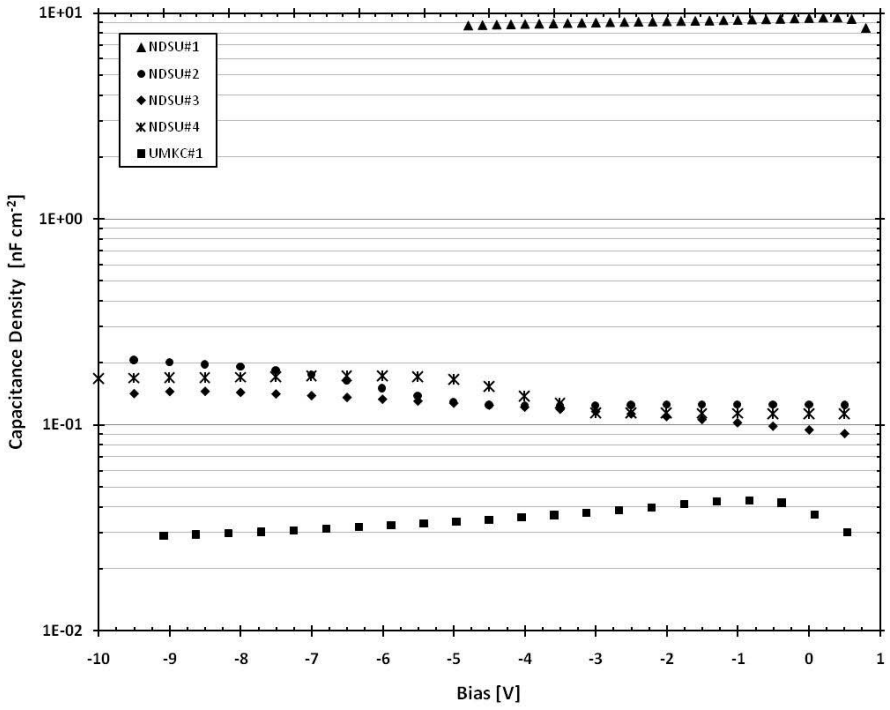

Figure 74. Pre-Irradiation capacitance density vs. applied bias for B_5C diodes.

Finally, C-t and I-t characteristics were measured to quantify variation with time under bias present in the diodes. The UMKC#1 results are presented in Figure 75. No significant trends occur as a function of time, but current measurements deviate from measurement to measurement. The variation is minimized by taking multiple I-V curves at each fluence interval as described in Section 5.2.2. On the other hand, capacitance measurements do not vary significantly from measurement to measurement. For this reason, and those outlined in Section 5.2.2, only single C-V curves were measured during irradiation at each fluence interval.

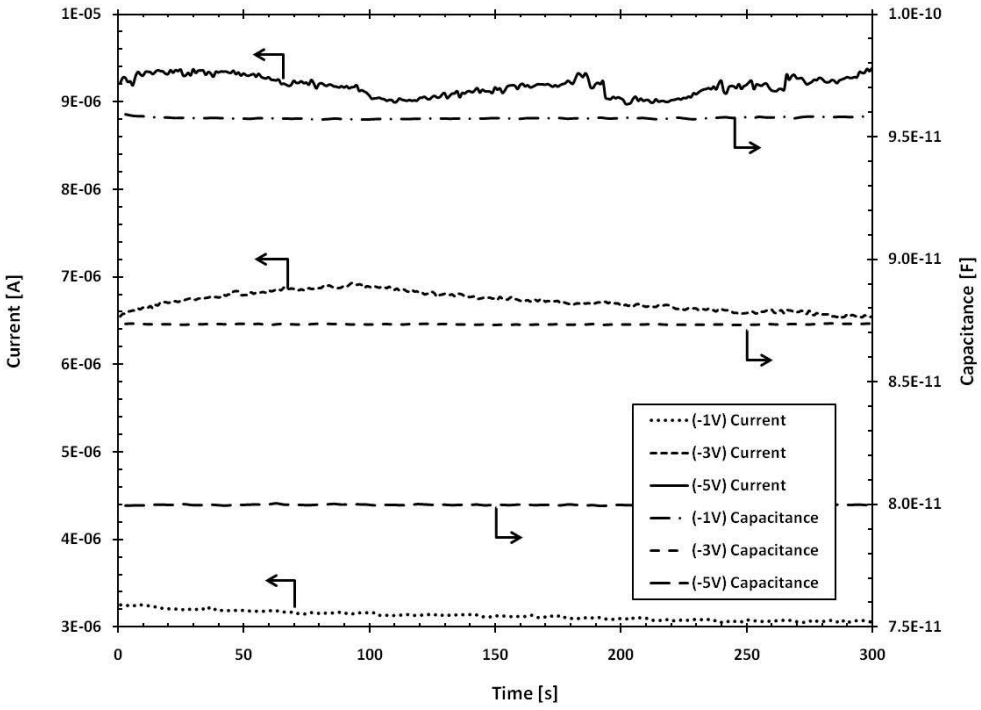

Figure 75. Current and capacitance as a function of time for UMKC#1 at various biases.

6.2 Thermal Column Irradiation Results

Owing to the non-diode-like characteristics noted in Section 6.1 from NDSU#2-NDSU#4, the irradiation results presented are limited to UMKC#1 and NDSU#1. All of the 1 MeV neutron equivalent fluence values were computed as described in Appendix A.2 and Section 5.2.4. Since the 7" tube measurements (fast neutron) were not performed for the reasons outlined in Section 5.3.2, the procedure to equate the thermal neutron induced boron capture products to a 1 MeV neutron equivalent has not been benchmarked. As such, the values may not be accurate.

6.2.1 Leakage Current

As described in Section 2.5, knock-on damage from NIEL events in semiconductors increases the leakage current through the creation of defects which serve as tunneling sites and generation/recombination centers. This effect is shown for NDSU#1 in Figure 76 and Figure 77. Figure 76 shows the increase, ΔI, as a function of thermal and 1 MeV equivalent neutron fluence. This increase is detrimental for detectors as it serves to lower the S/N, resulting in a loss of low energy deposition detection events. After a total thermal (1 MeV neutron equivalent) fluence of 9.7×10^{13} (1.3×10^{13}) n cm^{-2}, the reverse leakage current increased an average of approximately 340%. Additionally, Figure 77

demonstrates that a change in rectification, which typically accompanies type inversion, was not observed with the total fluence levels achieved.

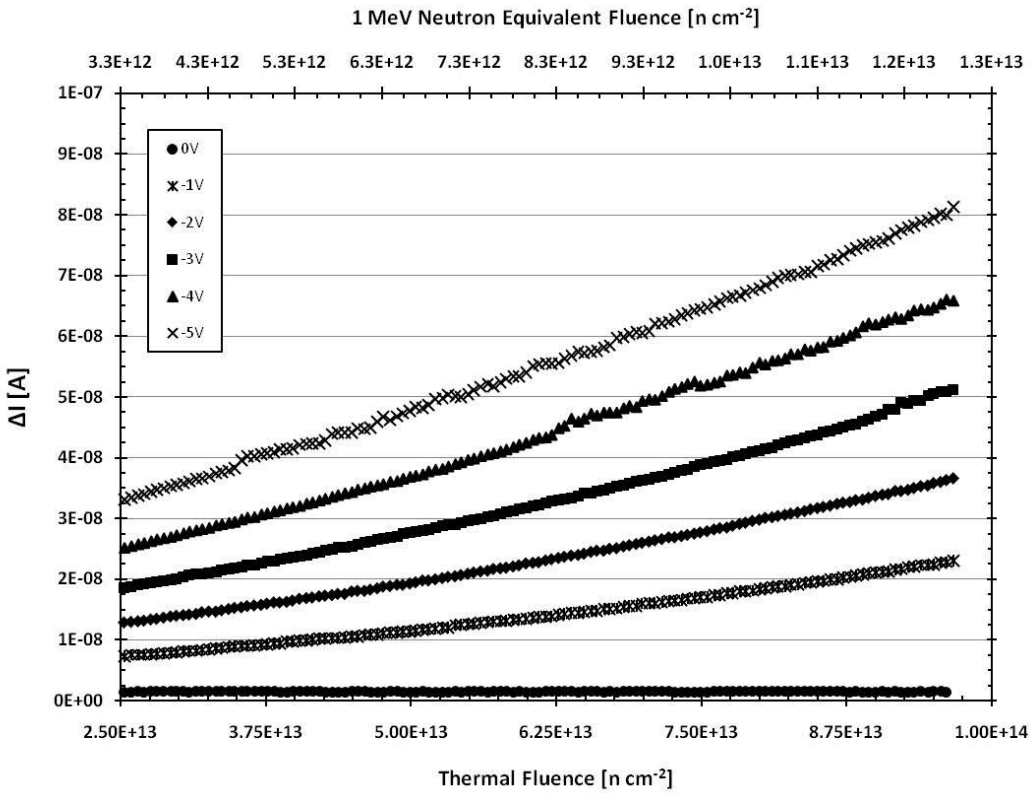

Figure 76. Increase in current as a function of total fluence at various biases for NDSU#1. Error bars are smaller than point size.

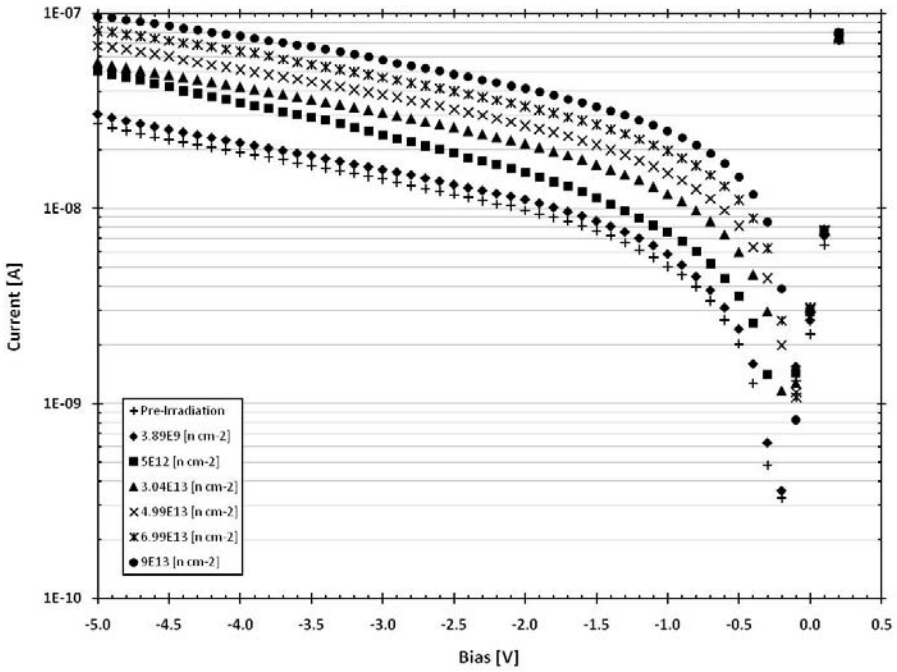

Figure 77. I-V curves for NDSU#1 as a function of total thermal neutron fluence. Error bars are not present for clarity, but standard deviation was approximately 1% for all bias points.

The I-V relationships as a function of fluence for UMKC#1 shown in Figure 78 do not follow the NDSU#1 results shown in Figure 77. This is due to the much higher current densities present in the UMKC#1 device (see Figure 72). This device is a first-of-its-kind produced in UMKC's new growth process. As such, the increase in current density is likely due to a much higher density of interface and bulk BC defects that act as tunneling and generation/recombination sites resulting in a greater leakage current as compared to NDSU#1. With an increased intrinsic density of defects, higher total fluences would be required to introduce the measureable quantities defects necessary to produce observable increases in leakage current.

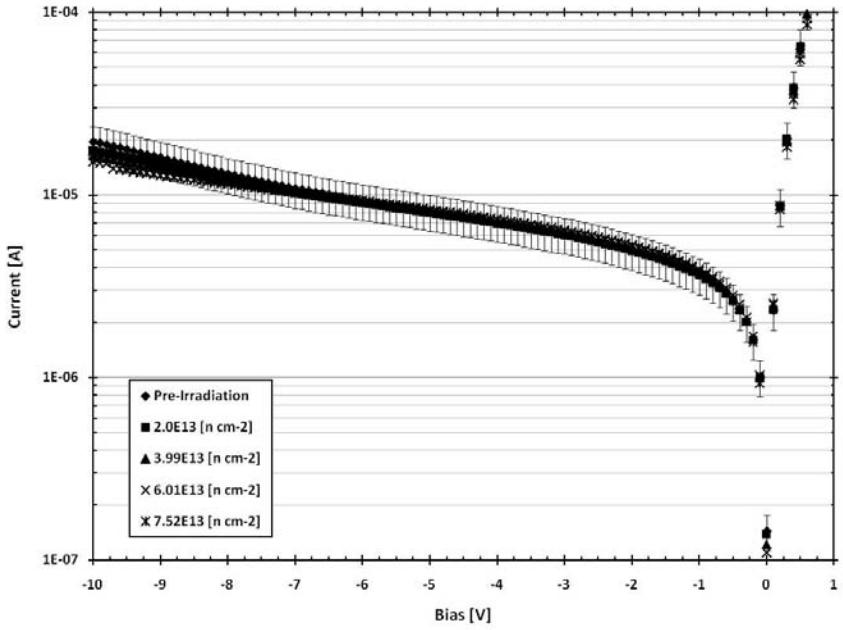

Figure 78. I-V curves for UMKC#1 as a function of total thermal neutron fluence. Error bars are included on the pre-irradiation measurement.

6.2.2 Type Inversion

As noted in Section 2.5, the most remarkable radiation induced effect in n-type silicon devices is type inversion. Type inversion is caused by NIEL interactions resulting in deep defects, which tend to be p-like under bias. This effect was measured through C-V characteristics as shown for NDSU#1 in Figure 79 and UMKC#1 in Figure 80. With increasing fluence, the capacitance decreases due to the decline in the effective doping density, N_{eff}, from the creation of the p-like defects. For NDSU#1, after a total thermal (1 MeV neutron equivalent) fluence of 9.7×10^{13} (1.3×10^{13}) n cm^{-2}, the capacitance decreased by an average of approximately 17%. Similarly, UMKC#1 had a 24%

average capacitance decrease at a total thermal (1 MeV neutron equivalent) fluence of 7.5×10^{13} (1×10^{13}) n cm^{-2}. For comparison, NDSU#1 decreased by of approximately 12% at the same total fluence. This factor of two difference in the rate of damage is in approximate agreement with the factor of 2.5 expected based on the difference in nominal resistivity of the two diodes and (8) (see Table 9). However, as will be explained below, this direct comparison is limited due to the differences in the diodes and the method of irradiation.

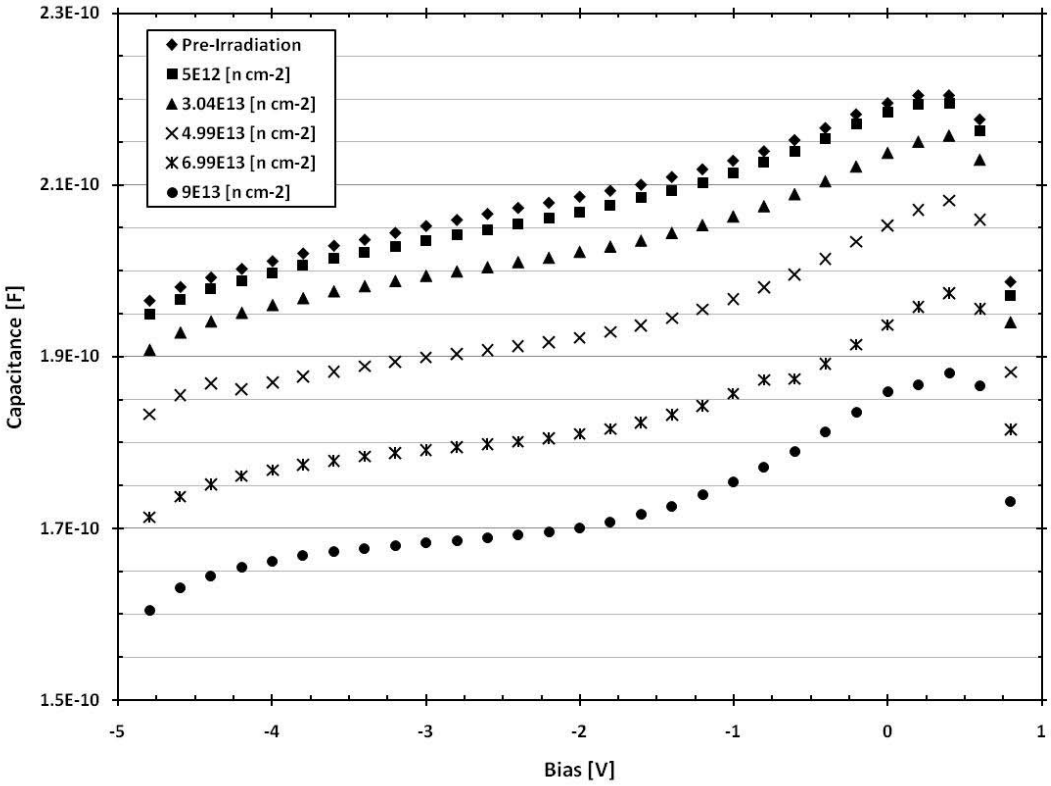

Figure 79. C-V characteristics as a function of total thermal neutron fluence for NDSU#1.

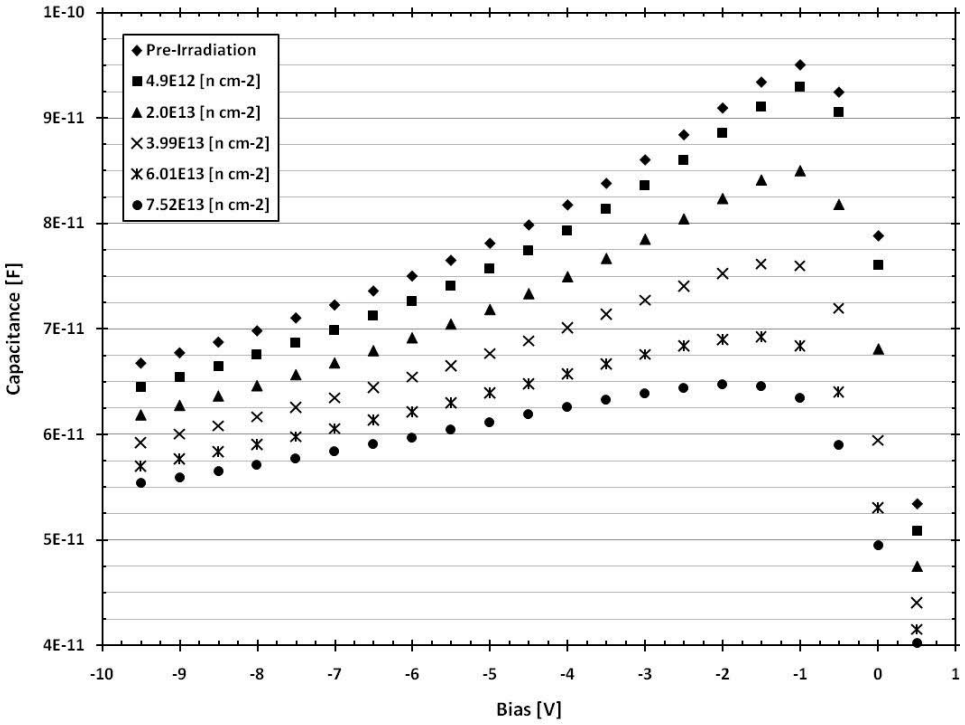

Figure 80. C-V characteristics as a function of total thermal neutron fluence for UMKC#1.

The root cause of the decrease in capacitance, a decrease in N_{eff}, can be calculated by

$$\frac{C^2}{C_0^2} = \frac{N_{eff}}{N_D}\left(1 - \frac{1}{\frac{N_{eff}}{N_A}}\right)\left(1 - \frac{1}{\frac{N_A}{N_{eff}}}\right), \tag{20}$$

where C_0 is the pre-irradiation capacitance [F]. N_{eff} is a particularly useful way to measure type inversion as was shown in Figure 28. Up until the point of inversion, N_{eff} will decrease as more p-like defects are created. At inversion, N_{eff} will reach a minimum. Finally, it will continue to increase while further

irradiation creates more p-like defects in what is now a p-type silicon substrate. As can be seen for NDSU#1 in Figure 81 and UMKC#1 in Figure 82, type inversion was not measured at the total fluence delivered to each.

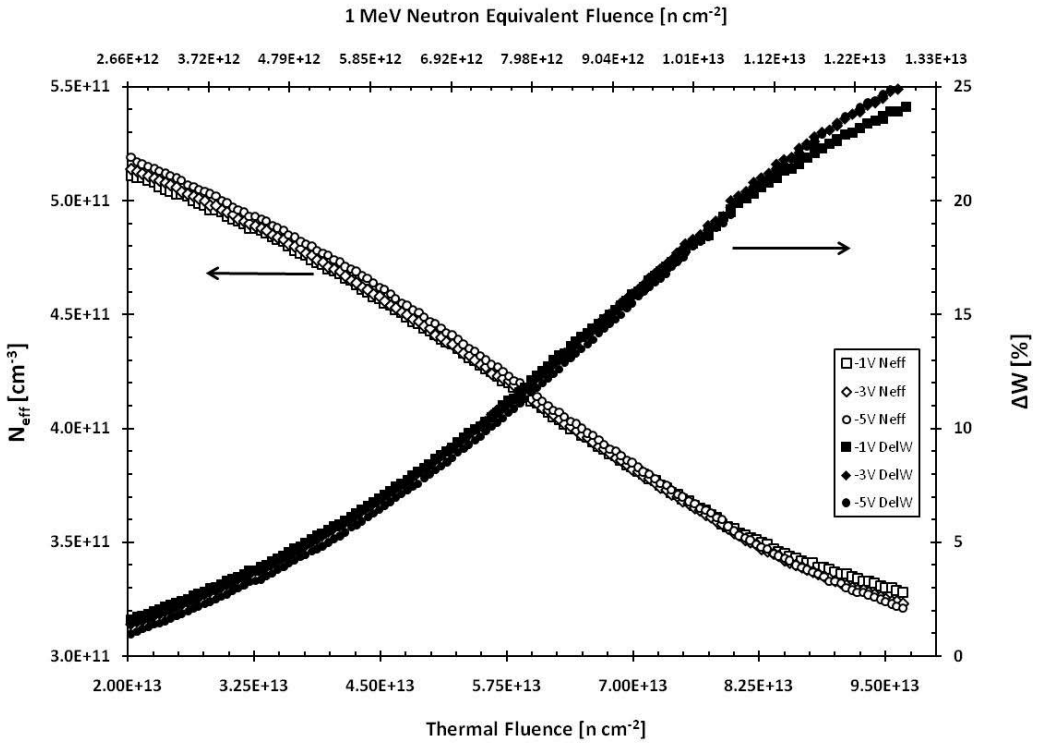

Figure 81. N_{eff} and ΔW for NDSU#1 as a function of total thermal and 1 MeV neutron equivalent fluence.

An interesting difference between the two is the apparent bias dependence in the UMKC#1 results. While one would not expect a bias dependence for a uniformly irradiated material, the use of thermal neutrons to induce boron capture products in the BC does not uniformly irradiate the entire silicon substrate. Instead, only the first several microns ($\square$ 5 μm) are

irradiated. In UMKC#1, the space-charge-region (SCR) is larger, due to the higher resistivity silicon thereby reducing the average N_{eff} in the SCR. This effect is magnified at higher biases where the SCR is further increased and the average N_{eff} is reduced. Finally, as shown in Figure 74, the capacitance density of NDSU#1 is much higher indicating a very small SCR. In this case, the SCR is limited to distances smaller than the range of the secondary capture products resulting in uniform irradiation of the SCR and a lack of bias dependence in the results.

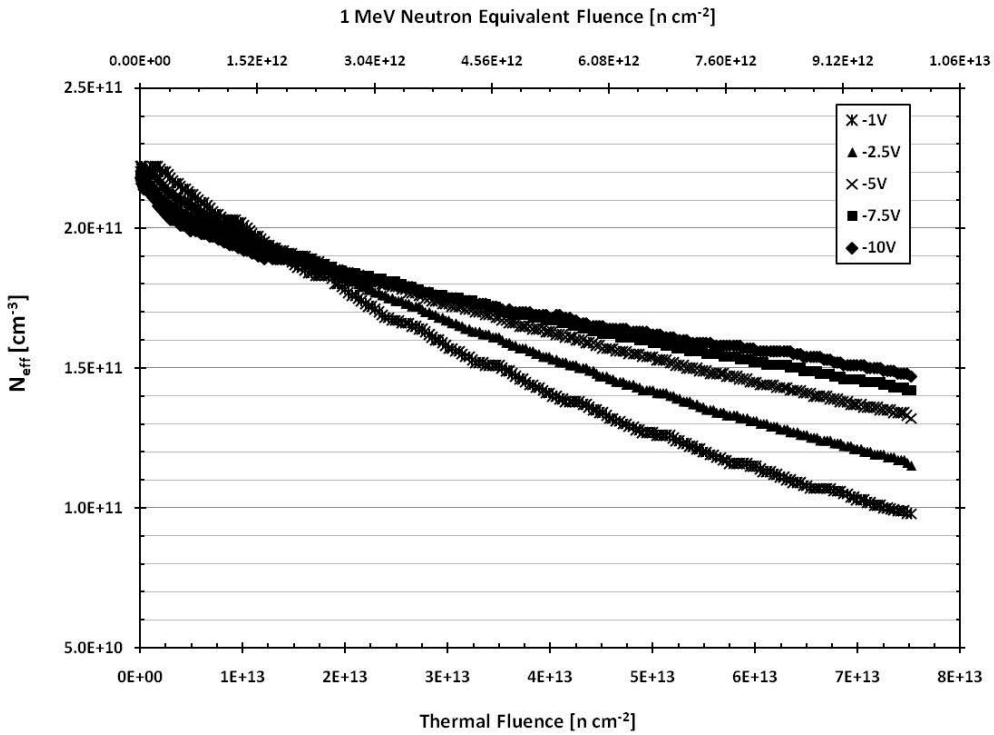

Figure 82. N_{eff} as a function of total thermal and 1 MeV neutron equivalent fluence for UMKC#1.

For these reasons, direct comparisons will fall short of the expected change based on the resistivity of the device alone. Nonetheless, the NDSU#1 N_{eff} decreased by 30% at a total thermal (1 MeV neutron equivalent) fluence of 7.5×10^{13} (1×10^{13}) n cm^{-2}. For UMKC#1 at -1V bias, the bias whose results would compare most favorably due to the smaller SCR, N_{eff} decreased by 57% at a total thermal (1 MeV neutron equivalent) fluence of 7.5×10^{13} (1×10^{13}) n cm^{-2}. This again gives a factor of approximately two difference between the diodes. For higher biases in UMKC#1, lower percent decreases were measured as shown in Figure 82.

The physical manifestation of changing N_{eff} is a change in the width of the SCR. The percent change in the width is calculated from (21).

$$\Box W(V) \Box \left(\frac{C_0(V)}{C(V)} \Box 1\right) \tag{21}$$

ΔW is plotted in Figure 81 for NDSU#1 and Figure 83 for UMKC#1. In comparison to the N_{eff} percent change, ΔW will be less owing to a constant SRC in BC. As previously discussed, the BC is taken as fully depleted (2 μm) at all biases. The bias dependence noted in UMKC#1 is attributable to the same root causes discussed for N_{eff}.

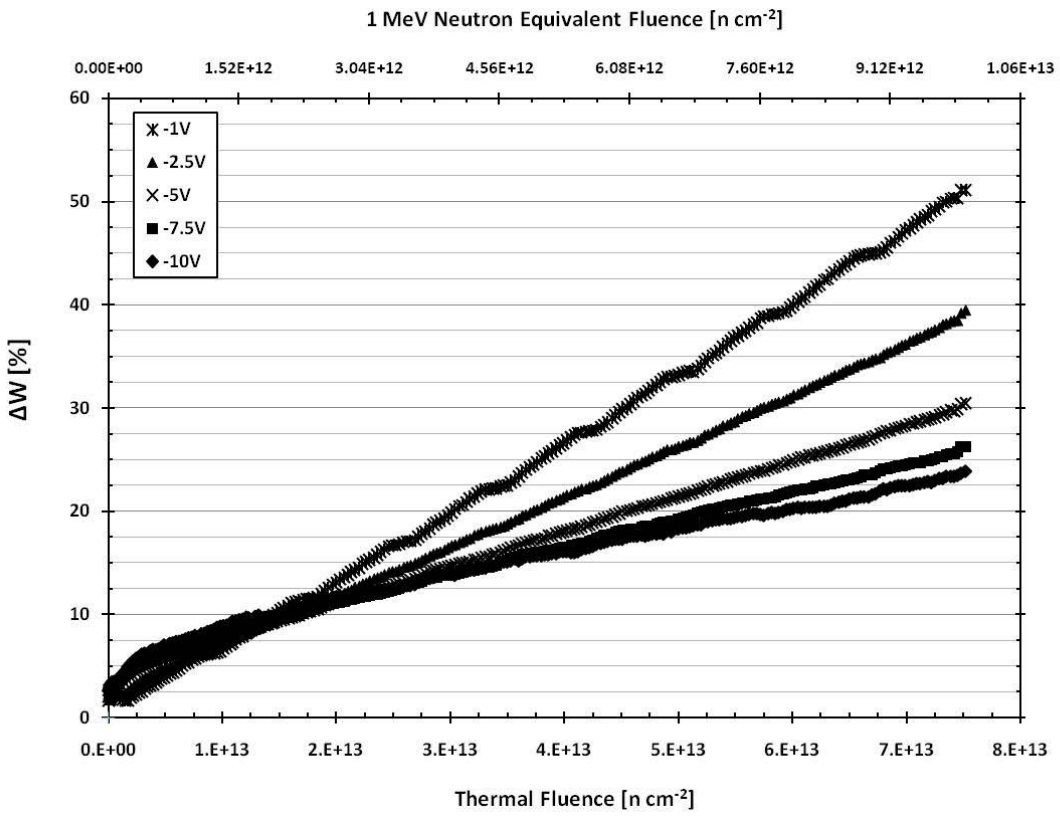

Figure 83. ΔW as a function of total thermal and 1 MeV neutron equivalent fluence for UMKC#1.

6.2.3 Irradiation Summary

While these irradiation results provide insight into defect damage to BC diodes, more questions remain unanswered such as:

1. **Can an experiment validate the procedure to determine a 1 MeV neutron fluence equivalent from thermal neutron capture as outlined in Appendix A.1?**

2. **Is the damage rate governed solely by the resistivity of the silicon substrate?**

3. What total fluence is required to achieve type inversion, and how does the device respond to this change?

4. What growth processes account for the differences in device performance and capacitance density observed when comparing each device?

Many of these questions are interrelated and exist due to the limitations imposed by the samples available. To answer question one, irradiation of at least two similar diodes, one in a fast neutron field and one in the thermal neutron field, is necessary. This will allow quantitative damage comparison from which to benchmark the conversion to a 1 MeV equivalent from the thermal neutron induced boron capture products.

The lack of knowledge regarding the accuracy of this conversion leads to questions two and three. NDSU#1 (UMKC#1) was irradiated to 130% (250%) of the predicted 1 MeV equivalent fluence necessary for type inversion. If the conversion were indeed accurate, this would mean that the devices are more radiation hard than expected from the resistivity of the silicon substrate. However, the multiple step conversion process and the lack of benchmarking for a new procedure call into question the accuracy of the calculation. Again, further irradiations are required to answer these questions.

Other than the increase in the leakage current, the other effects of NIEL damage in BC diodes up to type inversion are rather benign in terms of detector operation. However, type inversion could cause the device to quit functioning in

a manner suitable to serve as a detector, or it may merely require that the applied bias be inverted (i.e. forward is now reverse and vice versa). Measurements performed at fluences necessary for type inversion are necessary to quantify this effect. However, based on previous studies concerning the effects on diode performance from BC doping, it would appear that a combination of both is the likely outcome [15].

However, these irradiation results provide answers. First, BC diodes can withstand relatively high total thermal neutron fluences without type inversion, even with very high resistivity ($\square$ 8K Ω cm). The major limitation regarding device performance is the reduction in S/N that one would get from an increase in the leakage current (~340% at a thermal fluence of 9.7×10^{13} n cm^{-2}). From comparison of the NDSU#1 And UMKC#1 diodes, it appears that the increased leakage could be engineered to occur at higher total fluences by increasing the density of intrinsic defects in the BC and BC-Si interface. While this would raise the steady-state leakage current, it would allow for consistent device operation up to much higher fluence thresholds where required.

VII. Conclusions

Optimization of BC diodes was performed using a combination of nuclear physics transport models (GEANT and TRIM) as well as a semiconductor device models (TCAD). Through incorporation of these elements, the transient diode response to an idealized, simulated boron capture event was modeled. Utilizing this information, the S/N and charge collection, Q, expected from the capture event was determined for a range of controllable device growth parameters.

Additionally, BC diodes were irradiated in the OSURR thermal column to determine the effect of defect damage on heterojunction diodes of p-type B_5C on n-Si diodes. Two diodes grown using different processes on high resistivity silicon (8k and 20k Ω-cm) were irradiated to thermal neutron fluences of 9.7×10^{13} and 7.5×10^{13} n cm^{-2}, respectively. At these total fluence levels, increases in leakage current were observed, but type inversion was not achieved.

7.1 Summary of Optimization

A TCAD BC diode model was developed and benchmarked against two previously measured BC diodes. The model agreed with the experimentally determined leakage current to within 10% or better at biases up to -5V (-19V) for NDSU#1 (UNL#1). The capacitance was found to agree to within ~20% or better at biases up to -10V for UNL#1.

The primary limitations of this model are the lack of information regarding trap density, location, capture/emission cross-sections, and dynamics (owing to a corresponding absence of information on these in the literature) and the variability in the growth of BC diodes. This was compensated for by the use of effective parameters which allowed for the model to replicate current, capacitance, and charge collection time within reasonable agreement with experiment. However, no data existed from which to benchmark the magnitude of the charge collection. As such, results presented are normalized and can be scaled to experimentally determined full energy deposition values to establish expected charge collection at each operating condition.

Sensitivity studies indicated that the model is most sensitive in E_g and χ. While data exists on E_g for amorphous and crystalline BC, there is disagreement over the exact meaning of the different values. In the absence of information on the trap locations, densities, and capture/emission rates, an effective value of ~0.95 eV was used. However, no experimental information exists regarding χ. Measurement of these two parameters would greatly improve the accuracy of the model. As shown in Figure 56, the remaining parameters can vary by an order of magnitude or more while only resulting in a $\leq$ 10% change in the current. This enables these parameters to be less well defined while still achieving the model fidelity desired.

Optimization of a BC diode was performed to maximize detection characteristics using controllable device growth parameters. The metrics used were efficiency, S/N, and Q. Since Q is the more useful parameter quantifying the efficiency of charge transport in a device when a preamp is used, Q results were primarily presented. S/N results would be otherwise useful for diode operation in a direct current readout mode. All results presented are normalized owing to a lack of benchmark data for the collection efficiency of full energy deposition event in BC. In general, for silicon contact collection, the maximum charge was collected from a device with a silicon resistivity of ~10Ω cm and thin silicon substrates, while BC thickness and resistivity changes had minimal effects. For BC collection, the maximum charge was collected from a device with thinner BC layers, while changes to silicon resistivity, BC thickness, and BC resistivity had minimal effects. In both cases, higher bias operation led to higher charge collection.

Additionally, functional forms for each parameter at each contact were developed in the absence of a MDL criteria from an anticipated detection system. The functional forms are generally accurate within 10-15% at reverse biases less than -10 V and within the range of each parameter specified in Table 5. The resulting equations governing the efficiency and Q for each parameter are presented in (22).

$$
\begin{aligned}
Q_{\rho_{Si}}^{SCCon} &= \left(0.095\left|V_{app}\right|+0.05\right)\left(-0.017\rho_{Si}^{2}+0.2867\rho_{Si}-0.1843\right) && for\ \rho_{Si} \le 10\Omega - cm \\
Q_{\rho_{Si}}^{SCCon} &= 1.34\left|V_{app}\right|\rho_{Si}^{-0.96}+4.2\rho_{Si}^{-0.96} && for\ \rho_{Si} > 10\Omega - cm \\
Q_{t_{Si}}^{SiCon} &= \left(1.49 - 0.00315 t_{Si} + 2.44*10^{-6} t_{Si}^{2}\right)\left|V_{app}\right|^{0.7} \\
Q_{t_{BC}}^{SiCon} &= t_{BC}^{-0.18}\left(0.0093\left|V_{app}\right|+0.224\right) \\
Q_{bias}^{BCCon} &= 0.0464*\left|V_{app}\right|^{1.27} \\
Q_{t_{BC}}^{BCCon} &= \left(0.0072t_{BC}^{4}-0.11t_{BC}^{3}+0.616t_{BC}^{2}-1.55t_{BC}+1.64\right)\left(0.104\left|V_{app}\right|+0.039\right) \\
\varepsilon &= 3.47t_{BC}.
\end{aligned}
\qquad \textbf{(22)}
$$

Given an experimentally measured charge collection for a given set of conditions, the normalized functions presented can be scaled to estimate the charge collection from future diode growths and operating conditions. By scaling to experimentally determined charge collection results in this manner, the effect of the ion track orientation and simplifications used in the model development are minimized.

7.2 Summary of Radiation Effects

The device irradiation measurements fell short of the goal of determining an expected performance lifetime for a BC diode in neutron environments. Primarily, this was due to non-reproducibility in the diodes pre-irradiation characteristics. Although five devices were chosen, only NDSU#1 (8k Ω-cm Si) and UMKC#1 (20k Ω-cm Si) yielded diode-like characteristics and could be used for irradiation measurements.

After irradiation to a thermal neutron fluence of 9.7 $\times 10^{13}$ n cm^{-2}, the reverse leakage current increased an average of 340% in NDSU#1. This is likely due to NIEL damage creating tunneling and generation/recombination centers in the silicon which increased the bulk current. However, no statistically significant change was measured in the leakage current for UMKC#1. This is likely due to the higher initial current density indicating a higher defect density. Therefore, the additional introduction of radiation-induced defects is insignificant compared to the intrinsic defects.

C-V measurements indicate that type inversion did not occur at the thermal fluence expected from 1 MeV equivalent fluence conversion calculations. Due to the abridged irradiations, this method was not benchmarked to results obtained from fast neutrons and may be erroneous as the thermal results seem to indicate. Overall, capacitance in NDSU#1 decreased by ~17% on average after irradiation to a thermal neutron fluence of 9.7×10^{13} cm^2 resulting in a N_{eff} (W) decrease (increase) of ~42% (~24%). For UMKC#1 at -1V and a thermal neutron fluence of 7.5×10^{13} cm^2, the capacitance decreased ~24% resulting in a N_{eff} (W) decrease (increase) of ~57% (~51%). In UMKC#1, a bias dependence was measured in the capacitance change caused by the non-uniformity of the boron capture product distribution in the SCR.

Although incomplete, initial results indicate that the leakage current increase drives device performance degradation prior to type inversion. On the other hand, UMKC#1 results indicate that for high radiation environments, where efficiency can be traded for device hardness, engineering the growth process to include a high density of defects in the BC and Si-BC interface may provide a steady leakage current to a much higher total fluence. Since type inversion was not achieved, device performance past this point was not assessed. On the basis of observed results and doping studies previously discussed, it is likely to include a combination of increased leakage current and an inversion of the bands resulting in a reversal of bias operating regions (i.e. forward is reverse and vice versa). When coupling these and the optimization results (indicating lower resistivity silicon is preferential), it appears that BC diodes can be made reasonably hard to preclude lifetime issues in all but the most intense radiation environments.

7.3 Proposed Research Direction

Several areas of improvement have been discussed and all present opportunities for future research. Additionally, many of the device modeling techniques presented here have merit in other applications which couple radiation interactions to semiconductor devices. The following areas are proposed:

1. Refinement of the modeling methodology into a "process" for application to a variety of other device types,
2. Research into BC parameters of interest in electrical transport,
3. Specific refinement of the BC model to match ever-improving growth processes, and
4. Further irradiation studies to definitively quantify device lifetimes.

The potential exists to apply this modeling methodology to a variety of semiconductor devices designed to be detectors, nuclear-voltaic batteries, or exposed to a radiation field. To facilitate this use by a wide variety of researchers, a streamlined process would be highly beneficial. Currently, the process requires the use of multiple computing platforms and software. This requires a broad knowledge base that requires a significant "spin-up" time at the sacrifice of the research results. It would seem that a portion of this process, perhaps all, could be automated to an extent where a researcher has minimal time spent in structural overhead. For example, this overarching structure could be programmed to build the necessary input files and geometries to run a user-specified series of optimization or sensitivity studies on a user-specified device with user-specified materials and parameters (preferably in a streamlined format such as a GUI interface). Additionally, current simulations are limited to an idealized radiation energy deposition scenario. A useful "upgrade" would be a streamlined ability to simulate several different orientations and deposition

profiles. Admittedly, this would be a large undertaking and would, in some sense, sacrifice the level of intricacy currently available in the TCAD and GEANT models while making the user somewhat oblivious to the underlying processes.

As mentioned throughout, large gaps exist in the BC knowledge base. For a-B_5C:H_x, even less is available and/or contradicts much of the literature. This is a severe limitation in developing a model. Future research into electrical transport properties would greatly enhance the accuracy of this model while improving the understanding of this material. Additionally, refinement of the growth process and careful characterization of diodes suitable for benchmarks would benefit modeling, detector characterization, and radiation effects research.

Several limitations were presented for this model. Many of those issues would be addressed by the above research into material parameters and benchmarks. The model's fidelity and flexibility could be greatly enhanced by the incorporation of trap dynamics, better benchmarks, refinement of the fitted transport parameters (tied to better benchmarks), and finer grid spacing (more memory). Tying this model to a specific growth process would also increase the accuracy of the model as current devices vary by growth location and growth time.

Many questions were left unanswered regarding the radiation hardness of BC diodes as discussed in Section 6.2.3. With a better set of test diodes and irradiation environments, these answers could be answered thereby allowing for BC diode lifetime to be quantified. The thermal column is useful in attributing damage to boron capture products, but its low flux and uncertain 1 MeV neutron equivalency does not allow for development of a complete picture. The 7" column at the OSURR would provide a suitable environment to irradiate to a high total fluence in a fast neutron environment (if cadmium shielded). This allows damage attribution to the fast neutrons and direct 1 MeV neutron equivalent conversion from which to compare results to the thermal column and the wealth of information available on radiation damage in silicon. Additionally research into the effect that BC and BC-Si interface defect density (assuming this is a measurable, controllable parameter) has on radiation hardness and detection efficiency might yield a methodology to dramatically improve the hardness of these devices. As previously mentioned from the UMKC#1 results, it would appear that this presents opportunities for developing detectors that can withstand intense radiation fields with acceptable lifetimes and little significant device degradation.

Appendix A

A.1 Electron Affinity Calculations

The electron affinity was calculated consistent with the band diagram shown in Figure 17 [49]. The intrinsic carrier concentration is found by

$$n_i = \sqrt{N_c N_v}\, exp\left(-\frac{E_g}{2kT}\right) \quad (1)$$

where N_c is the effective conduction band density of states [cm^{-3}], N_v is the effective valence band density of states [cm^{-3}], E_g is the band gap energy [eV], and kT is the thermal energy [eV] [86]. Using the values in Table 7, a value of 2.85×10^{11} cm^{-3} was obtained. Using this value, and the silicon values in Table 7, the Fermi level is given by

$$\phi_{n/p} = \frac{kT}{q} ln\left(\frac{N_{D/A}}{n_i}\right), \quad (2)$$

where $N_{D/A}$ is the donor/acceptor doping concentration [cm^{-3}] [86]. The resulting values are shown in Table 7. The electron affinity can then be found from

$$\chi_p = V_{bi} - \chi_n - E_{F,p}^{VB} - E_{F,n}^{CB} - E_{g,p}, \quad (3)$$

where $\chi_{p/n}$ is the electron affinity of the p-/n-type semiconductor [eV], $E_{F,p}^{VB}$ is the Fermi energy of the p-type semiconductor referenced to the valence band [eV], $E_{F,n}^{CB}$ is the Fermi energy of the n-type semiconductor referenced to the

conduction band [eV], and $E_{g,p}$ is the p-type semiconductor band gap [eV] [49]. A resulting value of 4.58 eV was calculated and is included in Table 7.

A.2 Thermal flux to 1 MeV neutron equivalent Calculations

Using GEANT, values were obtained relating the average energy and rate of He and Li ions entering the silicon region of the diode. The values obtained for 100meV neutrons (taken as the average of the cadmium difference energy spectrum) are shown in Table 12.

Table 12. GEANT and subsequent NIEL results for boron capture products that reach a n-type silicon layer for a planar source of 100 meV average neutrons.

Parameter	Value
α Efficiency	0.16%
α E_{avg}	0.8 [MeV]
α NIEL	2500 [keV cm^2 g^{-1}]
Li Efficiency	0.06%
Li E_{avg}	0.45 [MeV]
Li NIEL	9640 [keV cm^2 g^{-1}]

Using Figure 84 and the TRIM obtained ratio of Li/He damage of 2.41, NIEL values were determined and are presented in Table 12. These values were then used to determine the thermal fluence required to reach the 1 MeV equivalent fluence calculated by (8) using

$$\phi_{Max}^{1MeV} = \phi_{\max}^{Therm}\left(\frac{NIEL_{Li} * R_{Li} + NIEL_{He} * R_{He}}{NIEL_{n}^{1MeV}}\right), \tag{4}$$

where NIEL is the non-ionizing energy loss for each particle [kev cm^2 g^{-1}] and R is the rate of ion deposition in silicon per incident neutron.

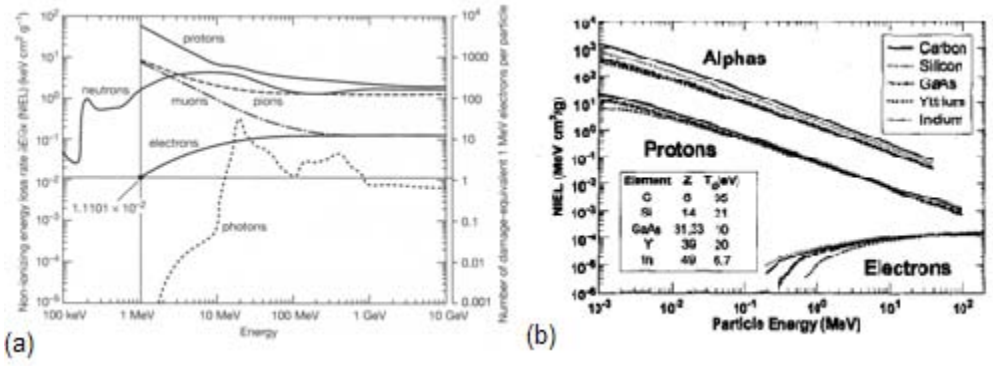

Figure 84. NIEL charts where (a) provided values for neutrons [61] and (b) provided information for Li (after TRIM correction) and He ions [87].

From (8), a total 1 MeV fluence of ~ 4×10^{12} n cm^{-2} is needed to achieve type inversion in the 20k Ω-cm silicon layer of the B_5C diode. Then by applying (4), an approximate thermal flux of 3.5×10^{13} n cm^{-2} is needed to obtain type inversion.

Appendix B

This appendix includes portions of the input code for the various software programs used in this research. The symbols *** indicate where segments have been removed. The full code developed is included in supporting documentation accompanying this document.**

B.1 GEANT Input Files

B.1.1 Detector Construction

```
*********************************************************************************
  //=================
  //Define Materials
  //=================
  G4NistManager* man = G4NistManager::Instance();
  G4double a;  // atomic mass
  G4double z;  // atomic number
  G4double density;
  G4int nel;

  //Air
  G4Element* N = new G4Element("Nitogen", "N", z=7., a=14.01*g/mole);
  G4Element* O = new G4Element("Oxygen", "O", z=8., a = 16.00*g/mole);
  G4Material* Air = new G4Material("Air", density=1.29*mg/cm3, nel=2);
  Air->AddElement(N, 70*perCent);
  Air->AddElement(O, 30*perCent);

  //Silicon
  G4Element* Si = new G4Element("Silicon", "Si", z=14., a=28.0855*g/mole);
  G4Material* Silicon = new G4Material("Silicon", density= 2.33*g/cm3, nel=1);
  Silicon->AddElement(Si, 100*perCent);

  //Boron Carbide
  G4Isotope* B10 = new G4Isotope("Boron10", z=5, 10, a=10*g/mole);
  G4Element* B = new G4Element("Boron", "Boron", 1);
  B->AddIsotope(B10,1.0);
  G4Element* C = new G4Element("Carbon", "C", z=6, a=12*g/mole);
  G4Element* H = new G4Element("Hydrogen", "H", z=1, a=1.008*g/mole);
  G4Material* BoronCarbide = new G4Material("BoronCarbide", density= 2.52*g/cm3, nel=3);
  BoronCarbide->AddElement(B, 41.67*perCent);
  BoronCarbide->AddElement(C, 8.33*perCent);
  BoronCarbide->AddElement(H, 50*perCent);

*********************************************************************************
  //===============
  //Define Volumes
  //===============
  //Experimental Hall (world volume)
  //defines volume in which all materials for the experiment will be placed
  //particle gun shoots along z axis
  fWorldLength= 5*cm;
  G4double expHall_x = 5*cm;
  G4double expHall_y = 5*cm;
  G4double expHall_z = 5*cm;
```

```
  G4Box* experimentalHall_box = new G4Box("expHall_box",expHall_x,expHall_y,expHall_z);
  experimentalHall_log = new G4LogicalVolume(experimentalHall_box,Air,"expHall_log");
  experimentalHall_phys = new
G4PVPlacement(0,G4ThreeVector(0,0,0),experimentalHall_log,"expHall",0,false,0);

  //------------------------------
  // Boroncarbide: p-type layer
  //------------------------------

  G4double BC_x = 0.1000*cm;
  G4double BC_y = 0.1000*cm;
  G4double BC_z = 0.0002500*cm;
  G4double BC_start_x = 0*cm;
  G4double BC_start_y = 0*cm;
  G4double BC_start_z = 0.0002500*cm;
  G4Box* pLayer_box = new G4Box("pLay_box", BC_x, BC_y, BC_z);
  pLayer_log = new G4LogicalVolume(pLayer_box,BoronCarbide,"pLay_log");
  pLayer_phys = new G4PVPlacement(0, G4ThreeVector(BC_start_x, BC_start_y, BC_start_z),
pLayer_log, "pLay_box",experimentalHall_log,false,0);

  //------------------------------
  // Silicon: n-type layer
  //------------------------------

  G4double Si_x = 0.1000*cm;
  G4double Si_y = 0.1000*cm;
  G4double Si_z = 0.02625*cm;
  G4double Si_start_x = 0*cm;
  G4double Si_start_y = 0*cm;
  G4double Si_start_z = -0.02625*cm;
  G4Box* nLayer_box = new G4Box("nLay_box", Si_x, Si_y, Si_z);
  nLayer_log = new G4LogicalVolume(nLayer_box,Silicon,"nLay_log");
  nLayer_phys = new G4PVPlacement(0, G4ThreeVector(Si_start_x, Si_start_y, Si_start_z),
nLayer_log, "nLay_box",experimentalHall_log,false,0);

  //============================
  // Define Sensitive Detector
  //============================
  G4SDManager* SensitiveDetectorMan = G4SDManager::GetSDMpointer();
  G4String ROname = "/BoronCarbide/readout";
  BoronCarbideSensitiveDet* ReadOut = new BoronCarbideSensitiveDet(ROname);
  SensitiveDetectorMan->AddNewDetector(ReadOut);
  nLayer_log->SetSensitiveDetector(ReadOut);
  pLayer_log->SetSensitiveDetector(ReadOut);
*****************************************************************************************
```

B.1.2 Physics List

```
*****************************************************************************************
// gamma
#include "G4LowEnergyRayleigh.hh"
#include "G4LowEnergyPhotoElectric.hh"
#include "G4LowEnergyCompton.hh"
#include "G4LowEnergyGammaConversion.hh"
// e-
#include "G4MultipleScattering.hh"
#include "G4LowEnergyIonisation.hh"
#include "G4LowEnergyBremsstrahlung.hh"
// e+
#include "G4eIonisation.hh"
#include "G4eBremsstrahlung.hh"
#include "G4eplusAnnihilation.hh"
// neutron
#include "G4HadronElasticProcess.hh"
#include "G4LElastic.hh"
#include "G4NeutronHPElastic.hh"
#include "G4NeutronHPElasticData.hh"
#include "G4NeutronHPThermalScattering.hh"
```

```
#include "G4NeutronHPThermalScatteringData.hh"
#include "G4NeutronInelasticProcess.hh"
#include "G4LENeutronInelastic.hh"
#include "G4NeutronHPInelastic.hh"
#include "G4NeutronHPInelasticData.hh"
#include "G4HadronCaptureProcess.hh"
#include "G4LCapture.hh"
#include "G4NeutronHPCapture.hh"
#include "G4NeutronHPCaptureData.hh"
#include "G4HadronFissionProcess.hh"
#include "G4LFission.hh"
#include "G4NeutronHPFission.hh"
// hadronic processes:
#include "G4hIonisation.hh"
#include "G4hLowEnergyIonisation.hh"
#include "G4StepLimiter.hh"
// construct general
#include "G4Decay.hh"
#include "G4RadioactiveDecay.hh"

*******************************************************************************************
      //============================
      // Neutron Elastic Scattering
      //============================
      G4HadronElasticProcess* theNeutronElasticProcess = new
G4HadronElasticProcess("HadElas_neutron");

      //cross section data
      G4NeutronHPElasticData* theHPElasticData = new G4NeutronHPElasticData();  //(4eV-
20MeV)
      theNeutronElasticProcess->AddDataSet(theHPElasticData);
      G4NeutronHPThermalScatteringData* theHPThermalScatteringData = new
G4NeutronHPThermalScatteringData(); //(<4eV)
      theNeutronElasticProcess->AddDataSet(theHPThermalScatteringData);

      //models
      G4LElastic* theElasticModel = new G4LElastic();
      theElasticModel->SetMinEnergy(19*MeV);
      theNeutronElasticProcess->RegisterMe(theElasticModel);
      G4NeutronHPElastic* theNeutronElasticModel = new G4NeutronHPElastic();
      theNeutronElasticModel->SetMaxEnergy(19.0*MeV);
      theNeutronElasticModel->SetMinEnergy(4.0*eV);
      theNeutronElasticProcess->RegisterMe(theNeutronElasticModel);
      G4NeutronHPThermalScattering* theNeutronThermalElasticModel = new
G4NeutronHPThermalScattering();
      theNeutronThermalElasticModel->SetMaxEnergy(4.0*eV);
      theNeutronElasticProcess->RegisterMe(theNeutronThermalElasticModel);

      //apply to process manager
      pmanager->AddDiscreteProcess(theNeutronElasticProcess);

      //============================
      // Neutron Inelastic Scattering
      //============================
      G4NeutronInelasticProcess* theInelasticProcess = new
G4NeutronInelasticProcess("NeutronInelas");

      //cross section data
      G4NeutronHPInelasticData * theNeutronData1 = new G4NeutronHPInelasticData();
      theInelasticProcess->AddDataSet(theNeutronData1);

      //models
      G4LENeutronInelastic* theInelasticModel = new G4LENeutronInelastic();
      theInelasticModel->SetMinEnergy(19*MeV);
      theInelasticProcess->RegisterMe(theInelasticModel);
      G4NeutronHPInelastic * theLENeutronInelasticModel = new G4NeutronHPInelastic();
      theInelasticProcess->RegisterMe(theLENeutronInelasticModel);

      //apply to process manager
```

```
      pmanager->AddDiscreteProcess(theInelasticProcess);

      //=================
      // Neutron Capture
      //=================
      G4HadronCaptureProcess* theCaptureProcess = new
G4HadronCaptureProcess("HadCapt_neutron");

      //cross section data
      G4NeutronHPCaptureData * theNeutronData3 = new G4NeutronHPCaptureData();
      theCaptureProcess->AddDataSet(theNeutronData3);

      //models
      G4LCapture* theCaptureModel = new G4LCapture();
      theCaptureModel->SetMinEnergy(19*MeV);
      theCaptureProcess->RegisterMe(theCaptureModel);
      G4NeutronHPCapture* theLENeutronCaptureModel = new G4NeutronHPCapture();
      theCaptureModel->SetMaxEnergy(19*MeV);
      theCaptureProcess->RegisterMe(theLENeutronCaptureModel);

      // apply to process manager
      pmanager->AddDiscreteProcess(theCaptureProcess);

*****************************************************************************************
  G4cout<<"SetCuts";

  // The production threshold is fixed to 0.1 mm for all the particles
  // Secondary particles with a range bigger than 0.1 mm
  // are generated; otherwise their energy is considered deposited locally
  defaultCutValue = 0.001 * mm;

  const G4double cutForGamma = defaultCutValue;
  const G4double cutForElectron = defaultCutValue;
  const G4double cutForPositron = defaultCutValue;

  SetCutValue(cutForGamma, "gamma");
  SetCutValue(cutForElectron, "e-");
  SetCutValue(cutForPositron, "e+");

  // the low limit for electrons should never be less than 250eV because the LE physics
processes
  // are only defined down to 250eV
  G4double lowLimit = 500.0 * eV;
  G4double highLimit = 100. * GeV;
  G4ProductionCutsTable::GetProductionCutsTable()->SetEnergyRange(lowLimit, highLimit);

  if (verboseLevel>0)
    DumpCutValuesTable();
}
```

B.1.3 Primary Generator Action

```
*****************************************************************************************
BoronCarbidePrimaryGeneratorAction::BoronCarbidePrimaryGeneratorAction(BoronCarbideDetect
orConstruction* myDC)
  :myDetector(myDC)
{
  G4int n_particle = 1;
  particleGun = new G4ParticleGun(n_particle);

  G4ParticleTable* particleTable = G4ParticleTable::GetParticleTable();
  G4ParticleDefinition* particle = particleTable->FindParticle("neutron");

  particleGun->SetParticleDefinition(particle);
  particleGun->SetParticleMomentumDirection(G4ThreeVector(0.,0.,-1.));
}
```

```
BoronCarbidePrimaryGeneratorAction::~BoronCarbidePrimaryGeneratorAction()
{
  delete particleGun;
}

void BoronCarbidePrimaryGeneratorAction::GeneratePrimaries(G4Event* anEvent)
{
  // choose particle energy randomly from input distribution
  if (readInputEnergySpectrum) {
       G4String filename =
"/Users/Abby/Documents/geant4/AFIT/BoronCarbide/nEnergy/nEnergyProb.txt";
       std::ifstream file(filename, std::ios::in);
       std::filebuf* lsdp = file.rdbuf();

       if (! (lsdp->is_open()) )
         {
           G4String excep = "BoronCarbidePrimaryGenerator - data file not found: " +
filename;
           G4Exception(excep);
         }

       //initialize array
       //max limit on the nbins the input probability distribution can have is 1000
       G4double sampleArray[1000];
       for (G4int j=0; j<1000; j++)
           sampleArray[j] = 0;

       G4int counter = 0;
       while (!file.eof())
         {
           // protection against a blank line at the end of the file
           if (counter==_nBins) break;
           // The file is organized in columns of energy and probability
           file >> energy_bin >> prob;
           sampleArray[counter] = prob;
           counter++;
         }

       G4RandGeneralTmp randGeneral(sampleArray, _nBins);
       G4double random = randGeneral.shoot();
       energy = _eMin*MeV + (_eMax*MeV - _eMin*MeV) * random;

       //G4cout<<"energy = "<<energy<<", random = "<<random<<G4endl;
  }
  else   {
    energy = 0.025*eV;  //define the energy of the particle to be shot
  }

  particleGun->SetParticleEnergy(energy);

  //G4double position = 0.5*(myDetector->GetDetectorFullLength());
  particleGun->SetParticlePosition(G4ThreeVector(0.*cm,0.*cm,0.0006*cm));
  particleGun->GeneratePrimaryVertex(anEvent);

}
```

B.1.4 Sensitive Detector

```
*****************************************************************************************
G4bool BoronCarbideSensitiveDet::ProcessHits(G4Step* aStep,G4TouchableHistory*)
{
  G4ParticleDefinition* particleType = aStep->GetTrack()->GetDefinition();

  edep = aStep->GetTotalEnergyDeposit();
  deltaE = aStep->GetDeltaEnergy();
  trackid = aStep->GetTrack()->GetTrackID();
  parentid = aStep->GetTrack()->GetParentID();
```

```
  particlename = particleType->GetParticleName();
  geantid = particleType->GetPDGEncoding();
  trackenergy = aStep->GetTrack()->GetKineticEnergy();
  vertexKE = aStep->GetTrack()->GetVertexKineticEnergy();
  if (writeTrackFile) writeTheTrackFile();

  if (aStep->GetTrack()->GetCreatorProcess()) {
    const G4VProcess* trackProcess = aStep->GetTrack()->GetCreatorProcess();
    const G4String processName = trackProcess->GetProcessName();
    //if (geantid==11)
    //G4cout<<"TrackID: "<<trackid<<", parentid = "<<parentid<<", particlename =
"<<particlename<<", geantid = "<<geantid<<", GetTotalEnergyDeposit = "<<edep<<",
GetDeltaEnergy = "<<deltaE<<", TrackEnergy = "<<trackenergy<<", VertexKE =
"<<vertexKE<<", CreatorProcess = "<<processName<<G4endl;
  }
  //else
  //G4cout<<"TrackID: "<<trackid<<", parentid = "<<parentid<<", particlename =
"<<particlename<<", geantid = "<<geantid<<", GetTotalEnergyDeposit = "<<edep<<",
GetDeltaEnergy = "<<deltaE<<", TrackEnergy = "<<trackenergy<<", VertexKE =
"<<vertexKE<<G4endl;

  //if no energy deposited in the sensitive detector
  //do not add entry to hit to hitCollection
  if(edep==0.) return false;

  BoronCarbideHit* newHit = new BoronCarbideHit();
  newHit->SetTrackID        (trackid);
  newHit->SetParentID       (parentid);
  newHit->SetEdep           (edep);
  newHit->SetPos            (aStep->GetPostStepPoint()->GetPosition());
  newHit->SetMomentum       (aStep->GetTrack()->GetMomentum());
  newHit->SetParticleName   (particlename);
  newHit->SetParticleEtot   (aStep->GetPreStepPoint()->GetTotalEnergy());
  newHit->SetParticleDeltaE (deltaE);
  newHit->SetParticleKE     (aStep->GetPreStepPoint()->GetKineticEnergy());
  newHit->SetTrackKE        (trackenergy);
  newHit->SetTime           (aStep->GetTrack()->GetGlobalTime());
  newHit->SetTrackLength    (aStep->GetTrack()->GetTrackLength());
  newHit->SetGeantID        (geantid);
  newHit->SetVertexPosition (aStep->GetTrack()->GetVertexPosition());
  newHit->SetVertexKE       (vertexKE);

  HitID = hitCollection->insert( newHit );
  return true;
}

void BoronCarbideSensitiveDet::EndOfEvent(G4HCofThisEvent*HCE)
{
  G4String HCname = collectionName[0];

  static G4int HCID = -1;
  if(HCID<0)
    HCID = G4SDManager::GetSDMpointer()->GetCollectionID(HCname);
  HCE->AddHitsCollection(HCID,hitCollection);


  //if (verboseLevel>0) {
  G4int NbHits = hitCollection->entries();
  G4cout << "\n-------->Hits Collection: in this event they are " << NbHits
         << " hits in the sensitive detector: " << G4endl;
  for (G4int i=0;i<NbHits;i++) (*hitCollection)[i]->Print();
  //}

  //last line of event needs to be distinguishable
  if (writeTrackFile) {
    G4String filename="boroncarbide_track.out";
    ofstream evfile(filename, ios::app);
    evfile <<"-1 -1 -1 -1 -1 -1 -1"<<G4endl;
    evfile.close();
```

```
  }
}

void BoronCarbideSensitiveDet::writeTheTrackFile(void)
{
  G4String filename="boroncarbide_track.out";
  ofstream evfile(filename, ios::app);

  evfile <<trackid<<" "
         <<parentid<<" "
         <<particlename << " "
         <<geantid<< " "
          <<vertexKE/MeV<< " "
         <<deltaE/MeV << " "
         <<trackenergy/MeV
         <<G4endl;

  evfile.close();
}
```

B.2 TCAD Input Files

B.2.1 Boron Carbide Parameter File

```
Epsilon
{ *  Ratio of the permittivities of material and vacuum

  * epsilon() = epsilon
      epsilon = 8     # [1]
}
*******************************************************************************************
Bandgap
{ * Eg = Eg0 + dEg0 + alpha Tpar^2 / (beta + Tpar) - alpha T^2 / (beta + T)
  * dEg0(<bgn_model_name>) is a band gap correction term.  It is used together with
  * an appropriate BGN model, if this BGN model is chosen in Physics section
  * Parameter 'Tpar' specifies the value of lattice
  * temperature, at which parameters below are defined
  * Chi0 is electron affinity.
      Chi0    = 4.58  # [eV]
      Bgn2Chi = 0.0   # [1]
      Eg0     = 0.95  # [eV]
      dEg0(Bennett)  = 0.0000e+00   # [eV]
      dEg0(Slotboom) = 0.0000e+00   # [eV]
      dEg0(OldSlotboom)      = 0.0000e+00   # [eV]
      dEg0(delAlamo) = 0.0000e+00   # [eV]
      alpha   = 0.0000e+00   # [eV K^-1]
      beta    = 0.0000e+00   # [K]
      Tpar    = 0.0000e+00   # [K]
}

*******************************************************************************************
eDOSMass
{
  * For effective mass specificatition Formula1 (me approximation):
  * or Formula2 (Nc300) can be used :
      Formula = 2     # [1]
  * Formula1:
  * me/m0 = [ (6 * mt)^2 *  ml ]^(1/3) + mm
  * mt = a[Eg(0)/Eg(T)]
  * Nc(T) = 2(2pi*kB/h_Planck^2*me*T)^3/2 = 2.540e19 ((me/m0)*(T/300))^3/2
  * Formula2:
  * me/m0 = (Nc300/2.540e19)^2/3
  * Nc(T) = Nc300 * (T/300)^3/2
      Nc300   = 1e+19 # [cm-3]
      a       = 0.0625       # [1]
      ml      = 1.5   # [1]
```

```
        mm      = 1.0000e+00   # [1]
}

hDOSMass
{
  * For effective mass specificatition Formula1 (mh approximation):
  * or Formula2 (Nv300) can be used :
        Formula = 2     # [1]
  * Formula1:
  * mh =  m0*{[(a+bT+cT^2+dT^3+eT^4)/(1+fT+gT^2+hT^3+iT^4)]^(2/3) + mm}
  * Nv(T) = 2(2pi*kB/h_Planck^2*mh*T)^3/2 = 2.540e19 ((mh/m0)*(T/300))^3/2

  * Formula2:
  * mh/m0 = (Nv300/2.540e19)^2/3
  * Nv(T) = Nv300 * (T/300)^3/2
        Nv300   = 1e+19 # [cm-3]
        a       = 1     # [1]
        b       = 0     # [K^-1]
        c       = 0     # [K^-2]
        d       = 0     # [K^-3]
        e       = 0     # [K^-4]
        f       = 0     # [K^-1]
        g       = 0     # [K^-2]
        h       = 0     # [K^-3]
        i       = 0     # [K^-4]
        mm      = 1     # [1]
}

ConstantMobility:
{ * mu_const = mumax (T/T0)^(-Exponent)
        mumax   = 0.001,        0.00075 # [cm^2/(Vs)]
        Exponent        = 3 ,   3       # [1]
        mutunnel        = 0.05 ,        0.05    # [cm^2/(Vs)]
}

*******************************************************************************************
HeavyIon("LiInBC"){
  }

HeavyIon("HeInBC"){
  }
```

B.2.2 Command File

```
Device Diode{
 File{
  *input files
  Grid = "geom_UMKC_msh.grd"
  Doping = "geom_UMKC_msh.dat"
  Parameter = "Models.par"
 }

 Electrode {
  { Name = "BCCon" Voltage = 0.0 }
  { Name = "SCon" Voltage = 0.0 }
 }

 Physics {
  Recombination(
   SRH(DopingDep
     Tunneling(Hurkx)
     )
   Auger(WithGeneration)
   TrapAssistedAuger
   Band2Band
   Radiative
   )
```

```
  Mobility(DopingDep Enormal CarrierCarrierScattering)
  EffectiveIntrinisicDensity (BandgapNarrowing (BennettWilson))
 }

 Physics (RegionInterface = "Silicon/BoronCarbide") {
  Thermionic
  HeteroInterface
  Recombination (SurfaceSRH)
 }
}

Math {
 Extrapolate
 RelErrControl
 Traps(Damping=10)
 RecBoxIntegr(1e-2 10 1000)
 Transient=BE
 Number_of_Threads = 4
 Method=Pardiso
 RHSmin=1e-20
 Denslowlimit=1e-10
 Extrapolate
 Derivatives
 Iterations = 30
}

File{
 *Output Files:
  Plot = "UMKC_IV_des.tdr"
  Current = "UMKC_IV_des.plt"
  Output = "UMKC_IV_des.log"
}

System{
  Diode trans (BCCon=B SCon=S)
  Vsource_pset vB (B 0) {dc=0}
*  Vsource_pset vS (S 0) {dc=0}
  Vsource_pset to_ground (S 0) {dc=0}
}

Plot {
 edensity hdensity eCurrent hCurrent Potential SpaceCharge
 ElectricField eMobility hMobility eVelocity hVelocity
 Doping DonorConcentration AcceptorConcentration HeavyIonChargeDensity
 eTrappedCharge hTrappedCharge eGapStatesRecombination, SRHRecombination
 hGapStatesRecombination, SpaceCharge, eQuasiFermi, hQuasiFermi CDL1 CDL2 CDL3
 eBarrierTunneling hBarrierTunneling RadiativeRecombination, SurfaceRecombination
 QuasiFermiPotential HeavyIonCharge HeavyIonChargeDensity
}

**IV TRACE
Solve {
 #-initial solution:
 Poisson
 Coupled { Poisson Electron Hole }
* #-ramp bias:
 Quasistationary ( MaxStep= 1 InitialStep=5e-3
 Goal { Parameter=vB.dc Voltage = -1 } )
{ Coupled { Poisson Electron Hole } }
Quasistationary ( MaxStep= 0.1
 Goal { Parameter=vB.dc Voltage = -2 } )
{ Coupled { Poisson Electron Hole } }
 Quasistationary ( MaxStep= 0.0125
 Goal { Parameter=vB.dc Voltage = -10 } )
{ Coupled { Poisson Electron Hole } }
}
```

B.3 KULT 4200 Automation Script

```
/*** Variables to send and receive GPIB commands ***/
char command_string[100];
char response_string[100000];
int max_size = 100000;
int rcv_size;

/*** Variables used in IV curves ***/
double VInow  = 0.0;
double IVnow  = 0.0;
double VIDataArray[20][1000] = {0.};
double VIAbsDataArray[20][1000] = {0.};
double VIAvgDataArray[3][1000] = {0.};       // [I,AbsI]
double VIStdDataArray[3][1000] = {0.};       // [I,AbsI]
double VISourced[1000] = {0.};
int    NumVIMeas;
double N;

/*** Variables used in CV curves ***/
double CVnow  = 0.0;
double VCnow  = 0.0;
double CVSourced[1000];
double CVDataArray [1000];
double GVDataArray [1000];
char   CapacitanceString[20];
char   ConductanceString[20];
char   VoltageString[20];
char   NumReadings[4];
int    inc;

/*** Variables used for Timing ***/
time_t TIMEnow;
char   *TIMEstring[30];
time_t Timer;
long int TimerNow;
long int TimerThen;
long int TheBeginningOfTime;
long int TheGrandClock;
long int TheGrandClockStep;
long int AbsoluteTime;
long int TimeHack;
long int LoopTime;

/*** Variables used for FILE Control ***/
FILE *DataFileText[10];
char *WritingMode[4];
char *DataFilePath[10][70];

/*** Variables used for Code Flow Control ***/
char FeedBackString[80];
int  CodeWord = 1111;
int ASimpleCounter = 0;
int VISimpleCounter = 0;
int CVSimpleCounter = 0;
int InfiniteLoopCatch = 0;
int i;
int j;
int k;
int m;
int f;
int s;
int NumDiode = 0;
int CharNumber;
char SizeOfString[100];
sprintf(FeedBackString,"Built all Variables");
PostDataString("Feedback",FeedBackString);
```

```
/*** Intialize Output ***/
for (i = 0; i < 20; i++) {
    CapacitanceString[i]=0;
    ConductanceString[i]=0;
    VoltageString[i]=0;
}
sprintf(FeedBackString,"Initialized Output");
PostDataString("Feedback",FeedBackString);

/*** Prepare 707 for Experimentation ***/
sprintf(command_string,"*RSTX");
kibsnd(GPIB_Address_707,IGNORE_PARAM,GPIBTIMO,strlen(command_string),command_string);
sprintf(FeedBackString,"Keithley 707 initialized");
PostDataString("Feedback",FeedBackString);

/*** Prepare 590 for Experimentation ***/
sprintf(command_string,"*RSTX");
kibsnd(GPIB_Address_590,IGNORE_PARAM,GPIBTIMO,strlen(command_string),command_string);
sprintf(command_string,"F1R0X");
kibsnd(GPIB_Address_590,IGNORE_PARAM,GPIBTIMO,strlen(command_string),command_string);
sprintf(command_string,"P1N0X");
kibsnd(GPIB_Address_590,IGNORE_PARAM,GPIBTIMO,strlen(command_string),command_string);
sprintf(command_string,"G4O0,0S4X");
kibsnd(GPIB_Address_590,IGNORE_PARAM,GPIBTIMO,strlen(command_string),command_string);
sprintf(FeedBackString,"Keithley 590 initialized");
PostDataString("Feedback",FeedBackString);

sprintf(FeedBackString,"Number of Diodes: %d",NumberOfDiodes);
PostDataString("Feedback",FeedBackString);

/*** Build File ***/
for (NumDiode = 1; NumDiode <= NumberOfDiodes; NumDiode++){
    sprintf(DataFilePath[NumDiode],"C:\\Documents and
Settings\\kiuser\\Desktop\\%s_%d.txt",FileName,NumDiode);
    sprintf(WritingMode,"w+");
    DataFileText[NumDiode] = fopen(DataFilePath[NumDiode],WritingMode);
    if (DataFileText[NumDiode]   == NULL) return -1;
    time (&Timer);
    TimerNow = Timer;
    AbsoluteTime = Timer;
    fprintf(DataFileText[NumDiode],"File: %s created at %ld since the
epoch.\n",FileName,TimerNow);
    fprintf(DataFileText[NumDiode],"Header Format(without spaces): Measurement# /t
Measurement Start Time(s) /t Estimated Fluence(n cm^-2 /n\n");
    fprintf(DataFileText[NumDiode],"IV Format(without spaces): V /t I /t Stdev(I) /t
Abs(I) /t StdDev(Abs(I) /n\n");
    fprintf(DataFileText[NumDiode],"CV Format(without spaces): V /t C /t G /n\n");
    sprintf(FeedBackString,"Output File # %d Built",NumDiode);
    PostDataString("Feedback",FeedBackString);
}
sprintf(FeedBackString,"\n");
PostDataString("Feedback",FeedBackString);

/*** Testing Routine ***/

/*** Pre-Soak ***/
for (i=1; i<=Presoak; i++){
    for(NumDiode = 1; NumDiode<=NumberOfDiodes; NumDiode++) {
        sprintf(command_string,"CA%dX", NumDiode*2-1);

kibsnd(GPIB_Address_707,IGNORE_PARAM,GPIBTIMO,strlen(command_string),command_string);
        sprintf(command_string,"CD%dX", NumDiode*2);

kibsnd(GPIB_Address_707,IGNORE_PARAM,GPIBTIMO,strlen(command_string),command_string);
        if (VIStart <= 0.0) {
            for (VInow = VIStart; VInow <= VIStop; VInow += VIStep) {
                forcev(SMU1,VInow);
                measi(SMU1,&VIDataArray[NumVIMeas][VISimpleCounter]);
```

```
            }
         }
        if (VIStart > 0.0) {
            for (VInow = VIStart; VInow >= VIStop; VInow -= VIStep) {
                forcev(SMU1,VInow);
                measi(SMU1,&VIDataArray[NumVIMeas][VISimpleCounter]);
            }
        }
        forcev(SMU1,0.0);
        sprintf(command_string,"NA%dX", NumDiode*2 - 1);

kibsnd(GPIB_Address_707,IGNORE_PARAM,GPIBTIMO,strlen(command_string),command_string);
        sprintf(command_string,"ND%dX", NumDiode*2);

kibsnd(GPIB_Address_707,IGNORE_PARAM,GPIBTIMO,strlen(command_string),command_string);
    }
}

/*** Loop Over Entire Time Set ***/
for (j=0; j<NumberTimeIntervals; j++) {
    TheGrandClock = TimeInterval[j] *60;

/*** Set Timers and Output Feedback for Location Within Loop ***/
    time(&Timer);
    TimerNow = Timer;
    TimerThen = TimerNow;
    if(j==0) TheBeginningOfTime = Timer;
    if(j>0) {
        TheBeginningOfTime = Timer - LoopTime;
        TimerThen = Timer - LoopTime;
    }
    if(TimeInterval[0]==0 && j==1) {
        TheBeginningOfTime = AbsoluteTime;
        TimerThen = AbsoluteTime;
    }
    TheGrandClockStep = TheGrandClock/NumberMeasurementsPerInterval[j];
    sprintf(FeedBackString,"****You Are in Time Loop # %d*****",j+1);
    PostDataString("Feedback",FeedBackString);
    sprintf(FeedBackString,"Time Step is %ld seconds",TheGrandClockStep);
    PostDataString("Feedback",FeedBackString);

    while ( (TimerNow-TheBeginningOfTime) <= TheGrandClock ) {
       if ( TimerNow - TimerThen >= TheGrandClockStep ) {
            ASimpleCounter = ASimpleCounter + 1;
            for (NumDiode= 1; NumDiode <= NumberOfDiodes; NumDiode++) {
                time(&Timer);
                TimeHack = Timer;
/*** VI with alpha-voltaic ***/
                for(NumVIMeas = 1; NumVIMeas<=NumVIMeasLoops; NumVIMeas++) {
                    VISimpleCounter = 0;
                    sprintf(command_string,"CA%dX", NumDiode*2-1);

kibsnd(GPIB_Address_707,IGNORE_PARAM,GPIBTIMO,strlen(command_string),command_string);
                    sprintf(command_string,"CD%dX", NumDiode*2);

kibsnd(GPIB_Address_707,IGNORE_PARAM,GPIBTIMO,strlen(command_string),command_string);
                    if (VIStart <= 0.0) {
                        for (VInow = VIStart; VInow <= VIStop; VInow += VIStep) {
                            VISimpleCounter = VISimpleCounter + 1;
                            forcev(SMU1,VInow);
                            measi(SMU1,&VIDataArray[NumVIMeas][VISimpleCounter]);
                            delay(5);
                            VIAbsDataArray[NumVIMeas][VISimpleCounter] =
fabs(VIDataArray[NumVIMeas][VISimpleCounter]);
                            VISourced[VISimpleCounter] = VInow;
                            if (NumVIMeas == 1) {
                                PostDataDouble("IV_Voltage", VInow);
                                PostDataDouble("Current",
VIAbsDataArray[1][VISimpleCounter]);
```

```
                        }
                    }
                }
                if (VIStart > 0.0) {
                    for (VInow = VIStart; VInow >= VIStop; VInow -= VIStep) {
                        VISimpleCounter = VISimpleCounter + 1;
                        forcev(SMU1,VInow);
                        measi(SMU1,&VIDataArray[NumVIMeas][VISimpleCounter]);
                        delay(5);
                        VIAbsDataArray[NumVIMeas][VISimpleCounter] =
fabs(VIDataArray[NumVIMeas][VISimpleCounter]);
                        VISourced[VISimpleCounter] = VInow;
                        if (NumVIMeas == 1) {
                            PostDataDouble("IV_Voltage", VInow);
                            PostDataDouble("Current",
VIAbsDataArray[1][VISimpleCounter]);
                        }
                    }
                }
                forcev(SMU1,0.0);
                sprintf(command_string,"NA%dX", NumDiode*2 - 1);

kibsnd(GPIB_Address_707,IGNORE_PARAM,GPIBTIMO,strlen(command_string),command_string);
                sprintf(command_string,"ND%dX", NumDiode*2);

kibsnd(GPIB_Address_707,IGNORE_PARAM,GPIBTIMO,strlen(command_string),command_string);
            }
/*** CV with alpha-voltaic ***/
            sprintf(NumReadings,"%.0f",(CVStop-CVStart)/CVStep+1);
            sprintf(command_string,"CC%d,B%dX", 2*NumDiode, NumDiode*2 - 1);

kibsnd(GPIB_Address_707,IGNORE_PARAM,GPIBTIMO,strlen(command_string),command_string);
            sprintf(command_string,"N1X");

kibsnd(GPIB_Address_590,IGNORE_PARAM,GPIBTIMO,strlen(command_string),command_string);

sprintf(command_string,"T2,1W1,,1V%+.2f,%+.2f,%+.2fB1,1,%sX",CVStart,CVStop,CVStep,NumRea
dings);

kibsnd(GPIB_Address_590,IGNORE_PARAM,GPIBTIMO,strlen(command_string),command_string);

kibrcv(GPIB_Address_590,IGNORE_PARAM,LF,GPIBTIMO,max_size,&rcv_size,response_string);
            for(CVSimpleCounter = 0; CVSimpleCounter < (CVStop-
CVStart)/CVStep+1;CVSimpleCounter++){
                inc = 36*CVSimpleCounter;
                for (CharNumber = 0+inc; CharNumber<=10+inc; CharNumber++) {
                    CapacitanceString[CharNumber-inc] = response_string[CharNumber];
                }
                for (CharNumber = 12+inc; CharNumber <= 22+inc; CharNumber++) {
                ConductanceString[CharNumber-12-inc] = response_string[CharNumber];
                }
                for (CharNumber = 24+inc; CharNumber <= 34+inc; CharNumber++) {
                    VoltageString[CharNumber-24-inc] = response_string[CharNumber];
                }
                CVSourced[CVSimpleCounter] = atof(VoltageString);
                PostDataDouble("CV_Voltage",CVSourced[CVSimpleCounter]);
                CVDataArray[CVSimpleCounter] = atof(CapacitanceString);
                PostDataDouble("Capacitance",CVDataArray[CVSimpleCounter]);
                GVDataArray[CVSimpleCounter] = atof(ConductanceString);
                PostDataDouble("Conductance",GVDataArray[CVSimpleCounter]);
            }
            sprintf(command_string,"V0X");

kibsnd(GPIB_Address_590,IGNORE_PARAM,GPIBTIMO,strlen(command_string),command_string);
            sprintf(command_string,"N0X");

kibsnd(GPIB_Address_590,IGNORE_PARAM,GPIBTIMO,strlen(command_string),command_string);
            sprintf(command_string,"NC%dX", NumDiode*2);
```

```
kibsnd(GPIB_Address_707,IGNORE_PARAM,GPIBTIMO,strlen(command_string),command_string);
                sprintf(command_string,"NB%dX", NumDiode*2-1);

kibsnd(GPIB_Address_707,IGNORE_PARAM,GPIBTIMO,strlen(command_string),command_string);

/*** Post Proccess VI data ***/
                N = NumVIMeasLoops;
                for (f=0;f<=2;f++){
                    for (s=0;s<=999;s++){
                        VIStdDataArray[f][s] = 0.;
                    }
                }
                if (NumVIMeasLoops == 1){
                    for(k=1; k <= VISimpleCounter; k++) {
                        VIAvgDataArray[1][k] = VIDataArray [1][k];
                        VIAvgDataArray[2][k] = VIAbsDataArray [1][k];
                    }
                }
                if (NumVIMeasLoops > 1) {
                    for(k=1; k <= VISimpleCounter; k++) {
                        for(m=1; m <= NumVIMeasLoops; m++) {
                            VIAvgDataArray[1][k] = VIAvgDataArray[1][k] +
VIDataArray[m][k];
                            VIAvgDataArray[2][k] = VIAvgDataArray[2][k] +
VIAbsDataArray[m][k];
                        }
                        VIAvgDataArray[1][k] = VIAvgDataArray[1][k]/NumVIMeasLoops;
                        VIAvgDataArray[2][k] = VIAvgDataArray[2][k]/NumVIMeasLoops;
                        for(m=1; m <= NumVIMeasLoops; m++) {
                            VIStdDataArray[1][k] = VIStdDataArray[1][k] +
pow((VIDataArray[m][k] - VIAvgDataArray[1][k]),2);
                            VIStdDataArray[2][k] = VIStdDataArray[2][k] +
pow((VIAbsDataArray[m][k] - VIAvgDataArray[2][k]),2);
                        }
                        VIStdDataArray[1][k] = sqrt(1.0/(N-1)*VIStdDataArray[1][k]);
                        VIStdDataArray[2][k] = sqrt(1.0/(N-1)*VIStdDataArray[2][k]);
                    }
                }
/*** Write data to file ***/
                fprintf(DataFileText[NumDiode],"\n\n\n");
                fprintf(DataFileText[NumDiode],"%d\t",ASimpleCounter);
                fprintf(DataFileText[NumDiode],"%ld\t",TimerNow-AbsoluteTime);
                fprintf(DataFileText[NumDiode],"%+.3e\t",(TimerNow-AbsoluteTime)*Flux);
                sprintf(FeedBackString,"Done With Diode # %d",NumDiode);
                PostDataString("Feedback",FeedBackString);
                time(&Timer);
                TimerThen = TimerNow;
                TimerNow = Timer;
                LoopTime = Timer - TimeHack;
                sprintf(FeedBackString," Diode LoopTime = %ld seconds",LoopTime);
                PostDataString("Feedback",FeedBackString);
                fprintf(DataFileText[NumDiode],"%+.3e\t\n",(TimerNow-AbsoluteTime)*Flux);
                fprintf(DataFileText[NumDiode],"IV\n");
                for (i = 1; i <= VISimpleCounter; i++) {
                    fprintf(DataFileText[NumDiode],"%+.3e\t",VISourced[i]);
                    fprintf(DataFileText[NumDiode],"%+.3e\t",VIAvgDataArray[1][i]);
                    fprintf(DataFileText[NumDiode],"%+.3e\t",VIStdDataArray[1][i]);
                    fprintf(DataFileText[NumDiode],"%+.3e\t",VIAvgDataArray[2][i]);
                    fprintf(DataFileText[NumDiode],"%+.3e\t\n",VIStdDataArray[2][i]);
                }

                fprintf(DataFileText[NumDiode],"CV\n");
                for (i = 1; i <= CVSimpleCounter; i++) {
                    fprintf(DataFileText[NumDiode],"%+.3e\t",CVSourced[i]);
                    fprintf(DataFileText[NumDiode],"%+.3e\t",CVDataArray[i]);
                    fprintf(DataFileText[NumDiode],"%+.3e\n",GVDataArray[i]);
                }
            }
```

```
/*** Post Information of Measurement Completion and Timing ***/
            sprintf(FeedBackString,"Done With Measurement %d",ASimpleCounter);
            PostDataString("Feedback",FeedBackString);
            sprintf(FeedBackString,"Taken at %ld seconds",TimerNow-AbsoluteTime);
            PostDataString("Feedback",FeedBackString);
            sprintf(FeedBackString,"Taken at a fluence of %+.3e n cm^-2",(TimerNow-
AbsoluteTime)*Flux);
            PostDataString("Feedback",FeedBackString);
            sprintf(FeedBackString,"\n");
            PostDataString("Feedback",FeedBackString);

/*** Reset Interval Time Loop ***/
       }
       time(&Timer);
       TimerNow = Timer;
    }
}

for (NumDiode = 1; NumDiode <= NumberOfDiodes; NumDiode++){
    fclose(DataFileText[NumDiode]);
}

/*** Extra Code ***/

//kibsnd(GPIB_Address,IGNORE_PARAM,GPIBTIMO,strlen(command_string),command_string);

//kibrcv(GPIB_Address,IGNORE_PARAM,LF,GPIBTIMO,max_size,&rcv_size,response_string);
         //PostDataString("Feedback",response_string);
         //Temperature[CurveCounter] = atof(response_string);
         //PostDataDouble("Temperature",Temperature[CurveCounter]);
         //sprintf(FeedBackString,"HERE");
         //PostDataString("Feedback",FeedBackString);
/* USRLIB MODULE END  */
}              /* End IVCV_Neutron_BCdiode_CVSweep_MultipleDiodes.c */
```

Bibliography

[1] "Nuclear Regulatory Legislation," US Nuclear Regulatory Commission, Washington, DC, NUREG-0980, 2009.

[2] "Nuclear Posture Review Report," Department of Defense, Wahington, DC, 2010.

[3] J.K. Shultis and R.E. Faw, *Radiation Shielding*. La Grange Park, IL: American Nuclear Society, Inc, 2000.

[4] (2010, June) Nuclear Structure and Decay Data, NUDAT 2.5. [Online]. http://www.nndc.bnl.gov/nudat2

[5] A.N. Caruso, Presentation to ONR M-WMD-D,"High Efficiency Fast Neutron Detection by Solid State Diect Conversion Heterostructures", Washington, DC, August 2009.

[6] T. Kimura, "Quantitative Evaluation of Multiple Production of Neutrons Induced by Cosmic Rays in Materials," *Journal of Nuclear Science and Technology*, vol. 27, no. 12, pp. 1147-1150, December 1990.

[7] R.T. Kouzes, E.R. Siciliano, J.H. Ely, P.E. Keller, and R.J. McConn, "Passive Neutron Detection at Borders," in *IEEE Nuclear Science Symposium*, Honolulu, 2007, pp. 1115-1119.

[8] R. T. Kouzes et al., "Cosmic-ray-induced ship-effect neutron meqasurements and implications for cargo scanning at borders," *Nuclear Instruments and Methods in Physics Research A*, vol. 587, pp. 89-100, January 2008.

[9] A.N. Caruso, presentation to AFIT, "High Efficiency Fast and Slow Neutron Detection by Solid State Heterostructures", Air Force Institute of Technology, Wright-Patterson AFB, OH, May 2010.

[10] A.N. Caruso, "The physics of solid-state neutron detector materials and geometries," *Journal of Physics: Condensed Matter*, vol. 22, p. 32, October 2010.

[11] David Kramer, "DOE begins rationing helium-3," *Physics Today*, pp. 22-25, June 2010.

[12] G.F. Knoll, *Radiation Detection and Measurements.*: John Wiley and Sons, 2000.

[13] E.E. Day, B.W. Robertson, S. Adenwalla, and A.D. Harken, "Boron-Rich Semiconducting Boron Carbide Neutron Detector," *Japanese Journal of Applied Physics*, vol. 44, no. 1A, pp. 444-445, January 2005.

[14] S. Karki et al., "Fabrication and trasnsport properties of a-B5C:Hx to n-type Si heterojunction diodes," in *American Physical Society*, Dallas, 2011.

[15] N. Hong, M. A. Langell, J. Liu, O. Kizikaya, and S. Adenwalla, "Ni doping of semiconducting boron carbide," *Journal of Applied Physics*, vol. 107, p. 024513, January 2010.

[16] H. Werheit, "Experimentally Founded Charge Transport Model for Icosahedral Boron-Rich Solids," in *Boron Rich Solids: Sensors, Ultra High Temperature Cermaics, Thermoelectrics, Armor*. Netherlands: Springer, 2009, pp. 45-62.

[17] A. N. Caruso et al., "Surface photovoltage effects on the isomeric semiconductors of boron-carbide," *Applied Physics Letters*, vol. 84, no. 8, pp. 1302-1304, February 2004.

[18] A. N. Caruso, P. Lunca-Popa, Y. B. Losovyj, A. S. Gunn, and J. I. Brand, "The Band Offsets of Isomeric Boron Carbide Overlayers," in *Matterials Research Symposium Proceedings Vol. 836*, 2005.

[19] R. B. Billa, T. Hoffman, M. Schubert, and B. W. Robertson, "Annealing effects on the optical properties of semiconducting boron carbide," *Journal of Applied Physics*, vol. 106, p. 033515, August 2009.

[20] D. L. Shultz el al, "Characterization of a-B5C:H prepared by PEVCD of orthocarborane: results of preliminary FTIR and nuclear reaction analysis studies," *Journal of Non-Crystaline Solids*, vol. 354, pp. 2369-2367, 2008.

[21] J. Mullins, K.Foreman, S.Adenwalla and N.Hong, "Boron Carbide Based Solid State Neutron Detectors: The effects of Bias and Time Constant on Detection Efficiency," *Journal of Physics D: Applied Physics*, vol. 43, pp. 1-11, June 2010.

[22] A. Harken, E. Day, B.W. Robertson, S. Adenwalla, and C. Lundestedt, "Modeling Solid-State Boron Carbide Low Energy Neutron Detectors," *Nuclear Instruments and Methods in Physics Research*, vol. 562, pp. 380-388, February 2006.

[23] A. A. Bickley, Boron Carbide Spectrometer Geant Update, 2010, Personal Correspondence.

[24] J. C. Petrosky, J. W. McClory, A. N. Caruso, and P. A. Dowben, "High Efficiency Solid State Neutron Detector and Spectrometer," August 18, 2009.

[25] J. E. Bevins, J. W. McClory, A. N. Petrosky, and A. N. Caruso, "Theoretical Performance of a p-type B5c:Hx Thin Film on n-Si Neutron Detector," in *American Nuclear Society Transactions Vol. 106*, Las Vegas, 2010.

[26] D. Emin, "Unusual Properties of Icosahedral Boron-Rich Solids," *Journal of Solid-State Chemistry*, vol. 179, pp. 2791-2798, January 2006.

[27] M.F. Hawthorne, D.C. Young and P.A. Wegner, "Carbametallic Boron Hydride Derivatives: Apparent Analogs of Ferrocence and Ferricinium Ion," *Journal of the American Chemical Society*, vol. 87, no. 8, pp. 1818-189, 1965.

[28] S. Adenwalla, A. Harken, P.Welsch, J.I. Brand, P.A. Dowben, and B.W. Robertson, "A Class of Boron Rich Solid-State Neutron Detectors," *Applied Physics Letters*, vol. 80, no. 19, pp. 3644-3646, May 2002.

[29] Synopsis Inc., "Sentaurus Device User's Guide", December 2007, Version A-2007.12.

[30] C. Wood and D. Emin, "Conduction Mechanism in Boron Carbide," *Physical Review B*, vol. 29, no. 8, pp. 4582-4587, April 1984.

[31] R. Schmechel and H. Werheit, "Correlation between structural defects and electronic properties of icosahedral boron-rich solids," *Journal of Physics: Condensed Matter*, vol. 11, pp. 6803-6813, May 1999.

[32] R. Schmechel and H. Werheit, "Evidence of the Superposition of Drude Type and Hopping Type Transport in Boron-Rich Solids," *Jounal of Solid State Chemistry*, vol. 133, pp. 335-341, July 1997.

[33] U. Kuhlmann and H. Werheit, "Distribution of carbon atoms on the boron carbide structure," *Journal of Alloys and Compounds*, vol. 189, pp. 249-258, June 1992.

[34] A. S. Anan'ev et al., "Fabrication and Properties of Amorphous Hydrogenated Boron Carbide Films," *Amorphous, Vitreous and Pourous Semiconductors*, vol. 36, no. 8, pp. 1006-1009, Feb 2002.

[35] S. Lee, J. Mazurowski, G. Ramseyer, and P. A. Dowben, "Characterization of boron carbide thin films fabricated by plasma enhanced chemical vapor deposition from boranes," *Journal of Applied Physics*, vol. 72, no. 100,

pp. 4925-4923, November 1992.

[36] M. M. Balakrishnarajan, P. D. Pancharatna, and R. Hoffmann, "Structure and bonding in boron carbide: The invincibility of imperfections," *New Journal of Chemistry*, vol. 31, pp. 473-485, February 2007.

[37] H. Werheit, "Present Knowledge of electric properties and charge transport of icosahedral boron-rich solids," in *16th International Symposium on Born,Borides, and Related Materials*, Japan, 2009.

[38] L.G. Bulusheva, V.V.Volkov, and A.V. Okotrub, "Electron interactions in the closo-carboranes 1,2- and 1,7-C2B10H12," *Journal of Molecular Structure*, vol. 520, pp. 33-38, March 2000.

[39] R.B. Billa, S. Balaz, J.L. Brand, P.A.Dowben, and A.N. Caruso, "The Heteroisomerio Diode," *Journal of Physics: Condensed Matter*, vol. 16, pp. L139-L146, February 2004.

[40] D. Emin, "Electronic Transport in Boron Carbides," in *AIP Conference Proceedings*, 1986.

[41] I. A. Howard, C. L. Beckel, and D. Emin, "Bipolarons in boron icosahedra," *Physics Review B*, vol. 35, p. 2929, 1987.

[42] H. Werheit, "Are there bipolarons in icosahedral boron-rich solids?," *Journal of Physics: Condensed Matter*, vol. 19, no. 18, pp. 1-14, April 2007.

[43] H. Werheit, "On Excitons and Other Gap States in Boron Carbide," *Journal of Physics: Condensed Matter*, vol. 18, no. 47, pp. 10655-10662, November 2006.

[44] H. Werheit, "Thermoelectric Properties of Boron-Rich Solids and their Possibilities of Technical Application," in *25th International Conference*

on ICT '06, Campus Duisburg, 2006, pp. 159-163.

[45] R. Schmechel, R. Werheit, V. Kueffel, and T. Lundstrom, "Electronic tansport in p-type and n-type beta-rhombohedral boron," in *16th International Conference on Thermoelectrics*, 1997, pp. 219-223.

[46] P. A. Dowben, Neutron Detection Group Meeting, August 20, 2010, Personal Correspondence.

[47] T. L. Aselage and D. Emin, "Boron Carbides: Unconventional High-Temperature Thermoelectrics," Sandia National Labratories, Albuquerque, SAND2002-3200P, 2002.

[48] H. K. Clark and J. L. Hoard, "The Crystal Structure of Boron Carbide," *Journal of the American Chemical Society*, vol. 65, no. 11, pp. 2115-2119, 1943 November.

[49] B. V. Zeghbroeck, *Principles of Semiconductor Devices*. US: Univeristy of Colorado Online Book, 2010.

[50] H. Suematsu et al., "Preparation of polycrystalline boron carbide thin films at room temperature by pulsed ion-beam evaporation," *Applied Physics Letters*, vol. 80, no. 7, pp. 1153-1155, February 2002.

[51] S. Adenwall et al., "Boron carbide/n-silicon carbide heterojunction diodes," *Applied Physics Letters*, vol. 79, no. 26, pp. 4357-4359, December 2001.

[52] S. D. Hwang, N. Remmes, and P. A. Dowben, "Nickel doping of boron-carbon alloy films and corresponding Fermi level shifts," *Journal of Vacuum Science Technology*, vol. 15, no. 3, pp. 854-859, June 1997.

[53] D. N. McIlroy et al., "The incorporation of Nickel and Phosphorus dopants into Boron-Carbon alloy thin films," *Applied Physics A: Materials Science and Processing*, vol. 67, pp. 335-342, 1998.

[54] J. Petrosky, *NENG 660 Radiation Effects Book Notes*. Wright-Patterson AFB, OH: Air Force Institute of Technology, 2010.

[55] C.A. Klein, "Bandgap Dependence and Related Features of Radiation Ionization Energies in Semiconductors," *Journal of Applied Physics*, vol. 39, no. 4, pp. 2029-2038, March 1968.

[56] D. S. McGregor et al., "Self-Biased Boron-10 Coated High-Purity Epitaxial GaAs Thermal Neutron Detectors," *IEEE Transactions on Nuclear Science*, vol. 47, no. 4, pp. 1364-1370, August 2000.

[57] A. N. Caruso et al., "The all boron carbide diode neutron detector: Comparison with theory," *Material Science and Engineering B*, vol. 135, pp. 129-133, August 2006.

[58] D. N. McIllroy, "Heteroisomeric diode - a solid state neutron detector," *Journal of Physics: Condensed Matter*, vol. 16, pp. V13-V14, 2004.

[59] E. Day, M. J. Diaz, and S. Adenwalla, "Effect of bias on neutron detection in thin semi-conducting boron carbide films," *Journal of Physics D: Applied Physics*, vol. 39, pp. 2920-2924, June 2006.

[60] K. Osberg et al., "A Handheld Neutron-Detection Sensor System Utilizing a New Class of Boron Carbide Biode," *IEEE Sendors Journal*, vol. 6, no. 6, pp. 1531-1538, December 2006.

[61] A. Holmes-Siedle and L. Adams., *Handbook of Radiation Effects*. Oxford, NY: Oxford University Press, 2007.

[62] A. Jostons, C. H.H. DuBose, G. L. Copeland, and J. O. Stiegler, "Defect Nature of Neutron Irradiated Boron Carbide," *Journal of Nuclear Materials*, vol. 49, pp. 136-150, June 1973.

[63] G. Hall, "Issues for deep level models of bulk damage to silicon detectors," *Nuclear Instruments and Methods in Physics Research: Section A*,

vol. 388, pp. 283-288, 1997.

[64] G. Lindstrom and et al, "Radiation hard silicon detectors - developments by the RD48 (ROSE) collaboration," *Nuclear Instruments and Methods in Physics Research A*, vol. 466, pp. 308-326, 2001.

[65] M. Moll, "Radiaition Damage in Silicon Particle Detectors," CERN, Technical Training 2000.

[66] R. Wunstorf, "Radiation Hardness of Silicon Detectors: Current Status," *IEEE Transactions on Nuclear Science*, vol. 44, no. 3, pp. 806-814, 2007.

[67] J.Robbins M. Matheson, S. Watts, G. Hall, and B. MacEvoy, "A microscopic explanation for type inversion and the annealing behaviour of radiation damaged silicon detectors," *Nuclear Instruments and Methods in Physics Research: Section A*, vol. 371, pp. 575-577, 1996.

[68] U. Biggeri, E. Borchi, M Bruzzi, Z. Li, and S. Lazanu, "Studies of Deep Levels in High Resistivity Silicon Detectors Irradiated by HYigh Fluence Fast Neutrons Using a Thermally Stimulated Current Spectrometer," *IEEE Transactions on Nuclear Science*, vol. 41, no. 4, pp. 964-970, August 1994.

[69] Z. Li et al., "Investigation of the Oxygen-VAcancy (A-Center) Defect Complex Profile in Neutron Irradiated High Resistivity Silicon Junction Particle Detectors," *IEEE Transactions on Nuclear Science*, vol. 39, no. 6, pp. 1730-1738, December 1992.

[70] R. Wheadon, "Aspects of radiation hardness for silicon microstrip detectors," *Nuclear Instruments and Methods in Physics Research: SEction A*, vol. 386, pp. 143-148, 1997.

[71] G. Hall, "Issues for Deep Level Models of Bulk Damage in Silicon Detectors," in *International Conference on Radiation Effects on*

Semiconductor Materials, Detectors, and Devices, Florence, 1996, pp. 1-10.

[72] G. Lindstrom, "Radiation Damage in Silicon Detectors," *Nuclear Instruments and Methods in Physics Research: Section A*, vol. 512, pp. 30-43, 2003.

[73] G. Casse, P. P. Allport, and M. Hanlon, "Improving the radiation hardness properties of silicon detectors using oxygenated n-type and p-type silicon," *IEEE Transactions on Nuclear Science*, vol. 47, no. 3, pp. 527-532, June 2000.

[74] G. C. Messenger, "A Summary Review of Displacement Damage from High Energy Radiation in Silicon Semiconductors and Semiconductor Devices," *IEEE Transactions on Nuclear Science*, vol. 39, no. 3, pp. 468-473, June 1992.

[75] G. C. Messenger and J. P. Spratt, "The Effects of Neutron Irradiation on Germanium and Silicon," in *Proceedings of the IRE*, 1958, pp. 1038-1044.

[76] V. Eremin, Z. Li, and I. Iljashenko, "Trapping induced Neff and elctrical field transformation at different temperatures in neutron irradiated high silicon detectors," *Nuclear Instruments and Methods in Physics Research A*, vol. 360, pp. 458-462, 1995.

[77] (2010, December) GEANT4 User Documentation. [Online]. http://geant4.carn.ch/support/userdocumentation.shtml

[78] J. F. Ziegler, J. P. Biersack, and M. D. Ziegler, *SRIM: The stopping and Range of Ions in Matter*. New York: Pergamon Press, 1996.

[79] P. Kluth et al., "Energy dependent saturation width of swift heavy ion shaped embedded Au nanoparticles," *Applied Physics Letters*, vol. 94, p. 113107, March 2009.

[80] H. S. Virk, "Heavy Ion tracks Route to Nanotechnology," *Advanced Materials Research*, vol. 67, pp. 115-120, 2009.

[81] R. Katz and E. J. Kobetich, "Particle Tracks in Emulsion," *Physics Review*, vol. 186, no. 2, pp. 344-351, October 1969.

[82] J. W. McClory, The Effect of Radiation on the Electrical Poperties of Aluminum Gallium Nitride/Gallium Nitrude Heterostructures, 2008, Air Force Institute of Technology Dissertation.

[83] A.N. Caruso, Professor, Department of Physics, UMKC, Personal Correspondence, 5 June 2010.

[84] J. C. Petrosky, Characterization of Hg1-xCdxTe Diodes Using PISCES-IIB and Implications to Radiation Effects, 1992, Rensselaer Polytechnic Institute Thesis.

[85] ASTM International, "Standard Practice for Characterizing Neutron Energy Spectra in Terms of an Equivalent Monoenergetic Neutron Fluence for Radiation-Hardness Testing of Electronsics," ASTM, West Conshohocken, E722-94, 2002.

[86] S.M. Sze, *Semiconducting Devices: Physics and Technology.*: John Wiley and Sons, 2002.

[87] J. C. Messenger, E. A. Burke, G. P. Summers, and M. A. Xapsos, "Nonionizing Energy Loss (NIEL) for Heavy Ions," *IEEE Transactions on Nuclear Science*, vol. 46, no. 6, pp. 1595-1602, December 1999.

REPORT DOCUMENTATION PAGE

Form Approved
OMB No. 074-0188

1. REPORT DATE *(DD-MM-YYYY)*	**2. REPORT TYPE**	**3. DATES COVERED** *(From – To)*
24-03-2011	Master's Thesis	June 2010 – March 2011

TITLE AND SUBTITLE

Characterization of a Boron Carbide Heterojunction Neutron Detector

5a. CONTRACT NUMBER

5b. GRANT NUMBER

5c. PROGRAM ELEMENT NUMBER

6. AUTHOR(S)

Bevins, James E 2Lt USAF

5d. PROJECT NUMBER
N/A

5e. TASK NUMBER

5f. WORK UNIT NUMBER

7. PERFORMING ORGANIZATION NAMES(S) AND ADDRESS(S)

Air Force Institute of Technology
Graduate School of Engineering and Management (AFIT/EN)
2950 Hobson Way
WPAFB OH 45433-7765

8. PERFORMING ORGANIZATION REPORT NUMBER

AFIT/GNE/ENP/11-M02

9. SPONSORING/MONITORING AGENCY NAME(S) AND ADDRESS(ES)
Defense Threat Reduction Agency
COL Mark Mattox
1900 Wyoming Blvd SE
Kirtland AFB, NM 87117-5669

10. SPONSOR/MONITOR'S ACRONYM(S)
DTRA/OP-CSU

11. SPONSOR/MONITOR'S REPORT NUMBER(S)

12. DISTRIBUTION/AVAILABILITY STATEMENT
APPROVED FOR PUBLIC RELEASE; DISTRIBUTION UNLIMITED

13. SUPPLEMENTARY NOTES

14. ABSTRACT

New methods for neutron detection have become an important area of research in support of national security objectives. In support of this effort, p-type B_5C on n-type Si heterojunction diodes have been built and tested. This research sought to optimize the boron carbide (BC) diode by coupling the nuclear physics modeling capability of GEANT4 and TRIM with the semiconductor device simulation tools. Through an iterative modeling process of controllable parameters, optimal device construction was determined such detection efficiency and charge collection were optimized. This allows an estimation of expected charge collection and efficiency given a set of operating parameters that include: silicon resistivity, BC resistivity, BC thickness, silicon thickness, applied bias, and collection contact. Charge collection was maximized with high bias operation of thin BC layers on thin silicon substrates of low resistivity ($<$10 Ω-cm), while the capture efficiency was maximized for thicker BC layers.

Additionally, the effects of neutron damage on BC diodes were studied to determine damage thresholds and resulting device performance and lifetime. The major limitation found for device performance was the increase in the leakage current (~340% at a thermal fluence of $9.7\text{x}10^{13}$ n cm^{-2}) in the 8k Ω-cm diode. Type inversion was not measured at the total fluence levels achieved, but the 8k Ω-cm diode effective carrier concentrations (N_{eff}) decreased by 30% at a total thermal fluence of $7.5\text{x}10^{13}$ n cm^{-2} ($1\text{x}10^{13}$ 1 MeV neutron equivalent). For the same irradiation conditions, the 20k Ω-cm diode N_{eff} decreased by 57%. These results indicate that the hardness of the diodes can be improved with low resistivity silicon substrates.

15. SUBJECT TERMS
Neutron, Detector, Optimization, Boron Carbide, Radiation Effects

16. SECURITY CLASSIFICATION OF: UNCLASSIFIED			**17. LIMITATION OF ABSTRACT**	**18. NUMBER OF PAGES**	**19a. NAME OF RESPONSIBLE PERSON**
a. REPORT	**b. ABSTRACT**	**c. THIS PAGE**			LTC John McClory, AFIT/ENP
U	U	U	UU	193	**19b. TELEPHONE NUMBER** *(Include area code)* (937) 255-3636 ext 7308, john.mcclory@afit.edu

Standard Form 298 (Rev. 8-98)
Prescribed by ANSI Std. Z39-18